Hypervelocity Stars
Kinematic studies of low-mass stars and hot subdwarfs

Der Naturwissenschaftlichen Fakultät
der Friedrich-Alexander-Universität
Erlangen-Nürnberg

zur

Erlangung des Doktorgrades Dr. rer. nat.

vorgelegt von

Eva Ziegerer
aus Nürnberg

Zusammenfassung

Hypervelocity Sterne (HVS) sind Sterne, die sich so schnell fortbewegen, dass sie nicht mehr gravitativ an unsere Milchstraße gebunden sind, d.h. sie sind schneller als die lokale Fluchtgeschwindigkeit der Galaxis. Diese Sterne und ihre langsameren Gegenstücke, die Runaways, sind wichtige Indikatoren für den Dunkle Materie Halo der Galaxis. Als sie das erstemal im Jahre 2005 entdeckt wurden, war der Auswurf aus dem galaktischen Zentrum durch die Zerstörung eines Doppelsternsystems, aufgrund der auftretenden Gezeitenkräfte zwischen dem System und dem Supermassiven Schwarzen Loch dort, die einzige Erklärung (Hills Mechanismus).

Ein alternativer Beschleunigungsmechanismus stellt der Supernova Ejektions Mechanismus dar. Wenn der Primärstern in einer Supernova explodiert, wird sein Begleiter mit einer Geschwindigkeit freigesetzt, die stark mit dessen Orbitgeschwindigkeit verknüpft ist. Je kompakter ein Doppelsternsystem ist, desto höher die Orbitgeschwindigkeit. Daher können bei einem Kernkollaps eines Riesensterns in einem Binärsystem keine allzu hohen Geschwindigkeiten produziert werden da der Abstand der beiden Sterne größer als die Summe ihrer Radien sein muss. In einem ultrakompakten System dagegen, in dem ein Weißer Zwerg einen heißen Unterriesen umkreist, wird der Abstand aufgrund der Abstrahlung von Gravitationswellen mit der Zeit schrumpfen. Wenn der Unterzwerg dann sein Roche-Limit ausfüllt wird er anfangen heliumreiches Material auf die Oberfläche des Weißen Zwergs zu transferieren, welches die Explosion des letzteren auslösen kann.

In Regionen mit hohen Sterndichten kann die dynamische Ejektion auftreten. Während einer nahen Begegnung können große Impulse auf den masseärmsten der beteiligten Komponenten übertragen werden. Dieser Prozess ist am effektivsten wenn zwei enge Doppelsterne miteinander kollidieren.

HVSs vom Typ B mit Massen von $3 - 4$ Sonnenmassen wurden gezielt in einer Radialgeschwindigkeits-Durchmusterung gesucht, da diese Sterne leuchtstark genug sind um sie bei Distanzen von über 100 kpc zu beobachten und gleichzeitig lang genug leben (einige hundert Myr). Die Durchmusterung brachte zwei Dutzend HVSs auf der nördlichen Hemisphäre hervor. Vor 2014 wurde noch kein HVS-Kandidat unter der sonnenähnlichen Sternen gefunden. Palladino et al. (2014) gaben die Entdeckung von nicht weniger als 20 massearmen HVS-Kandidaten in der Liste der Segue G und K Zwerge bekannt, von denen keiner aus dem Zentrum stammt. Da diese Entdeckung unerwartet kam und im Widerspruch zu theoretischen Vorhersagen steht führten wir eine kinematische Analyse der Kandidaten durch, wobei wir die komplette 6D Phasenraum Information verwendeten, die auf neuen Messungen der Eigenbewegung beruhen.

Diese Studie zielt darauf ab neue HVS-Kandidaten zu finden und bereits bekannte genauer

zu untersuchen. Wir führten an ihnen spektroskopische und kinematische Untersuchungen durch. Quantitative Spektralanalysen liefern Radialgeschwindigkeiten und atmosphärische Parameter für die Bestimmung der spektroskopischen Distanzen. Um die komplette 6D-Phasenraum Information zu erhalten, führten wir ebenfalls Eigenbewegungsmessungen durch. Die Eigenbewegungen wurden aus einer Kombination von Positionsmessungen von alten photographischen Aufnahmen und modernen digitalen Himmelsdurchmusterungen vorgenommen. Wir überprüften diese anhand von Eigenbewegungskatalogen auf Konsistenz. Die orbitalen Eigenschaften können anschließend bestimmt werden, indem die Bahn in verschiedenen Massenmodellen der Galaxis zurückverfolgt wird.

Wir präsentieren die Ergebnisse für 14 HVS-Kandidaten der Palladino et al. (2014) Sterne, für die die Messung der Eigenbewegung möglich war. Die Werte der erhaltenen Eigenbewegungen sind signifikant niedriger als in der vorangegangenen Studie. Unter Berücksichtigung von drei verschiedenen galaktischen Massenmodellen sind wir der Auffassung, dass alle Sterne gravitativ an die Milchstraße gebunden sind. Wir können bestätigen, dass die Sterne nicht aus dem galaktischen Zentrum stammen. Die Verteilung ihrer Eigenbewegungen und Radialgeschwindigkeiten stimmen überein mit Vorhersagen für Runaway Sterne, die aufgrund einer Supernovaexplosion in einem Doppelsternsystem aus der galaktischen Scheibe herausgeschleudert wurden. Jedoch sind ihre Kinematiken ebenfalls konsistent mit einer Zugehörigkeit zur Population alter Scheibensterne. Die meisten der Sterne haben sogar eher niedrige Metallizitäten und starke α-Element Anhäufungen, was typisch für Sterne der dicken Scheibe und des Halos ist. Wohingegen die Metallizität der 3 metallreichsten Sterne möglicherweise darauf hindeutet, dass diese Runaway Sterne der dünnen Scheibe sein könnten. Ein Stern zeigt Halo Kinematik, aber keiner kann als HVS klassifiziert werden. Daher warten wir nach wie vor auf die Entdeckung des ersten sonnenähnlichen HVS.

Das Hyper-MUCHFUSS Projekt hat zum Ziel, potentiell ungebundene heiße Unterzwerge mit hohen Geschwindigkeiten zu finden. Genau wie für die Liste der G und K Sterne wurden die Eigenbewegungen bestimmt und die Bahnen der Sterne in verschiedenen Massenmodellen zur galaktischen Scheibe zurückverfolgt.

Wir präsentieren die kinematische Analyse des schnellsten ungebundenen Sterns unserer Galaxis, dem kompakten Helium Stern (He-sdO) US 708. Für ihn zeigt die Rekonstruktion seiner Flugbahn, sowohl durch die Verwendung von erdgebundenen Eigenbewegungsmessungen, als auch die des Hubble Space Telescope (HST), dass ein Ursprung im galaktischen Zentrum äußerst unwahrscheinlich ist. Daher kann der Hills Mechanismus für US 708 ausgeschlossen werden, obwohl er möglicherweise der bevorzugte Beschleunigungsmechanismus für andere HVSs bleibt. Desweiteren konnten wir anhand von neuen spektroskopischen Beobachtungen nachweisen, dass es sich bei US 708 um einen schnellen Rotator handelt, was dafür spricht, dass er sehr wahrscheinlich der Hinterbliebene eines ursprünglich engen Doppelsternsystems ist, dessen Begleiter in einer thermonuklearen Supernova explodiert ist. Er wurde durch die Gezeitenkräfte, die in einem solchen System herrschen, aufgedreht.

Die Untersuchung eines weiteren He-sdO Sterns und drei weiterer Kandidaten unter den sdB Sternen wird ebenfalls gezeigt. Die Geschwindigkeiten im galaktischen Ruhesystem reichen von 203 km s^{-1} bis zu 660 km s^{-1}, was darauf hindeutet, dass alle vier Sterne sehr wahrscheinlich gravitativ an die Galaxis gebunden sind. Mit einer Temperatur von $T_{\text{eff}} =$ 47000 K und einer Schwerebeschleunigung an der Oberfläche von $\log g = 5.7$, ist SDSS

J205030.39−061957.8 (J2050) ein spektroskopischer Zwilling des He-sdO HVS US 708. Für J2050 kann das galaktische Zentrum als Ursprungsort aufgrund der kinematischen Analyse ebenfalls ausgeschlossen werden. Die benötigte Auswurfgeschwindigkeit ist wesentlich moderater (385 ± 79 km s^{-1}) als die von US 708 (998 ± 68 km s^{-1}). Das Szenario eines Sterns der in einem Doppelsternsystem durch eine thermonukleare Supernova explodiert, wie es für US 708 vorgeschlagen wurde, würde die beobachteten Eigenschaften von J2050 sehr gut erklären, ohne dabei die Modellparameter bis zu ihren absoluten Grenzen zu strapazieren, wie es für US 708 nötig ist. Dementsprechend wäre der Stern der Überlebende einer solchen Supernova vom Typ Ia.

Die drei weiteren sdB Sterne zeigen ebenfalls extreme Kinematiken: einer könnte ein HVS aus dem galaktischen Zentrum sein. Die anderen beiden wurden möglicherweise durch den Doppelsternsystem Supernova Mechanismus aus der galaktischen Scheibe herausgeschleudert. Alternativ könnte es sich bei den Sternen auch um Halo Sterne mit extremen Kinematiken handeln.

Außerdem präsentieren wir die kinematische Analyse des bereits zuvor untersuchten HVS-Kandidaten SDSS J121150.27+143716.2 (J1211), einem heißen Unterzwerg vom Typ B (sdB) mit einem Hauptreihenstern vom Typ K als Begleiter auf einer weiten Umlaufbahn. Es kann nicht ausgeschlossen werden, dass das System noch gravitativ an die Galaxis gebunden ist. J1211 ist damit der erste und bisher einzige HVS-Doppelstern-Kandidat. Alle gängigen Beschleunigungsmechanismen konnen ausgeschlossen werden. Seine Bahn zeigt in der Vergangenheit nicht in Richtung des galaktischen Zentrums. Sowohl die Beschleunigung durch eine Supernova wie im Fall von US 708 als auch die Austauschkollision in einem Sternhaufen sind ausgeschlossen. In beiden Fällen wäre das Doppelsternsystem zerstört worden. Das Doppelsternsystem ist entweder im Halo entstanden oder es wurde von der Milchstraße von dem Überrest einer durch Gezeitenkräfte zerrissenen Zwerggalaxie akkretiert. Sollte letzteres der Fall sein, müsste der Stern Teil eines Sternstroms im Halo sein, der noch durch *Gaia* Astrometrie entdeckt werden muss.

Die *Gaia* Mission wir genaue Eigenbewegungen für alle Sterne heller als ~ 21 mag messen Am Ende der Mission wird die Eigenbewegung um ein oder zwei Größenordnungen genauer ($0.03 - 0.6$ mas yr^{-1}) sein als erdgebundene Eigenbewegungen, was zu einer Verifizierung unserer Ergebnisse führt und es wird zum ersten Mal möglich sein, genauere Aussagen über den Ursprung von HVSs zu machen.

Gaia Parallaxen und die daraus resultierenden Distanzen werden genauer sein als spektroskopische Distanzen, die wir verwenden mussten. Allerding nur für Sterne näher als $2 - 4$ kpc. Für die betreffenden Sterne wird die Tangentialgeschwindigkeit damit mit sehr hoher Genauigkeit bestimmbar. Jedoch sind alle bekannten HVSs deutlich weiter entfernt (bis zu 100 kpc), was die Notwendigkeit von detaillierten quantitativen Spektralanalysen bekräftigt. Nachbeobachtungen der Radialgeschwindigkeit der neu entdeckten Sterne werden ebenfalls sehr viele erdgebundene Beobachtungen benötigen. *Gaia* Photometrie und erdgebundene Durchmusterungen (z.B. Skymapper) werden eine Durchsuchung der südlichen Hemisphäre nach Hyperschnellläufern ermöglichen. Diese ist von größter Bedeutung für die Untersuchung der Verteilung der Dunklen Materie im Halo.

Abstract

Hypervelocity stars (HVS) are stars that move so fast that they are not gravitationally bound to the Galaxy, i.e. they are faster than the local escape velocity of the Galaxy. These stars and their slower counterparts, the runaway stars are important tracers for the dark matter halo of the Galaxy. When they were first discovered in 2005, ejection from the supermassive black hole (SMBH) in the Galactic centre (GC) through tidal disruption of a binary was suggested as their origin (the so-called Hills mechanism).

An alternative acceleration mechanism is the supernova ejection mechanism. When the primary of a binary system explodes in a supernova, its secondary is released with an ejection velocity that is closely connected to the secondary's orbital velocity. The more compact the binary is the higher is the orbital velocity. Therefore, the core collapse of a giant star in a binary cannot produce high velocities as the separation of the two stars must be larger than the sum of their radii. Whereas, in an ultracompact binary, where a white dwarf (WD) orbits a hot subdwarf the stars' separation will shrink with time due to the emission of gravitational waves. When the subdwarf fills its Roche lobe, mass transfer will start, and helium-rich material is transferred to the companion which can trigger the explosion of the WD.

In regions with high stellar densities also the dynamical ejection can occur. During a close encounter large kicks can be transferred to the least massive of the envolved companions. This process is most efficient when two close binaries collide.

Late B-type stars, with masses between $3-4$ solar masses were targeted in a radial velocity survey for HVSs, because such stars are luminous enough to be observable to $> 100\,\mathrm{kpc}$ while living sufficiently long (a few hundred Myr). The survey unravelled two dozens of HVSs on the Northern hemisphere. Prior to 2014, no HVS star has been found among solar-like stars. Palladino et al. (2014) announced no less than 20 low-mass HVS candidates in the Segue G and K dwarf sample, but none of them originates from the GC. Because these discoveries came unexpected and were at variance with theoretical predictions, we embarked on a kinematic analysis of the Segue HVS candidate sample using the full 6D phase space information based on new proper motion measurements.

This study aims at finding new HVS candidates and revisiting previously studied candidates. We performed a spectroscopic and kinematic analysis of the stars of interest. Quantitative spectral analyses provided radial velocities and atmospheric parameters for the determination of the spectroscopic distances. In order to get the full 6D phase-space motion we also made use of proper motion measurements. They are determined by combining positions from early-epoch photographic plates with those derived from modern digital sky surveys. We also checked for consistency with proper motion catalogues. The orbital properties of the

ABSTRACT

stars could then be derived by tracing back their trajectories in different mass models of our Galaxy.

We present the results for 14 candidate HVSs from the Palladino et al. (2014) sample for which proper motion measurements were possible. Considerably lower proper motions than given in the previous study were derived. Considering three different Galactic mass models, we found that all stars are bound to the Galaxy. We confirm that the stars do not originate from the GC. The distribution of their proper motions and radial velocities is consistent with predictions for runaway stars ejected from the Galactic disk by the binary supernova mechanism. However, their kinematics are also consistent with old disk membership. Moreover, most stars have rather low metallicities and strong α-element enrichment, as is typical for thick disk and halo stars, whereas the metallicity of the three most metal-rich stars might indicate that they are runaway stars from the thin disk. One star shows halo kinematics, but none classified as a HVS. Hence, we still have to await the discovery of the first HVS of low mass.

The Hyper-MUCHFUSS survey aims at finding high-velocity potentially unbound hot subdwarf stars. As for the G and K type sample, proper motions are determined and the trajectories are traced back to the Galactic disk in different mass models.

We present the kinematical analyses of the fastest unbound star in our Galaxy, the compact helium star (He-sdO) US 708, for which the reconstruction of its trajectory both from our ground-based proper motion measurement as well as those measured with HST reveals that the GC is ruled out as the place of origin. Hence, the Hills mechanism is ruled out for US 708, although it may remain the most favoured ejection mechanism for the other HVSs. Furthermore, new spectroscopic observations allowed us to show that US 708 is a fast rotator and therefore it is most likely the ejected donor remnant of a thermonuclear supernova, spun up by tidal interaction with the former WD primary.

The analysis of another He-sdO as well as three candidates among the sdB stars is also reported. The Galactic rest frame velocities range from 203 $\mathrm{km\,s}^{-1}$ to 660 $\mathrm{km\,s}^{-1}$, indicating that most likely all four stars are gravitationally bound to the Galaxy. With a temperature $T_{\mathrm{eff}} = 47000$ K and a surface gravity of $\log g = 5.7$, SDSS J205030.39$-$061957.8 (J2050) is a spectroscopic twin of the hypervelocity He-sdO US 708. As for the latter, the GC is excluded as a place of origin based on the kinematic analysis. Hence, the Hills mechanism can be excluded for J2050 as well. The ejection velocity is much more moderate (385 ± 79 $\mathrm{km\,s}^{-1}$) than that of US 708 ($998 \pm 68\,\mathrm{km\,s}^{-1}$). The binary thermonuclear supernova scenario, suggested for US 708, would also explain the observed properties of J2050 very well without pushing the model parameters to their extreme limits, as required for US 708. Accordingly, the star would be the surviving donor of a type Ia supernova.

Three sdB stars also showed extreme kinematics: one could be a HVS ejected from the GC, whereas the other two could be ejected from the Galactic disk through the binary supernova mechanism. Alternatively, they might be extreme halo stars.

Previously studied candidate SDSS J121150.27+143716.2 (J1211), a sdB HVS candidate which became highly interesting when we discovered that it has a K-type main-sequence companion, likely on a wide orbit. An unbound orbit of the system cannot be ruled out. Therefore, it is the first and yet only binary HVS candidate. All acceleration machanisms could be ruled out. The past trajectories do not point to the GC. Both the ejection from a

supernova as well as an exchange collision in a stellar cluster can be ruled out as the system would have been disrupted. The binary has either formed in the halo or was accreted from the tidal debris of a dwarf galaxy by the Milky Way. If the latter is the case, the star should belong to a stellar stream in the halo that is yet to be discovered from *Gaia* astrometry.

The *Gaia* mission will measure accurate proper motions of all stars brighter than $\sim$ 21 mag. The end-of-mission proper motions will be one or two orders of magnitude more accurate $(0.03 - 0.6 \, \text{mas yr}^{-1})$ than currently available ground-based proper motions $(\sim 1.0 - 5.0 \, \text{mas yr}^{-1})$, which will lead to a verification of the provided conclusions and it will be possible for the first to draw more detailed conclusions about the origins of HVSs.

Gaia parallaxes and the resulting distances will be more accurate than spectroscopic distances, that had to be used, for stars closer than $2 - 4$ kpc only. Hence, the tangential velocities will be known to high accuracy of the concerned stars. However, the known HVSs are all more distant than that (up to 100 kpc), which reinforce the need for detailed quantitative spectral analyses. Radial velocity follow-up of new discoveries will still require a lot of ground-based observations. *Gaia* photometry and ground-based photometric surveys (e.g. Skymapper) will allow a HVS survey of the Southern hemisphere, which is of utmost importance to study the dark matter distribution of the halo.

Contents

Chapter 1

Introduction

The many stars visible at the clear, dark nightsky have fascinated mankind of all ages. One might think the stars are forever, always the same, never changing, never moving. But there is much more happening on the sky than the layman would guess. There are variations in brightness. There are variations in positions, stars are moving, the constellations are changing over time. There are variations in the nature of stars, they are evolving, they are gaining mass or losing mass, they are merging, they are exploding violently. Stars are born and they die. Low-mass stars like our Sun live for billions of years while the most massive ones only live for a few million years. They can be accelerated or they can exchange companions in regions with high stellar densities. It is an unsettled environment out there with lots of motion. Even on timescales that can be observed within a human life. In fact, it is more as if we were sitting in a rollercoster. The earth is spinning, revolving around the Sun which in turn is revolving around the center of the Galaxy with a constant speed of roughly about $220 \, \mathrm{km \, s^{-1}}$, very much like billions of other stars in the Galactic disk. A rather boring rollercoster. There are other stars, experiencing strong accelerations on exceptional trajectories. These stars are the topic of this work.

Today we know that the Milky Way consists of a rotating disk surrounded by a spherical halo. Studying the motion of the stars in the Galaxy allows astronomers to peer back in time to study the formation and evolution of the Galaxy. Curiously, the rotation velocity of the Galactic disk appears to be constant over its whole extent. A solid body would produce $v \sim r$, whereas a Keplerian potential with the mass concentrated in the Galactic core would be described by $v \sim r^{-1}$. For the inner part of the disk, the predicted potential is consistent with the observation. As the stellar density decreases exponentially with the distance from the center one would expect the rotational velocity to decline. However, the velocity remains constant which has the consequence that invisible, nonluminous matter must exist – the dark matter. This behaviour is observed in most spiral galaxies.

Stars with extreme kinematics are test particles to map the mass distribution of the Galaxy because they integrate to Galactic potential when they travel to large distances (Gnedin et al., 2005; Yu & Madau, 2007). The most prominent stars with extreme kinematics are the stars that are no longer bound to our Galaxy – the Hypervelocity stars (HVS). The ratio of incoming versus outgoing stars provides an empirical measure of the local escape velocity as unbound stars are supposed to be on outgoing orbits only (Kenyon et al., 2008;

Perets, 2009).

The first three HVSs were discovered serendipitously in 2005 by radial velocity studies of specific stellar samples. HVS1 was discovered by Brown et al. (2005). It is a late B-type main-sequence star with $3 - 4\,M_\odot$. Soon thereafter, Hirsch et al., 2005 found US 708/HVS2, which is a helium subdwarf O star with about half a solar mass. HVS3 is a massive ($9\,M_\odot$), short-lived B-star and according to its huge distance of 60 kpc possibly originating from the Large Magellanic Cloud (LMC). This object remains unique.

Motivated by these discoveries Brown et al. (2006) initiated a search strategy for late B-type stars. This is a compromise between space volume and stellar lifetime because these stars are young and luminous. By now there are about two dozens B-type HVSs discovered in the Nothern hemisphere (Brown et al., 2009; Brown et al., 2012; Brown et al., 2014).

Low-mass stars, similar to the sun, are much more abundant, therefore solar-like HVSs should exist. However, due to their low luminosity very deep surveys are required for their discovery. The announcement of no less than 20 solar-like HVS candidates by Palladino et al. (2014) came much to our surprise. In addition Palladino et al. (2014) already state that they expect false-positive HVS detections in their sample. Therefore, we reinvestigate this sample (Chapter 5).

The existence of one HVS among the hot subluminous stars encouraged us to start a systematic radial velocity survey, the Hyper-MUCHFUSS project. We performed a spectroscopic and kinematic analysis of the most promising candidates to describe the properties of hot subdwarfs with extreme kinematics. US 708/HVS2 was revisited (Chapter 6).

This work is structured as follows: Chapter 2 gives an introduction on stellar evolution. It is focused on the types of stars that are analysed in this work. Chapter 3 describes the structure of the Milky Way and the applied analysis tools. Chapter 4 highlights the acceleration mechanisms of stars and gives a short history of the discovery of fast stars. Our analysis of main-sequence stars at high velocities is shown in Chapter 5. The analysis of hot subdwarfs at high velocities is shown in Chapter 6. Finally, in Chapter 7 an outlook for the future work is given.

Chapter 2

Stellar evolution

In a simple picture stars can be modelled as spherically symmetric gravitating gas spheres in hydrostatic equilibrium, which implies that temperature, pressure, and density decrease towards the outer layers of the star. They are fuelled by the release of gravitational energy and even more important, by nuclear reactions.

2.1 Star formation

Stars form out of collapsing gas clouds which consist mostly of hydrogen. To describe under which conditions a gas cloud, or a part of it, becomes unstable and collapses the Jeans criterion is used. Triggered by gravitational instabilities, if gas pressure cannot compensate gravity anymore, the cloud starts to contract in a runaway process as long as no other force is able to impede the collapse. Such instabilities can be for example the shockwave of a close supernova explosion, density fluctuations in the interstellar medium induced by density waves, or radiation pressure of already formed young stars.

In a general picture one can say that the greater the amount of mass that is compressed into a smaller volume and the cooler the temperature of the gas, the less stable it is against the gravitational collapse. But also magnetic fields play a crucial role in stabilizing the cloud and hence counteract the gravitational collapse. Due to the contraction the temperature and the pressure in the core of the clump increases. While the collapse stops in the core, where a state close to hydrostatic equilibrium is reached, further material is accreted from the surrounding medium, until the temperature and pressure in the core is high enough to start fusion of hydrogen to helium. The resulting radiation pressure stops the accretion of matter. A new star is formed and has reached the main sequence. Fig. 2.1 shows the Pillars of Creation, a starforming region in the Eagle Nebula photographed by the Hubble Space Telescope. Objects that do not exceed a mass of $0.08\,M_\odot$ are not able to sustain nuclear fusion of hydrogen except for a short episode of deuterium burning. These substellar objects are called brown dwarfs. After a short burning phase of only light elements (deuterium and lithium) they simply get fainter.

As cloud masses are much larger than stellar masses ($10^2 - 10^5\,M_\odot \gg 0.1 - 10^2\,M_\odot$), stars are supposed to form in clusters. The cloud fragments into smaller clumps. Especially massive stars can only form in associations, as they result from the collapse of giant

Figure 2.1: Pillars of Creation – starforming region in the Eagle Nebula. The photograph was taken by the Hubble Space Telescope – NASA, ESA, and the Hubble Heritage Team (STScI/AURA)[1]

clouds. Observations of protostars show that binary and multiple systems predominate the endproducts of the fragmentation ($> 60\%$).

2.2 Main sequence

Most stars in the Hertzsprung-Russel-Diagramm (HRD), the most important diagram in stellar astrophysics, are located on the main sequence, a continuous and distinctive band that is covering the whole spectral range of stars, ranging from the hot and luminous high-mass O stars to the faint and cool low-mass M stars (see Fig. 2.2). These stars are burning hydrogen to helium in their cores. Stars spend most of their lifetime on the main sequence as they almost entirely consist of hydrogen but the evolution timescales decrease strongly with increasing stellar masses. The higher the pressure and temperature are in the core the higher the fusion rate. Hence, low mass stars with low luminosities stay on the main sequence for billions of years, while the most massive stars with high luminosities stay there only for a few million years or less. The time τ spent on the main sequence can be estimated by the mass of the star M and its luminosity L: $\tau \propto M/L$.

---

[1]http://hubblesite.org/newscenter/archive/releases/2015/01/image/c/warn/
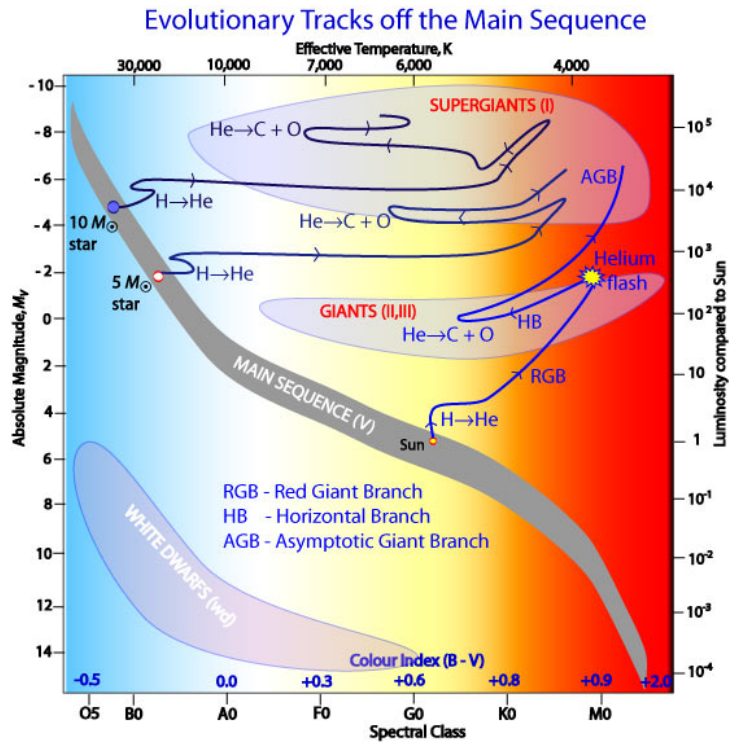
Figure 2.2: Hertzsprung-Russell-Diagramm (Australia Telescope Outreach and Education[2])

There are two different ways of fusioning four protons into one ^{4}He nucleus, the proton-proton (pp) chain and the carbon-nitrogen-oxygen (CNO) cycle. Usually both reaction chains occur simultaneously but which process is the dominant one in a star depends on its temperature. Figure 2.3 shows that for low-mass stars with low temperatures the pp chain dominates, whereas the CNO cycle dominates for the high-mass stars with high temperatures in the core.

The pp chain is already possible at the lowest central temperatures of stars ($\sim 5 \cdot 10^6$ K). The first reaction in this chain is the rarest since it requires the nuclear collision of two protons and therefore dictates the time flow for the whole reaction. During this encounter one of the protons has the chance to β^+ decay into a neutron. Helium (^{3}He) is formed when another proton is captured. This reaction is getting relevant when the core temperature exceeds $5 \cdot 10^6$ K. Until a temperature of $8 \cdot 10^6$ K is reached more ^{3}He is produced than consumed. With increasing temperature the reaction chains pp II and pp III get more importance (see Fig. 2.4).

In the CNO cycle isotopes of the elements carbon, nitrogen, and oxygen act as catalysts and are produced and destroyed in two independent cycles, the CN cycle and the CO cycle. Due to different reaction rates, the concentration of the different isotopes remains unchanged and reach their equillibrium abundance only at a temperature of about $15 \cdot 10^6$ K (see Fig. 2.5).

---

[2]http://www.atnf.csiro.au/outreach/education/senior/astrophysics/stellarevolution_postmain.html
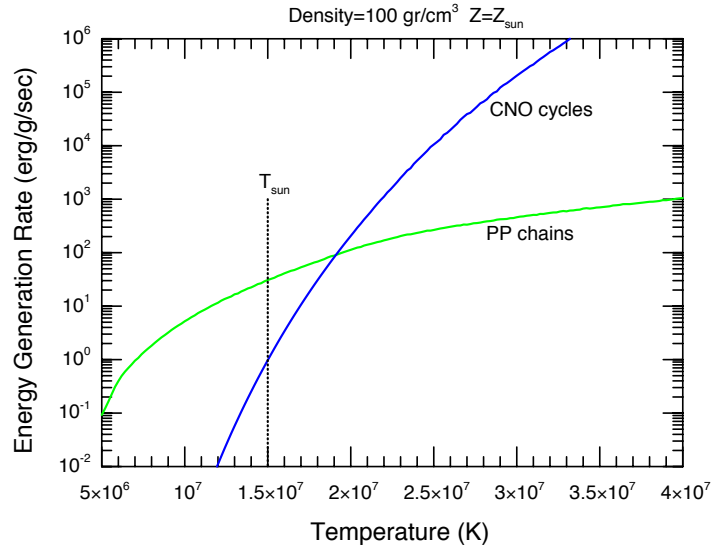
Figure 2.3: Dependency of energy generation rate of the different reaction chains of the temperature (Australia Telescope Outreach and Education[3])
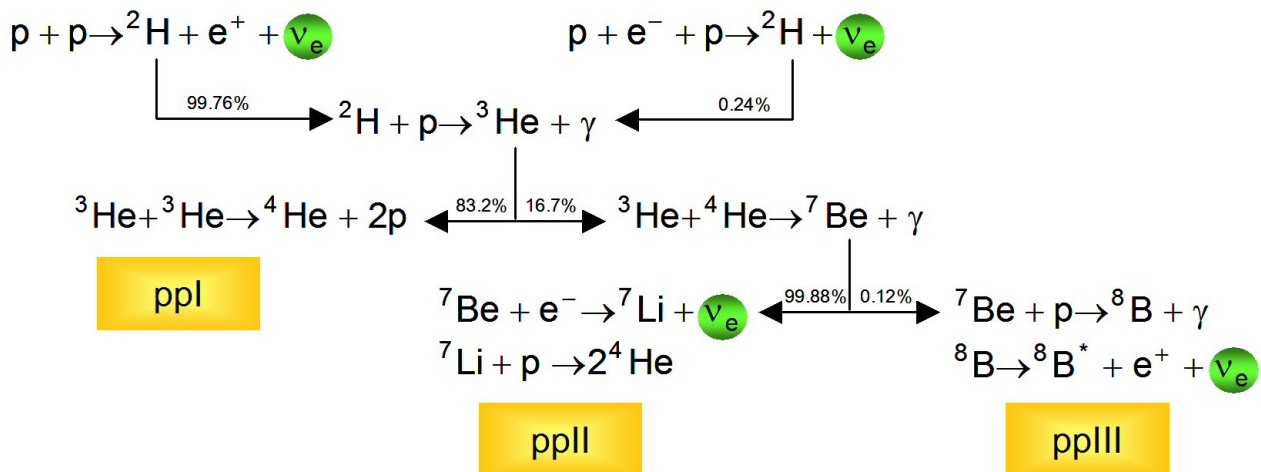
Figure 2.4: Representation of the pp chain
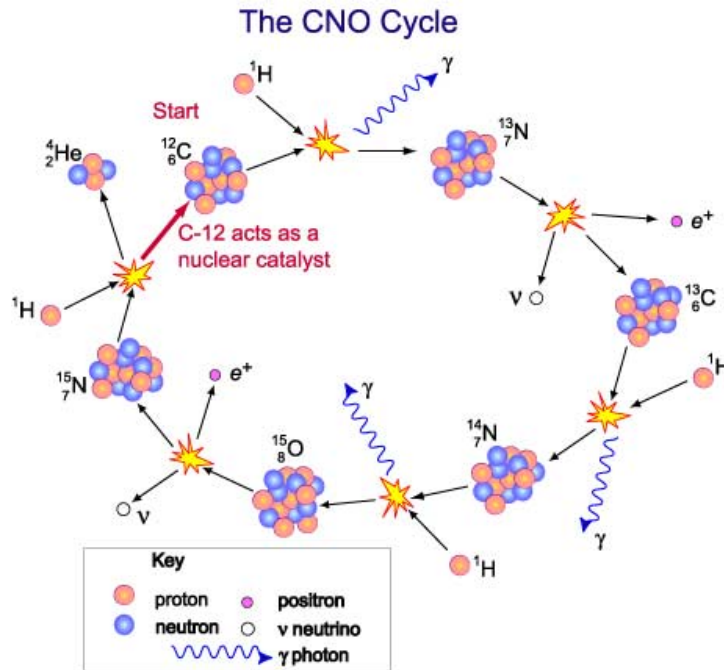
Figure 2.5: Representation of the CNO cycle[4]

2.3 Post main sequence

The ash of the hydrogen burning – helium – is accumulating in the core of the stars. As soon as the star has consumed all of its hydrogen fuel in the core the fusion zone will relocate to a shell around the core. The core itself contracts and heats up due to the release of gravitational energy. This also heats up the shell around the core which increases the fusion rate. Hence, more energy is produced in the shell-burning phase than in the core burning on the main sequence. The envelope of the star expands, and so does the luminosity, and the star climbs up the Red Giant Branch (RGB). The further evolution of the star depends on the initial mass.

The electron gas in the core of stars with masses $0.5\,M_\odot < M < 2.5\,M_\odot$ reaches a state of degeneracy due to the Pauli exclusion principle which states that no more than one fermion can occupy the same quantum state. The pressure of the electron gas no longer depends on the temperature and dominates the total pressure. Further energy input cannot be compensated via expansion. Temperature increases fast and the fusion from helium to carbon starts in an explosion at the tip of the RGB – the so-called helium flash. The large amount of energy that is released in the flash gets absorbed by the overlaying layers, causes some mass loss and the star drops down onto the Horizontal Branch (HB). The star now

---

[4]http://www.atnf.csiro.au/outreach/education/senior/astrophysics/stellarevolution_mainsequence.html

has a helium burning core and a hydrogen burning shell around it. The HB is a horizontal band in the HRD as the luminosity of both, low-mass and intermediate mass stars is very similar. It is crossing the main sequence in an area where main sequence stars are located with masses of about $3\,M_\odot$. The effective temperature on the HB increases for low-mass stars with decreasing envelope mass. Stars that have undergone huge mass losses during their RGB phase can be found on the Blue Horizontal Branch (BHB) or even the Extreme or Extended Horizontal Branch (EHB). The hotter they are the closer the helium burning core is to the surface.

The star stays on the HB until the helium in its core is exhausted. After that the helium burning relocates into a shell and again the star expands and climbs up the Asymptotic Giant Branch (AGB). The ash of the helium burning mainly consists of ^{12}C and ^{16}O. The star is not massive enough to start further nuclear burning stages. Instead it will eject its outer layers in several stages of mass loss due to shell flashes or envelope pulsations and exposes its hot core. With the loss of the envelope, the shell burning of hydrogen and helium will extinguish. When the remaining core has a surface temperature higher than 25000 K the ejected gas will be ionised by the ultraviolet radiation and will become visible as a planetary nebula. The star itself will evolve to a CO or NeOMg WD, depending on the initial mass with a maximum final mass of 1.4 $M_\odot$. This value is known as the Chandrasekhar limit and is the maximum value of a completely degenerated core as a consequence of Pauli's exclusion principle for fermions. The pressure of the degenerated electron gas stabilises the star that has reached hydrostatic equilibrium. As there is no energy production left in the star it will cool down with time, which takes billions of years as WDs have very small surface areas.

In stars with masses $> 2.5\,M_\odot$ the helium burning starts in hydrostatic equilibrium. In stars with masses $< 8\,M_\odot$ also the carbon core is degenerated. Most probably the star does not survive the carbon flash. But it is still possible for stars with such masses to evolve to a WD if it is undergoing huge mass loss episodes.

If stars are heavy enough ($M > 8\,M_\odot$) they are experiencing over and over again an exhaustion of the fuel in the core, relocating of the burning zone into a shell around the core, contraction of the core and ignition of the next burning stage. In shorter time intervals the star is going through carbon, oxygen, neon burning until the burning of silicon to iron. Iron has the largest binding energy per nucleon and therefore no more energy is released from further fusion reactions. This sets an end to stellar energy generation from fusion. The collapse in the central region will not be stopped by the ignition of the next fusion stage and the stellar core collapses and initiates a supernova explosion (see Sec. 2.5).

2.4 Blue straggler

Globular clusters are good objects to study populations of old stars. All stars are supposed to have the same age. To determine the age of the cluster one simply has to determine the turn-off point of the main sequence in the HRD. The most massive stars in the cluster first start to evolve away from the main sequence followed by the less massive ones. Stars in a globular cluster above the turn-off point have already evolved away from the main sequence, stars below are still on the main sequence. However, stars located on the main sequence above the turn-off point have been discovered in globular clusters (see Fig. 2.6). These stars
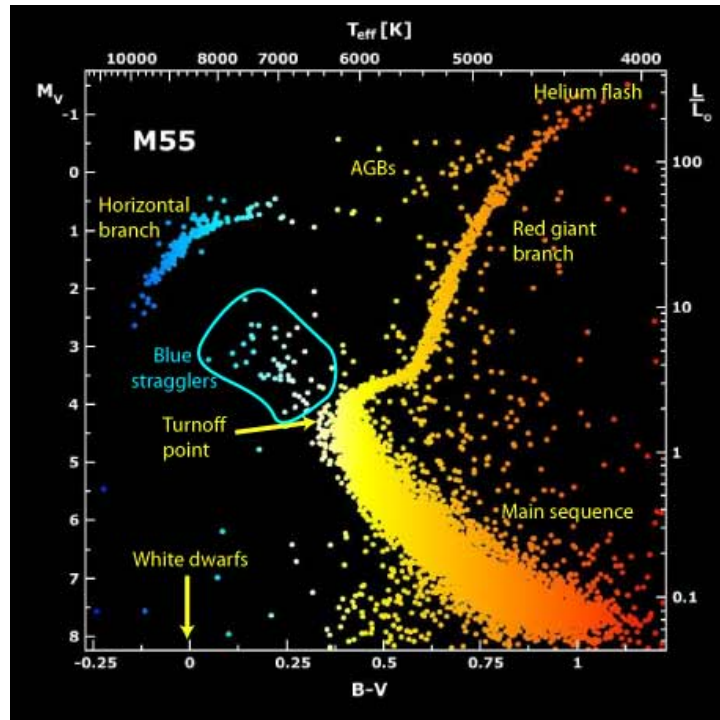
Figure 2.6: HRD of globular cluster M55 highlighting the position of blue stragglers[5]

are called blue stragglers. Two scenarios for the formation or rejuvenation of these stars have been suggested: Mass transfer in binaries and the merger of two stars. Ferraro et al. (2009) found two different sequences of blue stragglers in M30 and suggested that the bluer population is the result of stellar collisions due to the core collapse of the cluster, while the redder population stems from mass transfer in close binaries. This shows that both formation scenarios appear to be valid.

In globular clusters the blue stragglers are easy to detect, as they are located on the extension of the main sequence beyond the turn-off point. Contrary, it is difficult to identify field blue stragglers as they look like normal main sequence stars. To tell if the star should have already evolved away from the main sequence one has to determine its age. Blue metal-poor stars with main sequence luminosities are supposed to be older than their metal-rich counterparts. This may be a hint that the star was rejuvenited. If the kinematics of the star are known flighttime considerations can be made as the star has to have traveled the distance from its birthplace to its current within its lifetime.

2.5 Supernovae

Supernovae are classified by their light curve and their spectra. If hydrogen is present in the spectrum it is of type II, if not it is of type I. Type I are subdivided into Ia (silicon), Ib (no silicon, helium), and Ic (no silicon, no helium). Supernovae of type II, Ib, and Ic form via the same mechanism – the core collapse of a massive star.

---

[5]https://astrobites.org/2011/10/27/its-not-easy-being-blue/

2.5.1 Core collapse supernovae

When a massive star has reached silicon burning there is no source of thermonuclear energy left. The result is a star with an onion like structure of burning shells and a growing iron core in its center. The iron core is mainly stabilized by degenerate electron gas, with a rather small contribution of radiation pressure. Above a temperature of $5 \cdot 10^9 - 10^{10}$ K the thermal photons have enough energy to photodesintegrate the iron nuclei into neutrons and ^{4}He. The latter is further desintegrated into protons and neutrons. The compressibility increases and the interior hydrostatic equlibrium is disturbed because the photons that desintegrate the material decrease the radiative pressure. The central region is reaching densities so high that neutronization of the matter is possible. Protons and electrons form neutrons and electron neutrinos which leads to a free-fall collapse because the stabilizing pressure of the degenerate electron gas decreases rapidly. After a while the core consists almost entirely of neutrons and gets incompressible as a consequence of Pauli's exclusion principle for fermions. A proton-neutron star within the dying star is formed.

The infalling material gets decelerated on the surface of the neutron star which bounces back and generates outgoing shock waves. Its energy would be already exhausted after a few kilometers. But the waves regain strength by the ignition of higher nuclear burning stages or by supporting already existing ones. At the beginning of the collapse neutrinos are still able to leave the star unobstracted. But the densities reached in the shock waves are high enough that the weakly interacting high energy neutrinos from the core deposit additional energy into the material that the shock waves reach the outer layers. The envelope gets ejected and leaves a neutron star behind. If not enough energy is deposited in the envelope and the shock wave does not reach the surface of the star further material falls into the central region. If the limiting mass of a neutron star (Tolmann-Oppenheimer-Volkoff limit of about $2 - 3 \, M_\odot$) is reached the neutron star collapses to a black hole. The timescale of the final collapse is of the order of milli seconds. It is suggested that the type Ib and Ic stem from very massive stars collapsing to black holes. For these stars their strong stellar winds are no longer negligible during their evolution. The wind is so strong that stars that explode in a type Ib supernova have lost their entire hydrogen envelope while the ones exploding in a Ic additionly have lost their helium envelope.

Core collapse supernovae are an important source to enrich the interstellar medium with heavier elements beyond iron for the next generation of stars to form. The high density of neutrons leads to a rapid capture of neutrons by iron seed nucleii. Highly unstable nucleii are produced which subsequently beta decay into stable nucleii.

2.5.2 Thermonuclear supernovae

A different mechanism is leading to a supernova of type Ia (SN Ia). It is the thermonuclear explosion of a carbon-oxygen (CO) WD that has reached the Chandrasekhar mass limit of $1.4 \, M_\odot$ and does not leave any remnant. This makes this kind of supernovae so special. As they are supposed to take place under very similar conditions they are important standard candles to measure the structure of the universe. These measurements were awarded by the Nobel Prize in 2011 "for the discovery of the accelerating expansion of the Universe through

observations of distant supernovae"[6]. But one has to bear in mind that there exist some issues in understanding both, the progenitor evolution as well as the explosion mechanism.

When a CO WD accretes matter from a close companion the increasing weight heats up the core. The degeneracy pressure is independent of the temperature. The WD therefore cannot regulate the temperature by expanding. Once fusion of carbon has ignited, the WD heats up even more which leads to a runaway process of fusion reactions. The released energy is large enough to unbind the star and it explodes.

The single degenerate scenario starts with a binary of two main sequence stars. The more massive star first evolves to a red giant. If the two stars then share a common envelope, the system will lose a significant amount of mass. The orbital radius and period will shrink and the primary will evolve to a WD. Now the secondary evolves to a red giant and can donate matter to the WD via Roche-lobe overflow or a common envelope develops. Depending on the orbital separation of the system this can also already happen sooner if the secondary has just become a subgiant or even, if the orbit is small enough, a main sequence star. By the accretion of the material of the secondary it is possible that the WD reaches the Chandrasekhar limit. The accretion of H-rich material is commonly thought to cause classical and symbiotic novae. The absence of hydrogen lines in the spectra of SN Ia argues in favour of a loss of hydrogen rich material during the prior evolution.

In the double degenerate scenario both, the primary and the secondary have evolved to a WD and merge and the combined mass exceeds the Chandrasekhar limit. The two stars do not have to be born together. Collision in globular clusters can also produce WD-binaries on close orbits that shrink through the loss of angular momentum by the emission of gravitational waves and subsequently merge. This leads to the problem that conditions are not as similar as required for standard candles, as the total mass may exceed the Chandrasekhar mass. Observations also show that SN Ia are not as homogenous as believed previously.

The sub-Chandrasekhar scenario proposes the explosion of a SN Ia almost independent of the initial mass of the WD. When helium is accreted at an appropriate rate ($10^{-8}\,M_\odot\,\mathrm{yr}^{-1}$) the ignition of helium burning starts violently after about $0.15\,M_\odot$ have been accreted. This could result in a subsequent detonation and a compression wave moving inwards, causing the detonation of carbon (Fink et al., 2010; Kromer et al., 2010). Geier et al. (2013) discovered a progenitor system which fullfills all requirements for this scenario: CD–30° 11223 is an extremely close, eclipsing binary system ($P \sim 1.2\,\mathrm{h}$) where a WD is orbited by a core helium burning compact hot subdwarf star. In about 10 Mio years the subdwarf will start to transfer helium-rich material after the orbit has shrunk due to emission of gravitational. This star will be discussed in Section 6.2.

2.6 Formation of hot subdwarfs

Hot subdwarfs – subluminous stars of spectral type B and O (sdB, sdO) – can be found on the EHB in the HRD (see Fig. 2.7) and were first discovered in the photometric survey of the North Galactic pole region by Humason & Zwicky (1947) in the 1950s (Greenstein, 1956; Münch, 1958). They are helium core burning stars surrounded only by a very thin envelope

---

[6]http://www.nobelprize.org/nobel_prizes/physics/laureates/2011/press.html
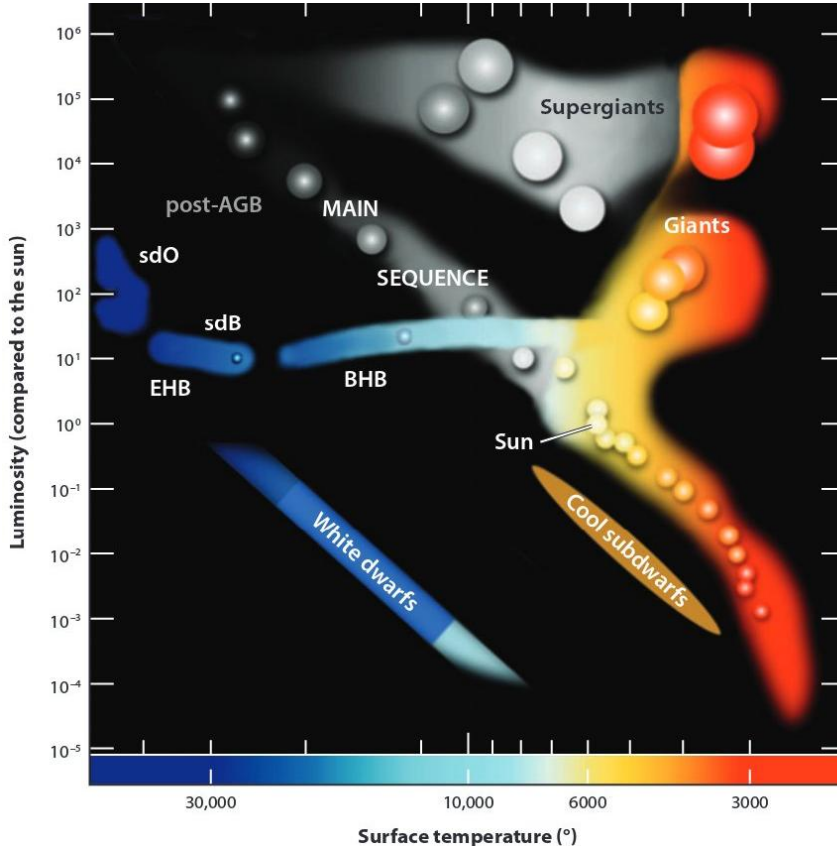
Figure 2.7: HRD showing the position of sdB and sdO stars, from Heber (2009).

that is not able to sustain hydrogen shell burning like the cooler HB stars. The hotter the star the thinner the envelope and the closer the helium burning core is to the surface. Normal HB stars are supposed to reascend the AGB in their future evolution. Instead, EHB stars will evolve directly to the white dwarf cooling sequence after the consumption of their helium fuel, avoiding a second red giant phase.

There are still aspects of the formation of hot subdwarfs that are unclear. This especially applies for the extreme mass loss the progenitor star has to undergo during the RGB phase to leave a helium core of about half a solar mass that is almost completely stripped of all hydrogen. The layer of hydrogen is so thin that the star is unable to maintain hydrogen-shell burning ($M_{\mathrm{env}}/M_{\mathrm{sdB}} \simeq 10^{-3}$).

As a large fraction (40-70%) are members of close binaries, binary evolution scenarios are favoured over single evolution scenarios to explain the formation of sdB stars. The observed periods range from 0.05d to 30d (Maxted et al., 2001; Morales-Rueda et al., 2003; Copperwheat et al., 2011; Geier et al., 2015b) while most of the companions are found in the shortest period systems. The companions are mostly WDs, but low mass main sequence stars are also found quite often. Candidates for very massive companions like neutron stars or black holes may also exist (Geier et al., 2010; Mereghetti et al., 2011). Charpinet et al. (2011) discovered a candidate for two close earth-sized planets, which shows that such objects might also play a role in the formation of hot subdwarfs.

Fig. 2.8 shows three different evolution channels that result in sdB binaries with different types of companions. The first two channels involve the formation of a common envelope that surrounds both stars following a phase of unstable Roche-lobe overflow when one of the stars evolved to a red giant. In the first scenario the primary has evolved to a WD already before the secondary evolved to a red giant and the common envelope developed. During the common envelope phase the separation of the system shrinks due to friction. During the spiral-in phase of the core of the red giant and the more compact companion due to friction, the released orbital energy is deposited in the envelope which leads eventually to an ejection of the latter. Therefore, both scenarios lead to subdwarfs in short period binaries, either with a WD or a main sequence star companion but a large diversity of end configurations are conceivable, depending on the initial separation, mass ratio and evolutionary stage of the companion (see Heber, 2009, 2016).

In the last channel of Fig. 2.8 the mass transfer is stable and no common envelope is formed. This leaves the separation of the system almost unchanged and results in a wide binary of a subdwarf with a F to G type main sequence or subgiant companion. To form single subdwarfs the engulfment and the possible subsequent destruction of a substellar object within the common envelope phase such as brown dwarfs and planets is suggested (Soker, 1998; Nelemans & Tauris, 1998).

A subclass of helium rich sdO/Bs exists which is mostly consisting of single stars (Napiwotzki, 2008). To form these kind of objects the merger of two helium WDs driven by gravitational wave radiation and ignition of helium core burning (Webbink, 1984; Iben & Tutukov, 1984) or a delayed helium-core flash on the WD cooling sequence (Lanz et al., 2004; Miller Bertolami et al., 2008) were suggested.
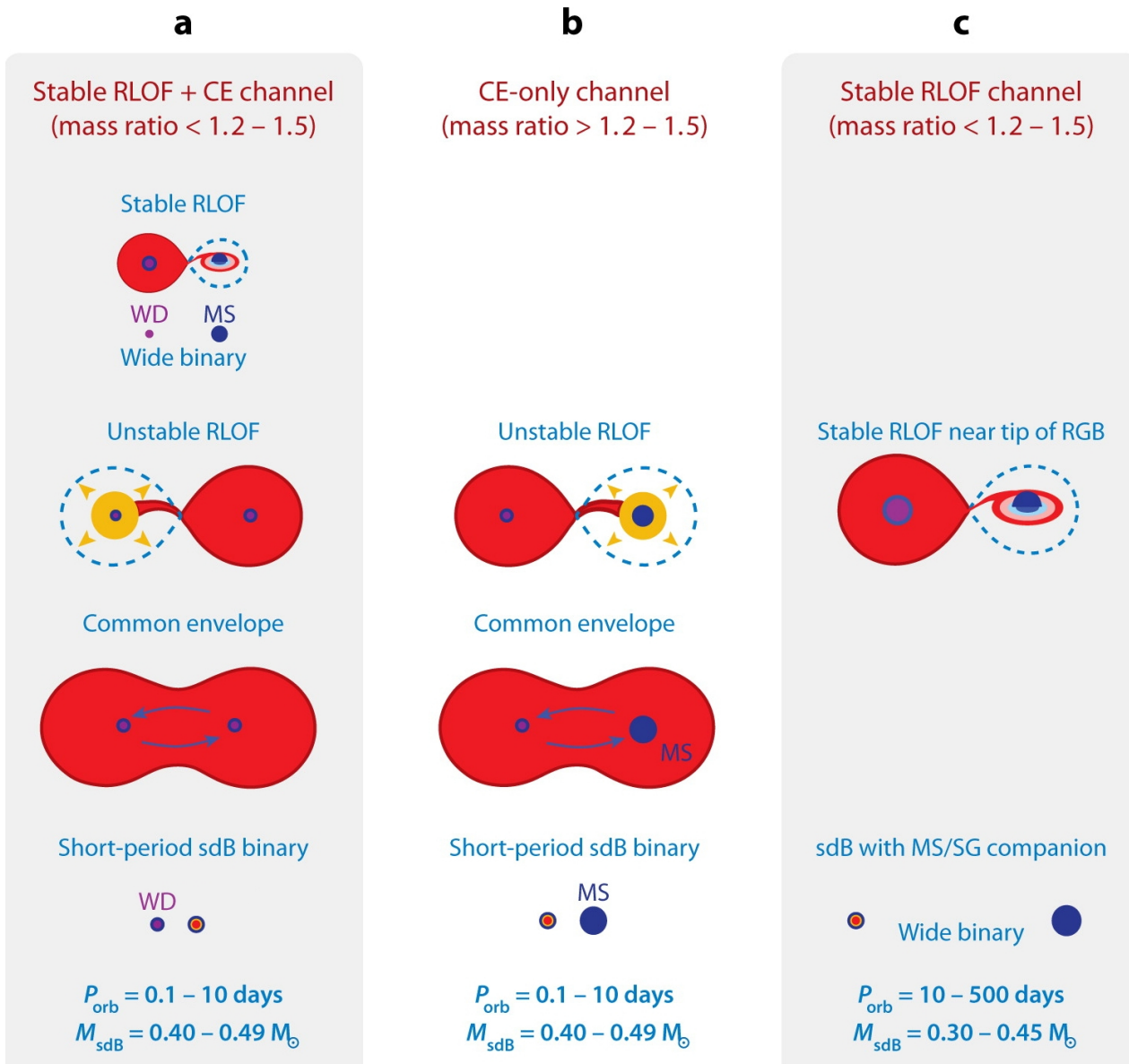
Figure 2.8: Formation channels of subdwarfs in binary systems, from Heber (2016)

Chapter 3

The Galaxy

Our Galaxy, the Milky Way, is a barred spiral galaxy and consists of three major parts: barred bulge, disk, and halo (see Figure 3.1). In the center resides a SMBH with a mass of about four million $M_\odot$. The gas and stellar density increases towards the GC. Therefore, the SMBH itself is obscured in the optical but can be studied in the infrared. It can be associated with the bright radio source Sgr A*, which is surrounded by a massive young star cluster. The nuclear cluster is the so-called S-star cluster consisting of several main-sequence B-type stars orbiting the GC, the so-called S stars (see Figure 3.2). Their orbits are eccentric and randomly oriented on solar system scales. Monitoring the orbit for about two decades allowed to determine the mass of the SMBH (Ghez et al., 2005, 2008; Gillessen et al., 2009; Genzel et al., 2010). Figure 3.3 shows the orbits of a number of the S-stars.

Contrary, the surrounding bulge with an extent of about 3 kpc is dominated by old, low-mass stars. The bulge is embedded in a rotating disk with a radius of about 30 kpc. It consists of stars, gas, and dust and can be divided into a thick and a thin disk. The thin disk has a height of about $0.1 - 0.2$ kpc and contains the solar neighbourhood and the youngest stars in the Milky Way. In its spiral arms, where the interstellar medium is densest, stars are continuously formed. They form in associations and open clusters which are relatively quickly dissolved. The thick disk has a height of about 2 kpc and contains of older and therefore more metal-poor stars.

These components are surrounded by a huge spherical halo with a radius of more than hundred kpc. It is not dense enough for star formation to take place but it contains some of the oldest objects of the Milky Way: Globular clusters, objects that are stable and gravitationally bound which consist of several $10^4 - 10^6$ stars. The mass of the halo is supposed to be dominated by dark matter, as the visible mass is by far not sufficient to explain the observed flat Galactic rotation curve.

Constructing Galactic trajectories of stars is an important task in the analysis of hyper-velocity star candidates. The results offer information about the stars' origin and the kind of ejection event. For the calculation of the stellar orbits the knowledge of the three components of their current coordinates and velocity components is of prime importance. Additionally, it is also required to have a reliable model of the Galactic gravitational potential at hand.
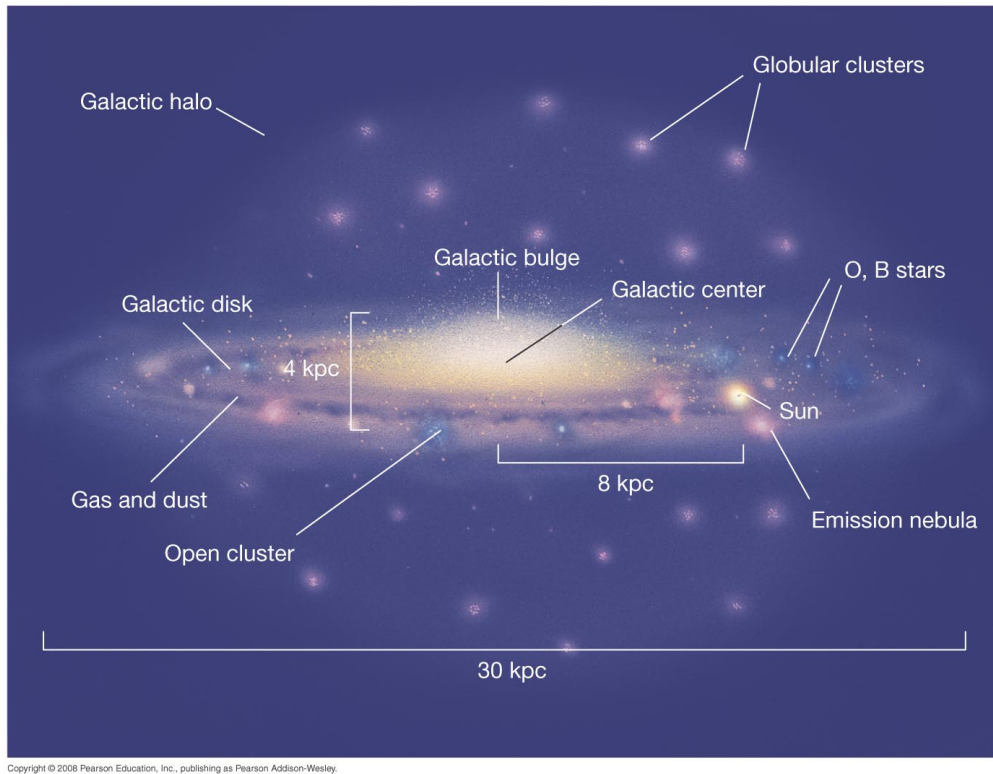
Figure 3.1: Schematic structure of the Milky Way.
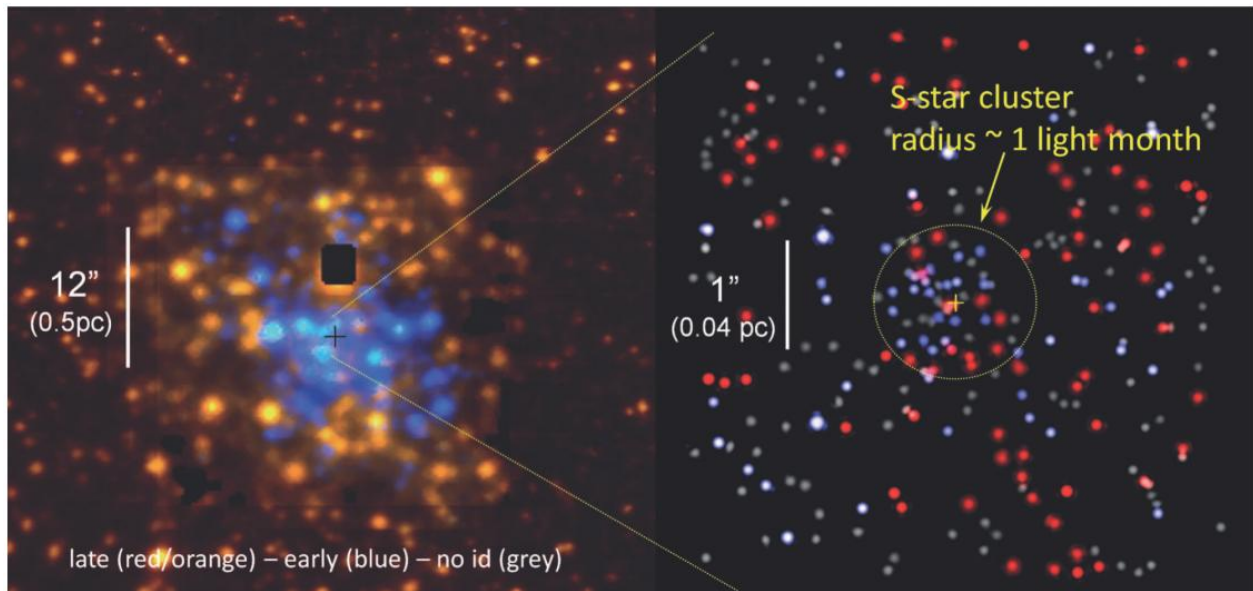
Figure 3.2: Distribution of early-type stars (blue) and late-type stars (red/orange) in the central region of the Galaxy (left ~ 1 pc, right ~ 0.8 pc), from Genzel et al. (2010).
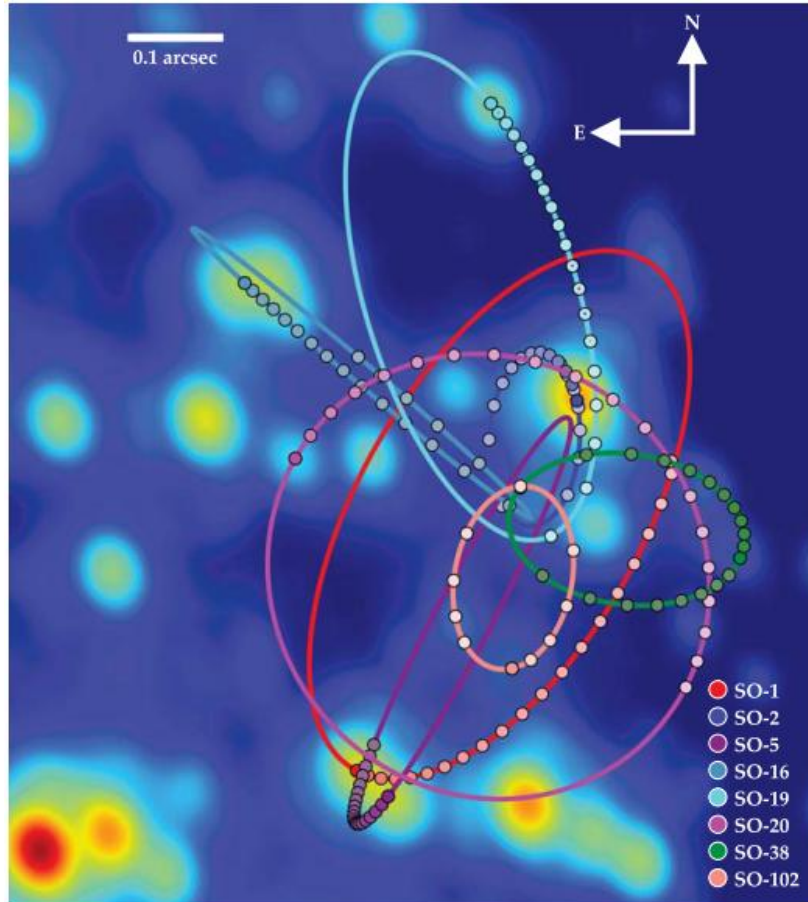
Figure 3.3: The orbit of S-stars. The coloured dots show the stars' annual average positions, measured between 1995 and 2014. The colour saturation increases with time, from Brown (2016).

3.1   Distance determination

For each object on the sky the coordinates in the equatorial coordinate system – right ascension α and diclination δ – can be measured to very high precision. To know the spatial position of a star one additionally has to determine the distance of the star to the Sun.

3.1.1   Parallax

Because the Earth revolves around the Sun a nearby object shows an apparent shift of position compared to the reference background of distant objects, the parallax effect. The parallax angle π is related to the distance as

$$d = 1/\pi \tag{3.1}$$

By definition, an object that shows a parallax angle of one arcsec has a distance from the Sun of one parsec (pc). However, parallaxes are only measureable for objects as close as the solar neighbourhood. Even the HIgh Precision PARallax COllecting Satellite (Hipparcos) was able to measure significant parallaxes up to a distance of about 500 pc only. Therefore,

no useful parallaxes are available for the stars of this work because they are all much further away. Other techniques are necessary for these distant objects.

3.1.2 Spectroscopic distance

A quantitative analysis of the spectrum of a star provides the atmospheric parameters T_{eff}, surface gravity $\log g$, projected rotational velocity $v_{\text{rot}} \sin i$, helium and metal abundances. State-of-the art synthetic model spectra are fitted simultaneously to the visible absorption lines of the observed spectra by means of χ^2-minimization. Depending on the nature of the star one can either use a canonical mass or a mass which is received from the comparison of the atmospheric parameters with stellar evolution models for the determination of the stellar radius. The apparent magnitude then allows us to derive the spectroscopic distance. The magnitudes have to be corrected for interstellar reddening. The reddening can either be obtained from reddening maps or byfitting the observed magnitudes to spectral energy distribution (SED).

3.1.3 Photometric angular diameter

Another way of obtaining the distance employs photometry. Observed magnitudes in different bands are compared to synthetic SEDs which is the emitted energy as a function of wavelength of a source, which allows the effective Temperature T_{eff}, the interstellar extiction and an estimate of the angular diameter to be determined. In order to derive the distance, however, the stellar radius needs to be known. It can be determined from the spectroscopic gravity assuming an appropriate mass or from theoretical evolution models.

3.2 Radial velocity measurement

The radial velocity can also be obtained from the spectrum of a star. The radial velocity arises as a Doppler shift. The absorption lines of a stars moving away from the observer are shifted to redder wavelengths. For a star that is approaching they are shifted to bluer wavelengths. It can be measured by fitting a set of mathematical functions (Gaussians, Lorentzians and polynomials) to match continuum, line, and line core to mimic the typical Voigt profile of spectral lines using the FITSB2 routine. The profiles are fitted to all suitable lines simultaneously using χ^2-minimization and the radial velocity shift with respect to the rest wavelength is measured. An object with negative radial velocity is moving towards the observer while a positive radial velocity stands for a movement away from the observer.

3.3 Proper motions

The transversal velocities can be derived from proper motion and distance. Accurate proper motions are therefore very important for the kinematic analysis of stars but difficult to measure to the required accuracy. Astrometric catalogue values from surveys are not always at hand, or the different catalogues give inconsistent results. Some outliers are obvious others

are not. Therefore, we measure our own proper motions whenever possible and compare them to available catalogue values.

For a given speed perpendicular to the line-of-sight, the proper motion will be smaller the further away the star is. Distant Extragalactic objects like galaxies or quasars show no measureable proper motion. They may therefore be used as a reference system. In contrast to the cyclic nature of the parallax, proper motions have advantage of being cumulative. Therefore, small annual displacements can be detected from measurements performed with large timebases. However, one has to take great care in the selection of the reference system. As the Galaxy rotates an extragalactic reference frame is the ideal choice.

3.3.1 Proper motion measurements

To determine the proper motion we use all available early epoch digitized photographic plates that are made accessible by the Digitised Sky Survey (DSS)[7]. These are combined with those obtained from the data bases of modern digital surveys such as SDSS[8], Super Cosmos[9], and VHS[10]. This provides a timebase of about 60 years.

The most commonly used photographic plates in this work are: The oldest plates are the most important images for our purposes as most of our stars are very distant and the proper motions are small. Therefore we need a long timebase. These photographic plates are the ones from the First Palomar Observatory Sky Survey (POSS I). Two images were taken in the 1950s with a 1.2m Schmidt telescope, one with a red emulsion, and the other with a blue one. It covered the Northern hemisphere down to the South to a declination of $\delta = -33°$. The Quick-V Northern survey (QVN) of the Northern hemisphere was performed in the 1970s but is rather shallow and of low spatial resolution. In the 1980s the Second Palomar Observatory Sky Survey (POSS II) was performed with improved photographic plates and an additional image in the near infrared. The counterpart to the POSS in the South was performed with the 1.2m UK Schmidt Telescope at the Australian Astronomical Observatory. Three emulsions were used: blue (SERCJ) from 1979 to 1994, infrared (SERCI) from 1978 to 2002, and red (Equatorial Red) from 1984 to 1998.

For each star, positions are derived from all available images with respect to a set of faint, compact, and well-distributed background galaxies which are supposed to be distant enough to have undetectable proper motions to the accuracy of our measurements. The galaxies for the reference system are taken from the SDSS database, which automatically classifies objects by means of photometry and morphology. We use as many galaxies as possible, but exclude those that show displacements which could be true motion (if the object is misclassified in the SDSS and is in fact a foreground star). The object is then excluded in all epochs. It can also be spurious if it is detected only on certain images, which can be caused for instance by a close faint foreground star that is detected only in certain wavelength ranges, as the photographic plates are taken in different filters and the companion is only detected on some of them only. Another possibility for a shift in position of a reference object is an explosion

---

[7]http://archive.stsci.edu/cgi-bin/dss_plate_finder
[8]http://skyserver.sdss3.org/public/en/tools/chart/navi.aspx
[9]http://www-wfau.roe.ac.uk/sss/pixel.html
[10]http://www.eso.org/qi/catalogQuery/index/51

of a supernova. This event can, even if it cannot be resolved, change the position of the maximum intensity of that object which defines the position of the object itself. When shifts are only detected in isolated images, these objects are only excluded for those epochs where the shift in position occurs.

The adopted uncertainty of the object for each epoch is the average deviation of the measured positions of the reference objects to their reference value from the SDSS. Finally, a linear regression fit is performed on the derived positions to derive the two components of the proper motion in right ascension $\mu_\alpha \cos \delta$ and declination μ_δ from the slope of the regression line.

3.3.2 Proper motion catalogues

There are various catalogues available that provide proper motions. As already mentioned the values of these catalogues are not always consistent. A naive approach could be to take the mean of these catalogue values but one has to be careful. Not all of the catalogue values represent independent measurements. In fact many catalogues base on previously existing ones.

The United States Naval Observatory (USNO-B1.0) catalogue (Monet et al., 2003) obtained its data from scans from 7435 Schmidt plates taken for the various sky surveys. The Position and Proper Motions Extended Large (PPMXL) catalogue (Roeser et al., 2010) is a combination of the USNO-B1.0 catalogue and positions from Two Micron All Sky Survey (2MASS). The Fourth US Naval Observatory CCD Astrograph Catalogue (UCAC4) (Zacharias et al., 2013) relies on several other catalogues and observations. They state that no Schmidt plates were used and that this leads to a significant improvement of the proper motions north of $\delta > -20°$. That makes this catalogue a rather independent one as none of the previous mentioned here is used but unfortunately it is rather shallow with a limiting magnitude of 16. An adapted version recently became available as Fifth US Naval Observatory CCD Astrograph Catalogue (UCAC5) including the first *Gaia* data release (Zacharias et al., 2017). The SDSS DR9 (Ahn et al., 2012) is combining UCAC and USNO-B1.0 with SDSS positions. For the Hot Stuff for One Year (HSOY) catalogue (Altmann et al., 2017) positions were taken from the first *Gaia* data release and combined with the input data from the PPMXL catalogue. The APOP catalogue (Qi et al., 2015) represents an independent catalogue which is also making use of the old Schmidt plates but is paying special attention to position, magnitude and colour dependent systematic errors.

3.4 Coordinate transformations

3.4.1 Transformation to Galactic coordinates

The position of celestial objects is specified by their coordinates in the equatorial coordinate system – right ascension α and declination δ – and their distance from the Sun d. In the first step the polar coordinates of the star are converted to Cartesian coordinates using

$$c = d \cdot \begin{pmatrix} \cos\alpha \cdot \cos\delta \\ \sin\alpha \cdot \cos\delta \\ \sin\delta \end{pmatrix} \tag{3.2}$$

This Cartesian coordinate system has to be rotated and shifted to x, y, z coordinates in the right-handed, non-rotating, Cartesian Galactic coordinate system, defined by the GC being at the origin $(0, 0, 0)$, the Sun being on the negative x-axis, and the positive z-axis pointing towards the Galactic North pole. Viewed from the North Galactic pole, the Galactic disk is then rotating in clockwise direction (see Figure 3.4). Using

$$\begin{pmatrix} x \\ y \\ z \end{pmatrix} = M \cdot c + \begin{pmatrix} -d_{\odot-\mathrm{GC}} \\ 0 \\ 0 \end{pmatrix} \tag{3.3}$$

where $d_{\odot-\mathrm{GC}}$ is the distance from the Sun to the GC

$$M = \begin{pmatrix} V_{\mathrm{GC}}^T \\ V_y^T \\ V_{\mathrm{NGP}}^T \end{pmatrix} \tag{3.4}$$

$$V_{\mathrm{GC}} = \begin{pmatrix} \cos\alpha_{\mathrm{GC}} \cdot \cos\delta_{\mathrm{GC}} \\ \sin\alpha_{\mathrm{GC}} \cdot \cos\delta_{\mathrm{GC}} \\ \sin\delta_{\mathrm{GC}} \end{pmatrix} \tag{3.5}$$

$$V_{\mathrm{NGP}} = \begin{pmatrix} \cos\alpha_{\mathrm{NGP}} \cdot \cos\delta_{\mathrm{NGP}} \\ \sin\alpha_{\mathrm{NGP}} \cdot \cos\delta_{\mathrm{NGP}} \\ \sin\delta_{\mathrm{NGP}} \end{pmatrix} \tag{3.6}$$

$$V_y = -(V_{\mathrm{GC}} \times V_{\mathrm{NGP}}) \tag{3.7}$$

are the rotation matrix transformations applied to the x, z, y axes respectively (Johnson & Soderblom, 1987). For these transformations the GC coordinates $\alpha_{\mathrm{GC}} = 17{:}45{:}37.224$, $\delta_{\mathrm{GC}} = -28{:}56{:}10.23$ and Galactic North Pole coordinates $\alpha_{\mathrm{NGP}} = 12{:}51{:}26.282$, $\delta_{\mathrm{NGP}} = 27{:}07{:}42.01$ as determined by Reid & Brunthaler (2004) are adopted.

3.4.2 Transformation of velocities

For the computation of the velocities, the individual observed velocity components are converted to Cartesian coordinates separately and subsequently added to give the total velocity v_C in the cartesian system:

$$v_{rc} = v_{\mathrm{RV}} \cdot \begin{pmatrix} \cos\alpha \cdot \cos\delta \\ \sin\alpha \cdot \cos\delta \\ \sin\delta \end{pmatrix} \tag{3.8}$$
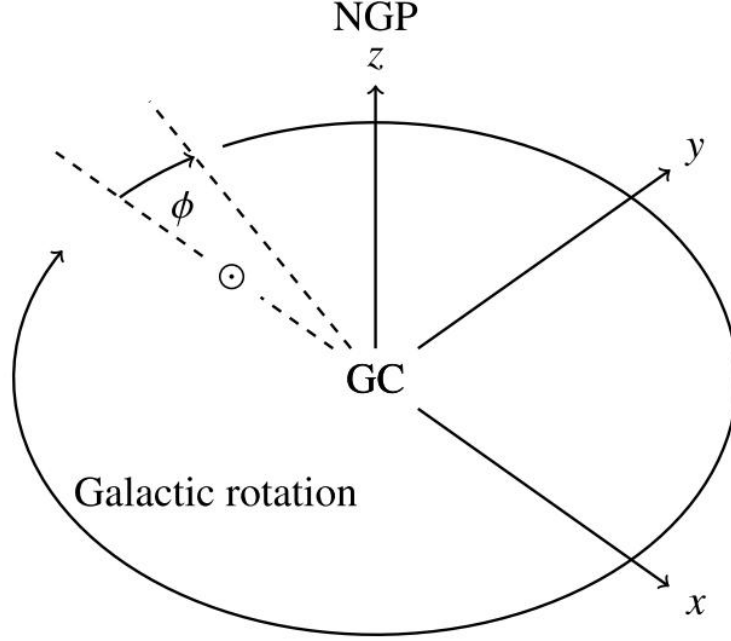
Figure 3.4: Galactocentric coordinate system used in this work, from Irrgang (2014). The position of the Sun is indicated with the solar symbol $\odot$

$$v_\delta = \mu_\delta \cdot d \cdot \begin{pmatrix} -\cos\alpha \cdot \sin\delta \\ -\sin\alpha \cdot \sin\delta \\ \cos\delta \end{pmatrix} \tag{3.9}$$

$$v_\alpha = \mu_\alpha \cos\delta \cdot d \cdot \begin{pmatrix} -\sin\alpha \\ \cos\alpha \\ 0 \end{pmatrix} \tag{3.10}$$

$$v_C = v_{rc} + v_\delta + v_\alpha \tag{3.11}$$

where v_{RV} is the measured radial velocity, μ_δ is the observed proper motion in declination, and $\mu_\alpha \cos\delta$ is the observed proper motion in right ascension. The resulting Cartesian velocity components are then transformed into velocity components v_x, v_y, v_z in the Galactic coordinate system with

$$\begin{pmatrix} v_x \\ v_y \\ v_z \end{pmatrix} = M \cdot v_C + \begin{pmatrix} v_{x\odot} \\ v_{y\odot} + v_{\mathrm{lsr}} \\ v_{z\odot} \end{pmatrix} \tag{3.12}$$

where v_{lsr} is the velocity of the local standard of rest (LSR) and $v_{x\odot}, v_{y\odot}, v_{z\odot}$ are the velocity components of the Sun in the Galactic reference frame for which we adopted the values from Schönrich et al. (2010). The total Galactic restframe velocity is then given by

$$v_{\mathrm{GRF}} = \sqrt{v_x{}^2 + v_y{}^2 + v_z{}^2} \tag{3.13}$$

The Galactic radial velocity v_r and rotational velocity v_ϕ components of the star are then respectively computed as

$$v_r = \frac{xv_x + yv_y}{\sqrt{x^2 + y^2}} \tag{3.14}$$

$$v_\phi = -\frac{xv_y - yv_x}{\sqrt{x^2 + y^2}} \tag{3.15}$$

3.4.3   Mass models

The resulting values are the input parameters for the following calculations in the model potentials. A widely used Galactic gravitational potential to calculate trajectories is the one of Allen & Santillan (1991). It has been used for various types of celestial objects, e.g., globular clusters (Odenkirchen et al., 1997; Allen et al., 2008; Lane et al., 2012), white dwarfs (Pauli et al., 2003, 2006), sdB stars (Altmann et al., 2004; Tillich et al., 2011), runaway stars (Irrgang et al., 2010; Silva & Napiwotzki, 2011), and HVSs (Hirsch et al., 2005; Edelmann et al., 2005). The model was recalibrated by Irrgang et al. (2013) using new and improved observational constraints, hereafter denoted as model I. In order to investigate the influence of the halo component on the trajectories Irrgang et al. (2013) calibrated two other dark matter halo mass models on the same observational constraints (hereafter denoted as model II and model III).

All gravitational potentials $\Phi(r, z)$ are the sum of a central spherical bulge component $\Phi_\text{b}(R)$, an axisymmetric disk $\Phi_\text{d}(r, z)$, and a spherical dark matter halo $\Phi_\text{h}(R)$, where $R = \sqrt{r^2 + z^2}$. The potential forms of bulge and disk remain the same in all three models of Irrgang et al. (2013), only the halo is changed. Disk and bulge potentials have the form proposed by Miyamoto & Nagai (1975) (the parameters M_b, M_d, M_h represent weighing factors to the contribution of their components to the total potential, and b_b, a_d, b_d, a_h are scale lengths):

$$\Phi_\text{b}(R) = -\frac{M_\text{b}}{\sqrt{R^2 + b_\text{b}^2}} \tag{3.16}$$

$$\Phi_\text{d}(r, z) = -\frac{M_\text{d}}{\sqrt{r^2 + \left(a_\text{d} + \sqrt{z^2 + b_\text{d}^2}\right)^2}} \tag{3.17}$$

In model I the halo potential is described by

$$\Phi_\text{h}(R) = \begin{cases} \frac{M_\text{h}}{a_\text{h}}\left(\frac{1}{\gamma-1}\ln\left(\frac{1+\left(\frac{R}{a_\text{h}}\right)^{\gamma-1}}{1+\left(\frac{\Lambda}{a_\text{h}}\right)^{\gamma-1}}\right) - \frac{\left(\frac{\Lambda}{a_\text{h}}\right)^{\gamma-1}}{1+\left(\frac{\Lambda}{a_\text{h}}\right)^{\gamma-1}}\right) & \text{if } R < \Lambda \\ -\frac{M_\text{h}}{R}\frac{\left(\frac{\Lambda}{a_\text{h}}\right)^{\gamma}}{1+\left(\frac{\Lambda}{a_\text{h}}\right)^{\gamma-1}} & \text{otherwise} \end{cases} \tag{3.18}$$

For $\Lambda = 100\,\text{kpc}$ and $\gamma = 2.02$, this is equivalent to the expression given in Allen & Santillan (1991). For model II the halo component is replaced by the truncated, flat rotation curve model of Wilkinson & Evans (1999):

$$\Phi_\text{h}(R) = -\frac{M_\text{h}}{a_\text{h}}\ln\left(\frac{\sqrt{R^2 + a_\text{h}^2} + a_\text{h}}{R}\right) \tag{3.19}$$

The halo component of model III is based on the universal density profile of dark matter halos suggested by Navarro et al. (1997):

$$\Phi_{\mathrm{h}}(R) = -\frac{M_{\mathrm{h}}}{R} \ln \left(1 + \frac{R}{a_{\mathrm{h}}} \right) \tag{3.20}$$

We calculate trajectories of the program stars in the three different Milky Way mass models of Irrgang et al. (2013) to trace the orbits back to the Galactic disk to obtain their dynamical properties and possible origins. Most important for the calculation is the halo mass. The range of these three models is $M_{R<200\,\mathrm{kpc}} = 1.2 - 3.0 \cdot 10^{12} M_{\odot}$. This covers a large range of published estimates for the mass of the dark matter halo. Nevertheless, we tested a fourth mass model (Rossi et al., 2017) for some of the stars in this work. This mass model shares the same disk structure (Miyamoto & Nagai, 1975), the same potential form for the halo as model III (Navarro et al., 1997) with a lower mass of the halo as adopted for model III, but a different model is used for the bulge (Hernquist, 1990). However, we recall that the mass model of Rossi et al. (2017) was calibrated to different observational constraints than the mass models of Irrgang et al. (2013), which leads to the different halo masses of the two mass models.

Long-term orbits were calculated for 5000 Myr to characterise them in the context of population synthesis. In order to constrain the place of origin, that is, to determine whether the star was ejected from the Galactic disk or centre or any other place in the Galactic plane, we traced the trajectories back to their last disk crossings and calculated the times of flight and ejection velocities for all mass models. Through a Monte Carlo simulation of a Gaussian distribution with a depth of 10^6 we calculated the kinematic properties of the stars. This is necessary rather than just calculating errors using Gauss error propagation laws because the parameters are significantly correlated. We determined all kinematic parameters of the current location of the stars as well as the values at the time and position of their last disk passage, such as velocity components in Cartesian coordinates (v_x, v_y, v_z). Velocity components in cylindrical coordinates (v_r, v_ϕ, v_z), the Galactic rest-frame velocity v_{GRF}, and the ejection velocity v_{ej} corrected for the Galactic rotation were also calculated for each of the mass models.

3.5 Classification of Galactic orbits

If a star is found to be bound to the Galaxy, it may not be an ejected star, but a member of an old stellar population (i.e. the halo) with extreme kinematics. In order to decide to which Galactic stellar population the stars of interest belong several criteria can be used. According to Pauli et al. (2006), stars can be assigned to the populations of the different components of the Milky Way - thin disk, thick disk, halo - using four different criteria. Those criteria have been calibrated using a suitable calibration sample of 291 main-sequence F and G stars for which the population membership can be determined from spectroscopically measured metallicities (Pauli et al., 2006).

The first is the classification by their position in the $v_r - v_\phi$-velocity diagram, where v_r is the Galactic radial component, which is negative towards the GC, while v_ϕ is the Galactic rotational component. Figure 3.5 shows the $v_r - v_\phi$-velocity diagram from Pauli et al. (2006).
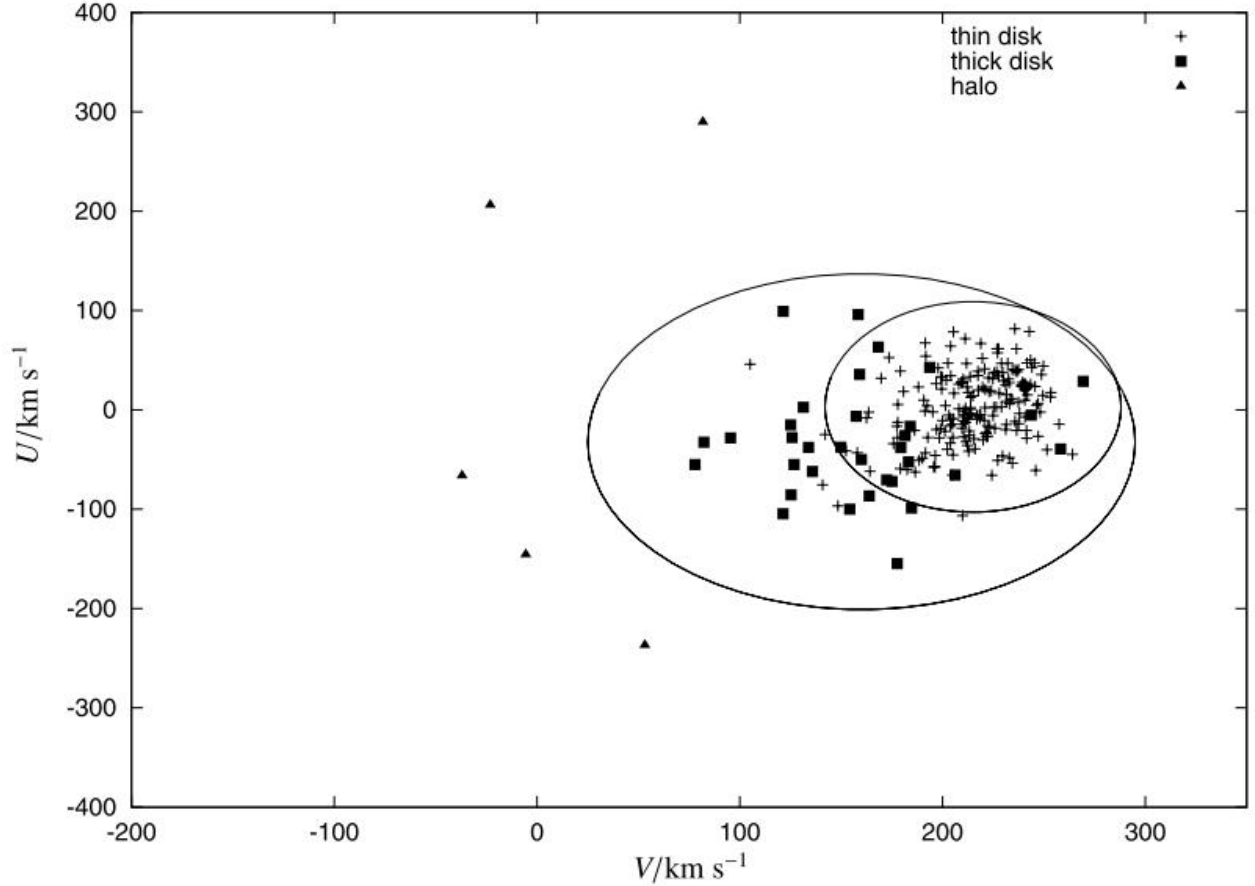
Figure 3.5: $v_r - v_\phi$-velocity diagram for the calibration sample from Pauli et al. (2006) ($U = v_r$ and $V = v_\phi$). The ellipses are 3σ-thin disk (inner) and 3σ-thick disk (outer) contours.

Stars that are revolving on retrograde orbits around the GC have negative v_ϕ. Disk stars are located in a well-defined region. Thin disk stars have roughly $|v_r| \approx 100$ km s^{-1} and v_ϕ ranges from 150 km s^{-1} to about 280 km s^{-1}. The area of the thick disk is larger. Thin disk stars have roughly -200 km s^{-1} $\lesssim v_r \lesssim$ 150 km s^{-1} and v_ϕ ranges from 0 km s^{-1} to about 300 km s^{-1}. Thin and thick disk overlap and have to be distinguished by additional criteria. Stars that are outside this region are assumed to belong to the Galactic halo.

The second diagnostic tool is the $J_z - e$-diagram. Figure 3.6 shows the $J_z - e$-diagram from Pauli et al. (2006). Stars on retrograde orbits have positive angular momentum J_z[11]. Thin-disk stars are located at the top left end of the diagram, having very low eccentricities e and negative J_z (Region A). Tillich et al. (2011) suggested that stars inside an area of $0.3 \lesssim e \lesssim 0.7$ and -2000 kpc km s^{-1} $\lesssim J_z \lesssim -1000$ kpc km s^{-1} belong to the thick disk (Region B), while halo stars are located in Region C.

The third classification criterion is the shape of the orbit in the $r - z$-diagram itself, where r is the distance of the star to the GC projected onto the Galactic plane $r = \sqrt{x^2 + y^2}$. Figure

---

[11]$J_z - e$-diagrams from Pauli et al. (2006) have switched signs for J_z. However, using mathematical conventions consistently, stars on prograde orbits should have negative angular momentum
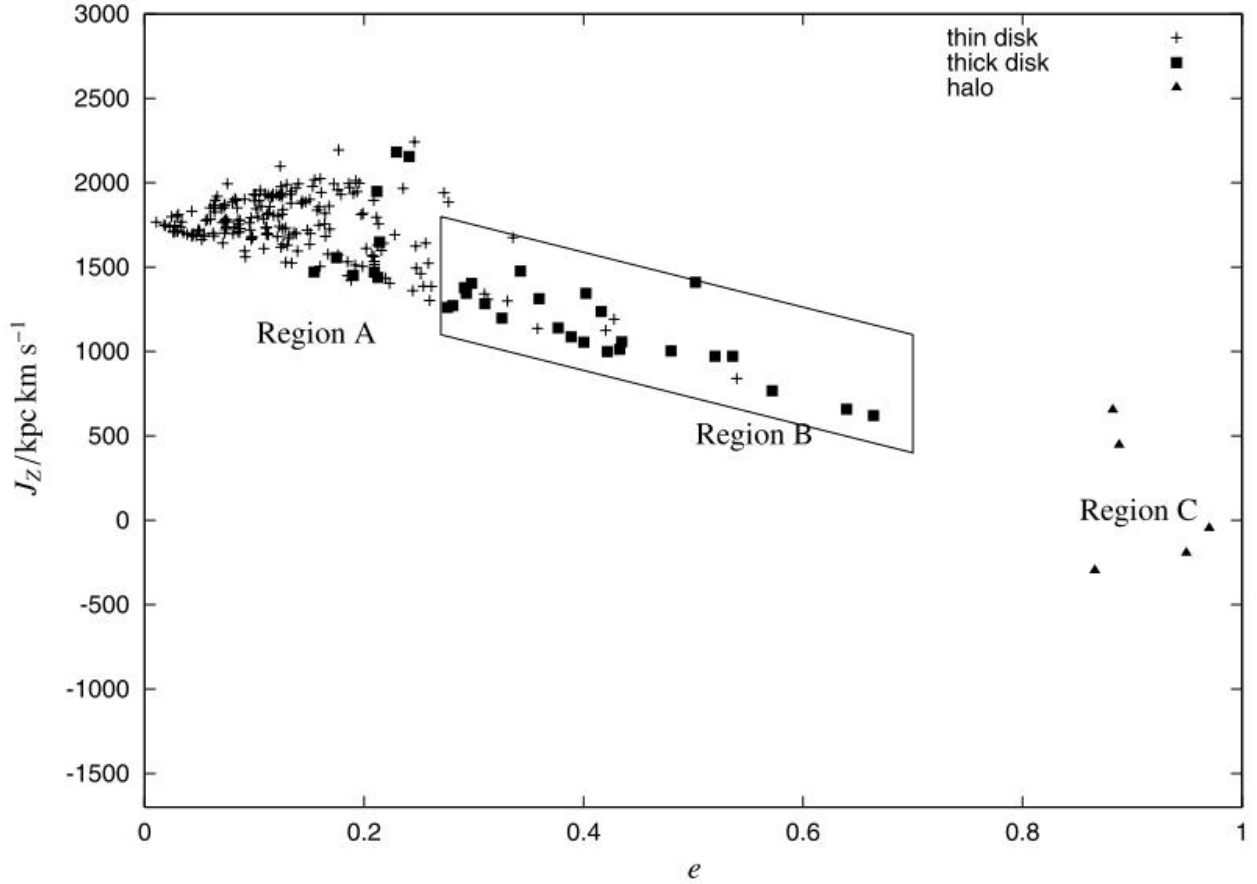
Figure 3.6: $J_z - e$-diagram for the calibration sample from Pauli et al. (2006)

3.7 shows some examples from Martin et al. (2017). The two plots in the top left are typical thin disk orbits, the two plots in the bottom right probable halo orbits. The remaining four plots show the transition from thin disk to halo orbits which are probably thick disk orbits. Thin-disk orbits only cover a very narrow region in this diagram and show 'boxy type' orbits because the stars are on very low-eccentricity orbits with very low inclination. They vary in r by less than 3 kpc and in z by less than 1-2 kpc. Thick-disk stars show a larger spread in both variables. Halo objects can have any chaotic orbit imaginable and may extend very far out, further out than what is generally considered to be the limit of the Galaxy.

The fourth classification criterion is the shape of the orbit projected onto the $x-y$-plane. Figure 3.8 shows some examples from Martin et al. (2017). The two plots in the top left are typical thin disk orbits, the two plots in the bottom right probable halo orbits. The remaining four plots show the transition from thin disk to halo orbits which are probably thick disk orbits. Again, thin disk orbits only cover a narrow ring as the stars are on very low-eccentricity orbits. The ring that is covered by thick-disk orbits is more expanded. The orbits may get close to the GC. Again, halo objects can have any chaotic orbit imaginable and may extend very far out, further out than what is generally considered to be the limit of the Galaxy.
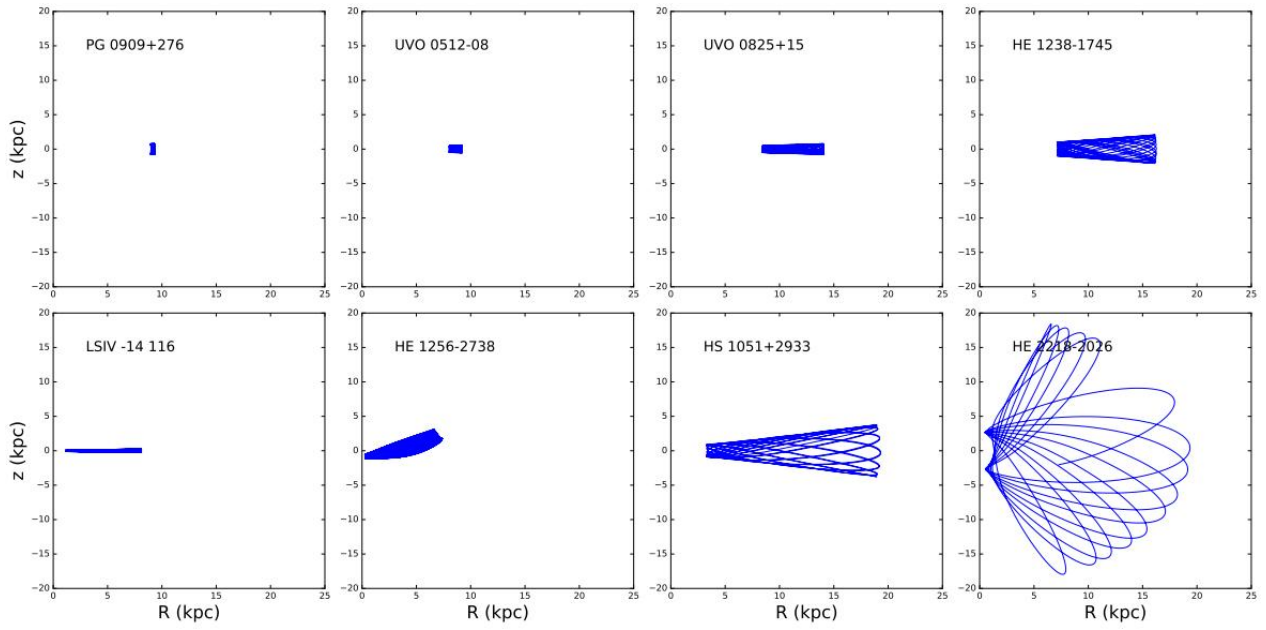
Figure 3.7: Typical orbits in the $r - z$-plane from Martin et al. (2017)
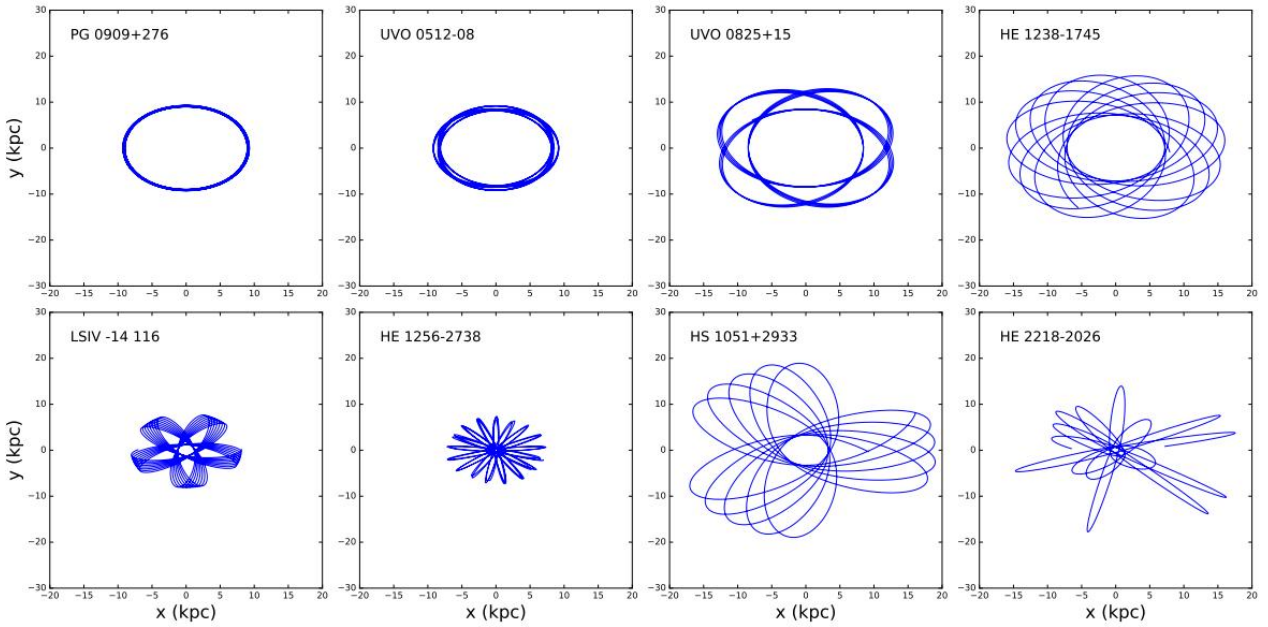
Figure 3.8: Typical orbits in the $x - y$-plane from Martin et al. (2017)

Chapter 4

Hypervelocity Stars

In the 1950s some main-sequence OB-stars have been found to move with astonishingly high velocities of $100 - 200$ km s^{-1} by Oort & Spitzer (1955) and were named runaway stars. But in 2005 the discovery of a new class of stars with even higher velocities attracted attention: HVSs are stars that move so fast that they may exceed the escape velocity of the Galaxy[12]. To solve the question of how these stars reach such velocities is an interplay of theoretical prediction and observational verification.

4.1 Acceleration mechanisms

4.1.1 Hills mechanism

Already in the late eighties, it was predicted from numerical experiments that a star can be ejected from the GC with velocities exceeding the escape velocity of the Galaxy by a three-body exchange collision of a stellar binary with a SMBH (Hills, 1988). In this tidal interaction the binary is disrupted when the gravitational tidal force of the SMBH exceeds the force that binds the binary. One star is kept bound to the SMBH and the other one is released (Fig. 4.1). It is well established that the GC hosts a SMBH with a mass of almost 4 million $M_\odot$ (Schödel et al., 2003; Ghez et al., 2005). This scenario also explains the existence of the so-called S-stars orbiting the SMBH in the GC (Gillessen et al., 2009). Interestingly, the nature, number, and distribution of the S-stars, which are normal main-sequence B-stars in the central arcsecond of the Galaxy on close eccentric orbits around the SMBH, are consistent with expectations for the former companions of HVS (Svensson et al., 2008; Madigan et al., 2014).

The binary fraction of massive O stars in the vicinity of the GC is comparable to that of dense stellar clusters (Ott et al., 1999; Pfuhl et al., 2014) (see Sec. 3). It was shown by Brown et al. (2007) that about 50% of the ejected stars that undergo this scenario remain bound to the Galaxy. While wide binaries are easier to disrupt than close binaries, their ejection velocity is much lower than that of their close counterparts.

---

[12]The escape velocity from the Galaxy has been determined from the Radial Velocity Experiment (RAVE) survey to be 544 km s^{-1}, though with substantial uncertainty, $498 - 608$ km s^{-1} at 90% confidence level (Smith et al., 2007)
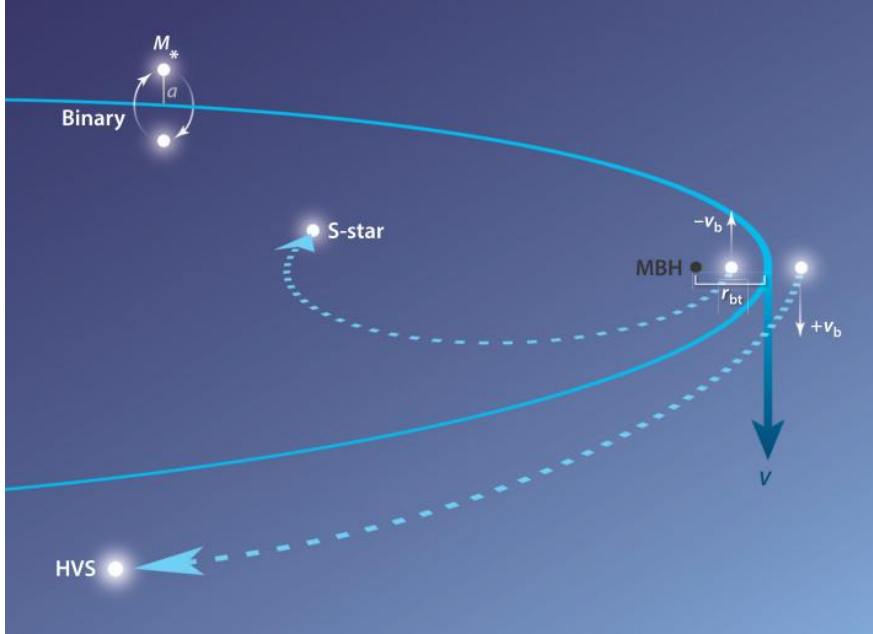
Figure 4.1: Schematic illustration of the Hills mechanism excerpted from Brown (2015). One star is kept bound to the SMBH and becomes one of the S-stars, while the other one is ejected.

Yu & Tremaine (2003) suggested the ejection of single stars by a massive binary black hole and calculated ejection rates to be of the order of $\sim 10^{-5}\,\mathrm{yr^{-1}}$ to $\sim 10^{-6}\,\mathrm{yr^{-1}}$ for the original scenario and an ejection rate of $\sim 10^{-4}\,\mathrm{yr^{-1}}$ for the massive binary black hole scenario. For an in-spiraling intermediate mass black hole similar ejection rates were achieved (Sesana et al., 2008; Gualandris & Merritt, 2009).

That a hierarchical triple system could be ejected through the interactions with the SMBH as a close hypervelocity binary was suggested by Perets (2009). Raghavan et al. (2010) showed that the fraction of triples among OB stars in the field is about 50%. Therefore, the disruption of a triple system by the SMBH is very likely although no such hypervelocity binary has been discovered yet. During their stellar evolution it is possible for such close binaries to reach mass transfer configurations and some can even merge. The outcome of these mass transfer configurations and mergers might explain e.g. fast hot subdwarf binaries and fast single hot subdwarfs (see formation of hot subdwarfs, Sec. 2.6). For stars that seem to be younger than their time of flight this triple disruption could explain their rejuvenation by their subsequently merging to a blue straggler (see Sec. 2.4) (Ginsburg & Perets, 2011).

4.1.2 Supernova acceleration

A star can be released from its massive binary companion if the latter explodes as a core-collapse supernova (see Sec. 2.5) (Blaauw, 1961). This scenario has been revisited for G/K dwarfs by Tauris (2015) to derive the maximum speed of HVS stars ejected from binaries. The simulations indicate that Galactic rest-frame velocities of up to 1280 kms^{-1} are possible.

The ejection velocity scales with the progenitor binary separation and is the sum of orbital velocity and the supernova kick velocity. Przybilla et al. (2008a) could show that for a binary containing of an early B and a Wolf-Rayet star it is possible to reach velocities up to $400 \, km \, s^{-1}$. To reach higher velocities the ejection has to take place in the direction of the Galactic rotation.

Also a thermonuclear SN Ia can release a companion star with high velocity. In an ultracompact binary like CD–30° 11223, where a WD orbits a hot subdwarf (Geier et al., 2013), the stars' separation will shrink with time due to the emission of gravitational waves. When the subdwarf fills its Roche lobe, mass transfer will start, and helium-rich material is transferred to the companion which can trigger the explosion of the WD (see Sec 2.5). The radial velocity semiamplitude in this stage is predicted to be about $600 \, km \, s^{-1}$.

The acceleration by this scenario leaves imprints on the ejected remnant. Hot subdwarfs in compact binaries have been spun up by the tidal influence of the close companion to projected rotational velocities that are substantially higher than the projected rotational velocities of single hot subdwarfs. Due to the pollution by supernova (SN) material and the subsequent stellar evolution, the surface abundances might be substantially affected and enriched with iron-group elements, at least for stars with non-convective envelopes. For cool stars with convective atmospheres the pollution will vanish quickly.

4.1.3   Dynamical interactions

Stars can also be ejected from stellar clusters by the dynamical N-body interaction (Poveda et al., 1967). Very high velocities are unlikely because the interaction probability of two binaries with really small separations like $\sim R_\odot$ even in a very dense cluster is expected to be extremely small and binary-binary interactions frequently result in merger events instead of an ejection (Fregeau et al., 2004). Anyhow, it is possible that a $4 \, M_\odot$ star can reach ejection velocities of $500 - 600 \, km \, s^{-1}$ when it interacts with a binary containing $100 \, M_\odot$ stars (Gvaramadze et al., 2009; Gvaramadze & Gualandris, 2011). To reach higher velocities, again, the ejection has to take place in the direction of the Galactic rotation.

4.1.4   Extragalactic origin

The escape velocities from nearby, low-mass galaxies are smaller and it is easier for stars to escape and travel through the intracluster space and some of the Galaxy's satellite galaxies have quite high velocities with respect to our own Galaxy. The dwarf galaxies themselfes are interacting with the Milky Way. Abadi et al. (2009) carried out numerical simulations of the disruption of dwarf galaxies and showed how they contribute halo stars with velocities as high as the escape velocity of the whole system.

The bigger galaxies in the Local Group might host a massive black hole on their own, e.g. Andromeda (Bender et al., 2005), LMC (Boubert & Evans, 2016), which can accelerate stars via the Hills mechanism and subsequently can be caught up by the Milky Way.
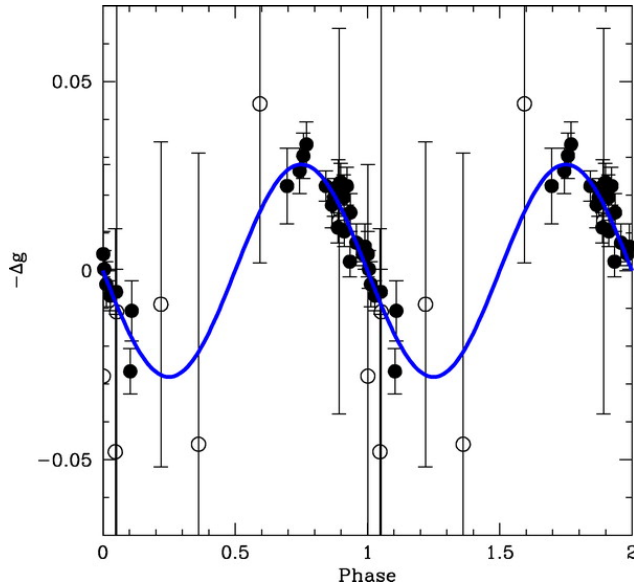
Figure 4.2: Pulsational light variations the B9 HVS 1 (period P = 0.355188 days, Fuentes et al. 2006) based on MMT g-band photometry.

4.2 Zoo of fast stars

The first HVS was discovered serendipitously in a radial velocity survey of faint BHB stars in 2005 by the Harvard group (Brown et al., 2005). In its spectral range exists a degeneracy which makes it difficult to distinguish between two different evolutionary states of the stars. Either they are distant (intrinsically bright) massive ($3 - 4\ M_\odot$) main sequence (MS) stars or closer (intrinsically faint) blue horizontal branch stars (BHB) of about $0.6\ M_\odot$. This degeneracy occurs from the coincidence that the main sequence and horizontal branch overlap in the HRD at the temperature of late B type stars of about 10000 K. Behr (2003) shows that B-type horizontal-branch stars are very slow rotators (< 8 km s^{-1}) and show peculiar metal abundance patterns probably caused by diffusion processes. Therefore, BHB stars can be distinguished from massive stars with $v\sin(i)$ measurements in combination with chemical abundance analyses. It could be shown by Fuentes et al. (2006) that HVS1 is a $3\ M_\odot$ low-amplitude, slowly pulsating main sequence B star, since BHB stars do not appear to be variable (see Fig. 4.2).

HVS2 and 3 were discovered shortly after this by the Bamberg group (Hirsch et al., 2005; Edelmann et al., 2005). By now there are about two dozens of HVSs known, mostly found in a targeted HVS survey by Brown et al. (2014). All but one are main sequence stars of late B spectral type with $3-4\ M_\odot$. Therefore they have short lifetimes. As such stars are luminous their survey covered a large volume (out to 100 kpc from the GC). The evolutionary ages of most of these HVS candidates are in good agreement with the GC scenario. However, they would be in agreement with an origin from almost anywhere in the Galactic disk. Only HVS2 (from now on called US 708) is a He-sdO. Hirsch et al. (2005) suggested that it is the merger product of two He-core WDs. Justham et al. (2009) and Wang & Han (2009) proposed that

US 708 is the product of a SN Ia from a single-degenerate WD+helium star binary. If either of these scenarios is valid, the star can come from anywhere in the Galaxy, its past trajectory does not have to point to the GC.

In the early stages the stars were 'discovered' and 'classified' as HVS based on their radial velocity only. But proper motion measurements for SDSS J013655.91+242546.0, an A-type main sequence star, exclude an origin in the GC and challenge the SMBH paradigm (Tillich et al., 2009). This was the first time when a proper motion was measured in connection with a HVS. Together with the spectroscopic distance a full 6 dimensional phase space information could be obtained.

For HD 271791 also the combined analysis of radial velocity and proper motion could exclude an origin in the GC but still is significantly unbound. The star is located at a distance of 20 kpc with a moderate radial velocity (444 km s^{-1}) and has a mass of 11 $M_\odot$ (Heber et al., 2008). Several proper motion measurements are available. All of them are non-zero but inconsistent with each other. The resulting Galactic rest frame velocities differ from 530 km,s^{-1} for the ACT catalogue to up to 920 km s^{-1} for the original Hipparcos measurement (Heber et al., 2008). Przybilla et al. (2008a) were able to measure a subsolar iron abundance along with an enhancement of α-elements in the star's atmosphere which indicates the capture of nucleosynthesis products from a high energetic hypernova.

Another example is HIP 60350, whose kinematics point to a birthplace in the Galactic disk with Galactic restframe velocities exceeding the Galactic escape velocity. The star's abundance patterns also indicate the capture of nucleosynthesis products from a core collapse supernova (Irrgang et al., 2010).

HVS3, a 9 $M_\odot$ main-sequence star, seems to be the most problematic case: an origin in the GC would mean a travel time to its present position at a distance of 60 kpc away from the Sun in the Galactic halo of about 100 Myr. This is in contrast to its main sequence lifetime of only 25 Myr. As HVS3 is located much closer to the LMC than to the GC an origin in this galaxy was suggested by Edelmann et al. (2005) although this would require an ejection velocity of 1000 km s^{-1} and consequently an unseen massive black hole in the LMC (Gualandris & Portegies Zwart, 2007). However, HST proper motions argue for an origin in the GC, leading Brown et al. (2010) to favour the GC as place of origin. This implies that the progenitor was a triple and a binary was ejected that subsequently merged to form a blue straggler. But several arguments speak against this scenario. First, Przybilla et al. (2008b) were able to show that the abundance pattern of HVS3 is not consistent with that one observed for stars near the GC but found a high degree of consistency with that of the LMC. Secondly, the proper motions derived from HST data may suffer from non-optimal observing conditions, e.g. different space-craft orientation, combination of data taken before and after refurbishment mission and in particular the inconsistencies in the charge transfers inefficiency (CTI) correction. They assume a linear behavior of the CTI over the time which is apparently not the case (Massey, 2010). Additionally the 1σ error bars are obviously underestimated as only two individual proper motion measurements from the individual epoch-1 and epoch-2 HST images are located in this area. Brown et al. (2015) included a third epoch of HST data but the results are still inconclusive.

J1539 is a BHB with a very high negative radial velocity, i.e. it is approaching us. It is travelling with a Galactic restframe velocity of about 690 km s^{-1}. In order to keep the star

bound a halo mass of more than $1.7 \cdot 10^{12} \, M_\odot$, is required (Przybilla et al., 2010). An origin as an unbound HVS from another galaxy is unlikely as the local volume is devoid of galaxies in a wide range around the infall direction of the star. To keep this star bound is one of the most important constraints for the construction of the Milky Way mass models of Irrgang et al. (2013).

Low-mass stars can be accelerated more easily and may gain higher ejection velocities (Tauris, 2015). Since they are long-lived they can travel very large distances during their main-sequence lifetime. However, they are less luminous than the B-type HVSs and can only be detected in a smaller volume by flux-limited surveys (<10 kpc), such as Sloan Extension for Galactic Understanding and Exploration (SEGUE). Moreover, a photometric pre-selection of low mass main-sequence stars is very difficult because of the overwhelmingly large number of red stars in the halo. Therefore attempts have been made to isolate HVS candidates of low mass from the SEGUE G and K Dwarf Sample (Palladino et al., 2014), LAMOST (Zhong et al., 2014) and RAVE (Hawkins et al., 2015) surveys using proper motion criteria or radial velocity criteria for the latter.

Palladino et al. (2014) selected high proper motion stars for a detailed analysis of the 6D phase space information, and 20 candidates were found to be probably unbound, four of which at 3σ and six at 2σ significance levels. From calculating the stellar trajectories in the Galactic potential, P14 derived possible places of origin in the Galactic disk. Of the seven stars with the highest probability of being unbound ($> 98\%$), none crossed the disk near the GC, but at distances of 5 to 10 kpc away from it. Hence, an origin in the GC was excluded for these stars, which challenges the SMBH slingshot mechanism. Other ejection mechanisms were discussed, including the classical scenario for dynamical interaction in star clusters and the binary supernova scenario. Such high velocities that can be reached by the latter can explain many, if not all, of the G/K-dwarf HVSs in the SEGUE sample.

Chapter 5

Analysis of main-sequence stars at high velocities

Up to now, all known HVSs are of early spectral type because such stars are very luminous and can be found to large distances. On the other hand, low-mass stars similar to the Sun are easier to accelerate and may reach higher ejection velocities (Tauris, 2015). Furthermore, they can travel very large distances during their main-sequence lifetime since they are long-lived. However, the luminosity of solar-like stars is considerably lower than that of late B-type main-sequence stars. Therefore, in fluxlimited surveys the accessible space volume is about 1000 times smaller for solar-like stars than for $3 - 4\,M_\odot$ stars. It, therefore, came much to our surprise, when Palladino et al. (2014) announced the discovery of no less than 20 HVS candidates of spectral type G and K. Moreover, such a large number is in contradiction to predictions of population synthesis studies (Kenyon et al., 2014).

5.1   Cool G and K type stars

The results of this chapter has already been published (Ziegerer et al., 2015) and the text is based on this publication with some updates based on data from new astrometric catalogues.

Palladino et al. (2014) (hereafter P14) carried out a search for G and K candidate-HVS from the SEGUE sample. High proper motion stars were selected for a detailed analysis of the 6D phase space information, and 20 candidates were found to be probably unbound, four of which at 3σ and six at 2σ significance levels. Only two stars had probabilities of less than 1σ to be unbound. From calculating the stellar trajectories in the Galactic potential, P14 derived possible places of origin in the Galactic disk. Of the seven stars with the highest probability of being unbound ($> 98\%$), none crossed the disk near the GC, but at distances of 5 to 10 kpc away from it. Hence, an origin in the GC was excluded for these stars, which challenges the SMBH slingshot mechanism. Other ejection mechanisms were discussed, including the classical scenarii for dynamical interaction in star clusters and the binary supernova scenario (Blaauw, 1961). The latter has been revisited by Tauris (2015) to derive the maximum speed of HVS stars ejected from binaries. The simulations indicate that Galactic rest-frame velocities of up to 1280 km s^{-1} are possible. Such high velocities can explain many, if not all, of the G/K-dwarf HVSs in the SEGUE sample.

As stressed by P14, the HVS nature of the stars strongly depends on the proper motion adopted. Therefore, the data were carefully checked for reliability by applying the same criteria adopted by Kilic et al. (2006) and visual inspection to exclude any potential blending issues. Three stars (stars $1 - 3$ of the P14 numbering) met all criteria and therefore were characterized as "clean" which means a chance of contamination of less than 0.5%. The remaining 17 stars were regarded as "reliable" with a chance of contamination of less than 1.5%. P14 state they expect false-positive HVS detections in their sample as P14 found that the candidates' tangential velocities are much higher than their radial velocities, unlike what is expected for an isotropic distribution of stars. The authors therefore cautioned that the high ratio of tangential vs. radial velocity may be characteristic for a sample with large proper motion errors and built a Monte Carlo test to estimate the probability of the stars being outliers. All stars show a likelihood of lower than 25%, half of them even lower than 10%. Nevertheless, an independent determination of the proper motions is required.

In this work we attempt to reanalyse the sample of P14 by determining proper motions for all 20 stars of the sample by combining all astrometric information at hand from digitized plates and modern surveys (Volkert, 2014; Ziegerer et al., 2015). We were able to derive proper motions for 14 stars of the sample. Because of the strong implications of the results of P14, we also determined their radial velocities and distances and calculated their trajectories in different Galactic potentials. Proper motion values of different catalogues were also taken into account. The confirmation of the candidates as HVSs as well as their place of origin would demand ejection mechanisms other than the SMBH slingshot to explain their existence.

5.2 Observations

5.2.1 Radial velocities and distances

We retrieved spectra of all 20 stars from the Sloan Digital Sky Survey (SDSS) data base as well as individual SDSS spectra to search for radial velocity variability so that close binaries could be excluded. No statistically significant radial velocity variations were detected, that is, we found no indication for binarity. The averaged radial velocities were consistent with those given by P14 to within mutual error limits.

P14 made use of the DR9 SEGUE Stellar Parameter Pipeline (SSPP), which provided estimates for effective temperatures T_{eff}, surface gravity $\log g$, iron abundance [Fe/H], and α enrichment factor [α/Fe]. They determined the distances of the stars using an isochrone-matching technique. We checked effective temperatures and surface gravities for consistency by comparing *ugriz*-magnitudes from SDSS to synthetic colours from Castelli (1999). Additionally, we compared the synthetic spectra of Munari et al. (2005) to the SDSS spectra (for a detailed description see Volkert, 2014). No inconsistencies were found and therefore the atmospheric parameters and distances as given by P14 were adopted. Radial velocities and distances can be found in Table 5.1.

P14 No.	Name	d (kpc)	$v_{\rm rad}$ ($\rm km\,s^{-1}$)	$\mu_\alpha \cos\delta$ ($\rm mas\,yr^{-1}$)	μ_δ ($\rm mas\,yr^{-1}$)	catalogue
1	SDSS J060306.77+825829.1	3.70 ± 0.30	-76.0 ± 1.5	38.3 ± 2.6	-41.0 ± 2.6	SDSS (P14)
2	SDSS J023433.42+262327.5	5.68 ± 0.45	-25.6 ± 5.0	8.9 ± 4.7	8.6 ± 3.7	this work
				-2.6 ± 3.0	15.5 ± 3.0	SDSS (P14)
3	SDSS J160620.65+042451.5	4.06 ± 0.73	31.7 ± 4.8	5.5 ± 4.0	-10.4 ± 4.7	this work
				23.6 ± 3.0	-1.6 ± 3.0	SDSS (P14)
4	SDSS J113102.87+665751.1	1.04 ± 0.19	-54.9 ± 0.9	-12.9 ± 2.4	-20.0 ± 4.1	this work
				-117.2 ± 5.9	206.8 ± 5.9	SDSS (P14)
5	SDSS J185018.09+191236.1	3.19 ± 0.26	58.0 ± 5.0	-0.5 ± 3.1	61.5 ± 3.1	SDSS (P14)
6	SDSS J035429.27-061354.1	3.13 ± 0.56	80.2 ± 3.3	5.8 ± 2.2	-4.5 ± 2.5	this work
				-41.6 ± 5.5	20.1 ± 5.5	SDSS (P14)
7	SDSS J064337.13+291410.0	3.06 ± 0.55	20.4 ± 2.8	-23.6 ± 2.6	29.9 ± 2.6	SDSS (P14)
8	SDSS J202446.41+121813.4	2.48 ± 0.45	6.3 ± 4.6	-18.9 ± 2.9	48.3 ± 2.9	SDSS (P14)
9	SDSS J011933.45+384913.0	3.31 ± 0.60	-36.9 ± 2.5	-3.1 ± 3.1	-8.5 ± 3.2	this work
				4.8 ± 2.9	-65.3 ± 2.9	SDSS (P14)
10	SDSS J172630.60+075544.0	3.82 ± 0.69	-2.2 ± 2.9	19.7 ± 2.9	-56.4 ± 2.9	SDSS (P14)
11	SDSS J073542.35+164941.4	3.70 ± 0.30	78.2 ± 2.7	7.6 ± 2.8	27.7 ± 2.8	SDSS (P14)
12	SDSS J025450.18+333158.4	3.14 ± 0.57	-62.4 ± 2.9	7.3 ± 2.6	21.4 ± 2.9	this work
				19.4 ± 2.8	38.1 ± 2.8	SDSS (P14)
13	SDSS J134427.80+282502.7	2.91 ± 0.52	2.5 ± 1.8	-2.0 ± 2.5	-5.6 ± 2.7	this work
				39.6 ± 3.0	-19.1 ± 3.0	SDSS (P14)
14	SDSS J225912.13+074356.5	4.60 ± 0.83	-97.8 ± 3.2	-0.9 ± 2.9	-1.3 ± 2.4	this work
				-5.7 ± 3.9	-44.5 ± 3.9	SDSS (P14)
15	SDSS J095816.39+005224.4	2.22 ± 0.40	1.6 ± 2.2	1.1 ± 2.2	-2.2 ± 2.3	this work
				-58.6 ± 5.4	8.1 ± 5.4	SDSS (P14)
16	SDSS J074728.84+185520.4	3.26 ± 0.26	43.9 ± 1.5	-5.2 ± 4.6	1.1 ± 5.1	this work
				0.8 ± 5.7	-58.1 ± 5.7	SDSS (P14)
17	SDSS J064257.02+371604.2	1.78 ± 0.14	6.2 ± 1.8	12.5 ± 3.2	13.0 ± 3.5	this work
				25.2 ± 2.5	42.1 ± 2.5	SDSS (P14)
18	SDSS J165956.02+392414.9	4.35 ± 0.78	-205.1 ± 5.0	1.8 ± 2.3	-28.6 ± 3.5	this work
				7.2 ± 3.1	-32.2 ± 3.1	SDSS (P14)
19	SDSS J110815.19-155210.3	4.56 ± 0.82	131.2 ± 4.1	-9.0 ± 2.0	-2.8 ± 1.7	this work
				-28.8 ± 6.9	8.7 ± 6.9	SDSS (P14)
20	SDSS J145132.12+003258.0	5.88 ± 1.06	87.9 ± 5.7	-0.4 ± 2.4	-1.0 ± 3.1	this work
				15.4 ± 5.8	-5.8 ± 5.8	SDSS (P14)

Table 5.1: Kinematic input values of all stars of the P14 sample.
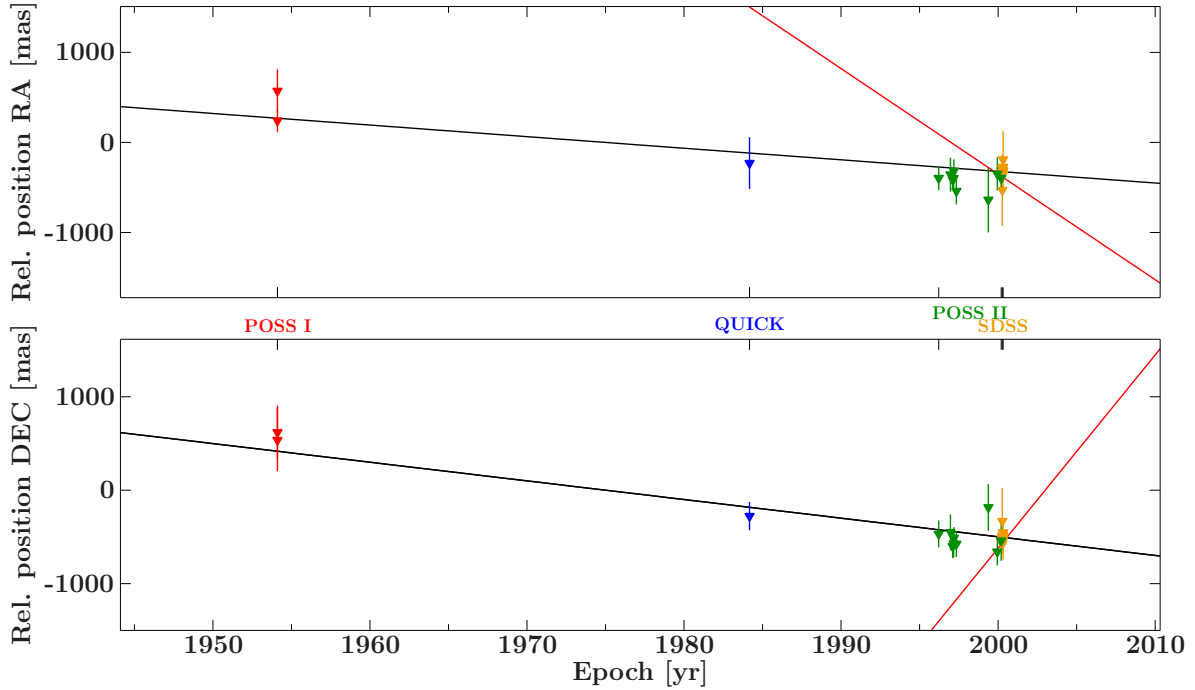
Figure 5.1: Proper motion fit through the relative positions of star 4. Red lines indicate the proper motion used by P14.

5.2.2 Proper motions

The most problematic information for the kinematic analysis are the proper motions. P14 selected their sample using proper motions provided by the SDSS data base.

We were able to derive proper motions for 14 of the 20 P14 candidates as explained in Chapter 3.3.1. For the low Galactic latitude stars #5, #7, #8, and #10 we failed to identify a sufficiently large set of suitable background galaxies. For stars 1 and 11 the fields are so crowded that the target could not be resolved on the old POSS I plates. These plates are the oldest and therefore the most important ones as they provide the long time baseline. Therefore we had to dismiss these six stars from further analysis of proper motion. For the remaining candidates, 16 to 29 background galaxies per field were found to be suitable and distributed favourably around the target. The proper motion components were obtained from the positions of all epochs by linear regression. Figure 5.1 shows such a proper motion fit for star #4. The slope of the corresponding SDSS proper motion is also indicated and this star shows the most extreme discrepancy between the SDSS and our proper motion.

Multiplying the stars' proper motions with their distances results in their tangential velocities v_t which are plotted in Figure 5.2 vs. the radial velocities and compared to the results of P14. Except for stars #2 and #18, the values derived here are significantly lower than those given by P14. With our results star #18 actually shows the highest tangential and highest radial velocity. Remarkably, the brightest star of the sample, star #4, shows the largest difference between the tangential velocity derived here and that found by P14. The ratios of the tangential vs. radial velocity of the stars are much lower than previously found
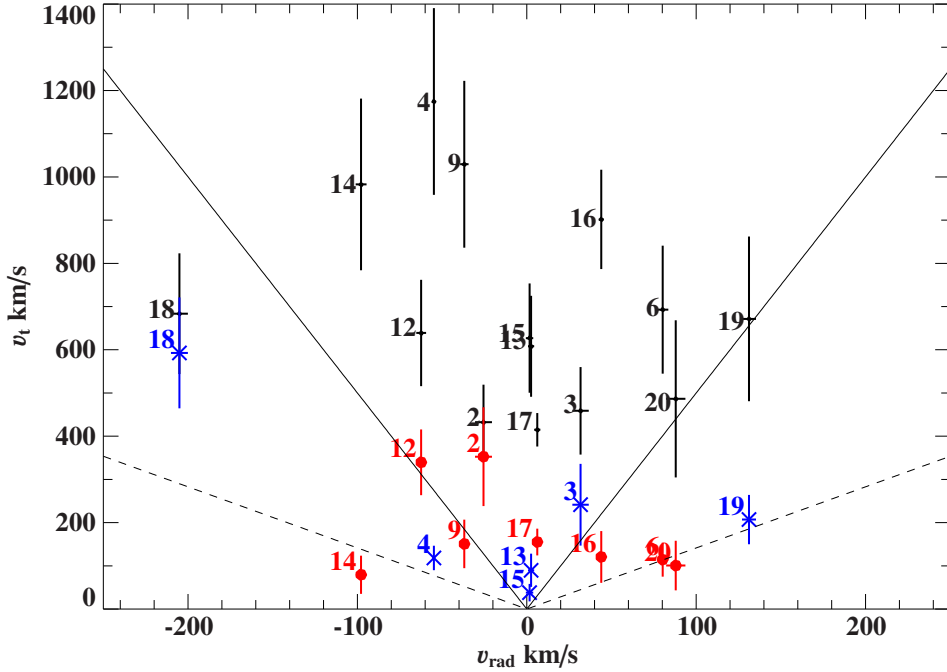
Figure 5.2: Comparison of the tangential and radial velocity derived in this work (coloured with error bars, red dots indicate stars with [Fe/H]> -0.7, blue crosses [Fe/H]< -0.7) and P14 (black). Error bars of P14 were derived in the same way as in this work. The dashed lines indicate $v_t = \sqrt{2}v_r$, while the solid lines indicate $v_t = 5v_r$.

(>5). According to P14, an isotropic distribution of stars would be described by a $\sqrt{2}$ times higher tangential than radial velocity. The new results come close to that expectation.

5.3   Kinematics

To obtain the dynamical properties of the stars, the orbits were traced back to the Galactic disk. Three different Milky Way mass models, see models I, II, and III in Irrgang et al. (2013) and Chapter 3.4.3, were used for this exercise to estimate possible systematic influences of the applied gravitational potential. Because the escape velocities of model II of Irrgang et al. (2013) are very similar to those calculated by P14, we first used this model for the comparison with the results of P14.

By varying the position and the velocity components within their respective errors by applying a Monte Carlo procedure with a depth of 10^6, we determined the intersection area of the trajectories with the Galactic plane. All input parameters for the procedure can be found in Table 5.1. From these simulations we also derived the median Galactic rest-frame velocities v_{GRF} at the present locations and their distributions. These values were compared with the respective local escape velocity. Because we assumed a lower tangential velocity than P14, the stars show a much lower probability of being bound to the Galaxy in all three applied gravitational potentials. The bound probability is defined as the number of orbits

P14 No.	r (kpc)	$r_{\min}$ (kpc)	$v_{\mathrm{GRF,1}}$ (km/s)	$v_{\mathrm{GRF,2}}$ (km/s)	bound probabilities (%)		
					P14 PM: SDSS	model II	this work
2	60.1	3.4	423.9 ± 100.7	635.2 ± 86.7	7.43	10.7	84.7
3	8.7	1.5	303.7 ± 75.9	645.9 ± 96.7	34.88	33.3	99.9
4	6.7	3.9	126.5 ± 23.2	1304.9 ± 213.5	0.00	0.0	100
6	6.8	0.8	145.4 ± 38.3	920.9 ± 148.2	0.07	0.3	100
9	11.1	7.5	254.1 ± 42.7	937.9 ± 187.3	1.20	1.9	100
12	27.7	16.2	482.4 ± 69.9	735.7 ± 117.4	3.77	5.5	81.1
13	7.6	3.6	185.7 ± 35.8	716.7 ± 110.0	4.42	8.9	100
14	7.4	1.0	200.2 ± 50.9	840.6 ± 194.6	5.86	7.4	100
15	11.2	7.1	239.5 ± 18.1	656.7 ± 117.5	15.98	21.7	100
16	19.3	2.4	293.3 ± 74.6	676.8 ± 113.2	19.70	12.0	99.9
17	10.3	9.8	346.8 ± 30.9	603.0 ± 37.3	20.01	10.9	100
18	3.6	0.5	537.4 ± 123.3	651.1 ± 134.8	21.30	29.8	63.6
19	3.6	0.9	150.2 ± 41.6	644.5 ± 188.0	23.69	34.6	100
20	7.8	1.9	255.7 ± 69.0	630.2 ± 178.2	43.24	43.2	100

Table 5.2: Kinematic properties of the program stars. The quantities r and $r_{\min}$ give the average and shortest distance to the GC at the 3σ level of the disk passage using new proper motions and model II of Irrgang et al. (2013). Galactic rest-frame velocities are based on our proper motions $v_{\mathrm{GRF,1}}$ or SDSS proper motions $v_{\mathrm{GRF,2}}$. The last three columns give the bound probabilities as listed by P14, our results based on model II, and the proper motions from SDSS and based on our revised proper motions.

not exceeding the local escape velocity with respect to the number of all calculated orbits. In Table 5.2 the bound probabilities listed by P14 are compared to the bound probabilities obtained by applying model II of Irrgang et al. (2013) using proper motions of SDSS, as used by P14, and of this work. The bound probabilities calculated using SDSS proper motions are similar to those obtained by P14, as expected. For the Galactic potential models I (see Table 5.3) and III (see Table 5.4), the differences between P14 and our calculations using SDSS proper motions can be explained by the higher Galaxy masses of those models.

Using our revised proper motions, none of the 14 candidates is unbound, irrespective of the Galactic potential model used. In fact, the probability to be unbound is lower than 0.1% for all but three candidates. Star #18 has the highest probability of being unbound, but even in the lightest Galaxy model II, this probability does not exceed 36%. We also calculated the distances to the GC at the time of the disk passage and the shortest distances in all three potentials (Tables 5.2-5.4). They do not depend on the choice of the potential except for stars #12, #16, and particularly star #2 (the latter changes by almost a factor of 2), for which the location of disk crossing must be regarded as highly uncertain. The GC is excluded at 3σ level for all stars irrespective of the choice of potential. Among the program stars the present position of star #17 is closest to the Galactic plane and, hence, its disk-crossing location outside of the solar circle can be well constrained (see Figure 5.3).

P14 No.	r (kpc)	$r_{\min}$ (kpc)	$v_{\text{GRF},1}$ (km/s)	$v_{\text{GRF},2}$ (km/s)	bound probabilities (%)		
					P14 PM: SDSS	model I	this work
2	50.3	3.8	424.5 ± 100.5	636.4 ± 86.7	7.43	23.4	92.3
3	8.5	1.3	304.6 ± 75.8	647.2 ± 96.7	34.88	49.3	100
4	6.7	3.9	128.1 ± 23.2	1305.8 ± 213.4	0.00	0.0	100
6	6.8	0.9	146.7 ± 38.4	922.6 ± 147.9	0.07	0.8	100
9	11.1	7.5	255.4 ± 42.6	937.5 ± 187.1	1.20	3.3	100
12	24.2	16.0	483.5 ± 69.9	736.4 ± 117.4	3.77	11.0	91.7
13	7.6	3.6	187.2 ± 35.8	717.7 ± 109.8	4.42	16.9	100
14	7.4	1.0	201.5 ± 50.9	839.7 ± 194.4	5.86	11.3	100
15	11.1	7.1	241.1 ± 18.1	657.0 ± 117.3	15.98	33.8	100
16	18.6	2.5	294.5 ± 74.4	675.9 ± 113.3	19.70	22.2	100
17	10.3	9.8	348.2 ± 30.9	604.4 ± 37.3	20.01	44.4	100
18	3.5	0.5	537.1 ± 123.5	651.1 ± 134.9	21.30	41.4	74.6
19	3.7	1.0	150.7 ± 41.3	644.6 ± 187.9	23.69	43.4	100
20	7.9	2.0	257.0 ± 69.0	631.7 ± 178.0	43.24	52.0	100

Table 5.3: Same as Table 5.2 for model I of Irrgang et al. (2013).

P14 No.	r (kpc)	$r_{\min}$ (kpc)	$v_{\text{GRF},1}$ (km/s)	$v_{\text{GRF},2}$ (km/s)	bound probabilities		
					P14 PM: SDSS	model III	this work
2	34.1	4.0	423.3 ± 100.5	634.4 ± 86.7	7.43	94.4	99.9
3	7.9	1.1	303.2 ± 75.8	645.3 ± 96.9	34.88	96.3	100
4	6.7	3.9	126.5 ± 23.1	1304.1 ± 213.8	0.00	1.0	100
6	6.8	0.9	144.7 ± 38.4	920.5 ± 147.8	0.07	19.8	100
9	11.1	7.5	253.5 ± 42.7	937.8 ± 187.4	1.20	22.6	100
12	18.9	14.2	481.8 ± 69.9	735.1 ± 117.6	3.77	68.4	100
13	7.6	3.7	185.1 ± 35.8	716.6 ± 110.0	4.42	79.4	100
14	7.3	1.1	199.6 ± 51.0	841.0 ± 194.5	5.86	43.3	100
15	11.2	7.2	239.5 ± 18.1	656.5 ± 117.5	15.98	88.3	100
16	16.3	2.5	292.5 ± 74.5	677.7 ± 113.3	19.70	83.5	100
17	10.3	9.8	346.2 ± 30.9	602.5 ± 37.3	20.01	100.0	100
18	3.6	0.5	537.4 ± 123.3	651.1 ± 134.8	21.30	87.7	97.9
19	3.7	1.0	149.8 ± 41.7	644.1 ± 187.9	23.69	80.0	100
20	8.0	2.1	255.1 ± 68.8	630.2 ± 178.4	43.24	85.4	100

Table 5.4: Same as Table 5.2 for model III of Irrgang et al. (2013).
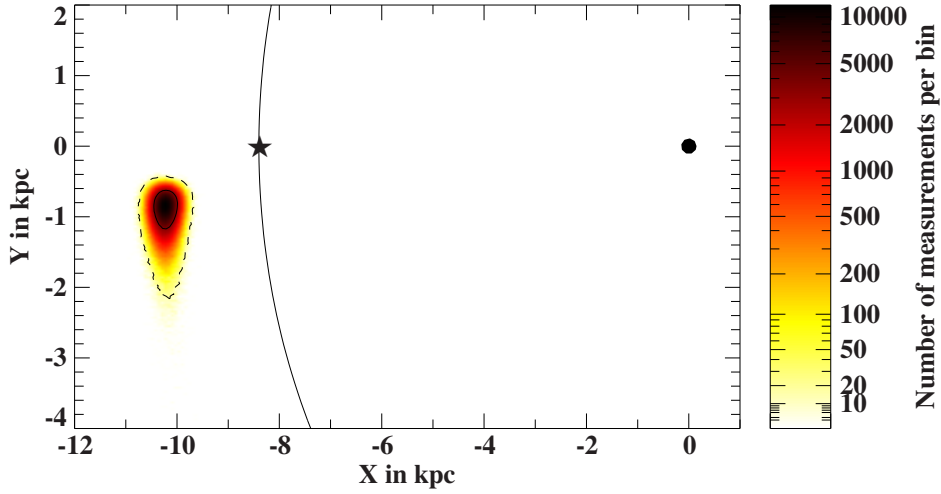
Figure 5.3: Disk passages (binned and colour coded) of star #17 obtained by a Monte Carlo simulation with 1 (solid) and 3 (dashed) σ contours. The solid line indicates the solar orbit. The asterisk marks the position of the Sun, the black dot that of the GC.

5.4   The stars in the catalogues

In addition, we searched for proper motions in other astrometric catalogues including the recently published catalogues APOP (Qi et al., 2015), HSOY (Altmann et al., 2017), and UCAC5 (Zacharias et al., 2017). All catalogue values can be found in Table 5.5. For most of the stars the catalogue proper motions of the depending catalogues (see Chapter 3.3.2) are consistent with each other, as expected. The newer catalogues are making use of previously existing catalogues. Even the newest catalogue, HSOY, which uses the *Gaia* DR1 position is affected by that. Only the more independent catalogue APOP shows significant different values for proper motions, which in most cases are consistent with our values. We have performed the same calculations as in the previous chapter for the whole P14 sample for all catalogue proper motions in all mass models as well.

P14 No.	$\mu_\alpha \cos \delta$ ($\mathrm{mas\,yr^{-1}}$)	μ_δ ($\mathrm{mas\,yr^{-1}}$)	catalogue	P14 No.	$\mu_\alpha \cos \delta$ ($\mathrm{mas\,yr^{-1}}$)	μ_δ ($\mathrm{mas\,yr^{-1}}$)	catalogue
1	38.3 ± 2.6	-41.0 ± 2.6	SDSS (P14)	11	7.6 ± 2.8	27.7 ± 2.8	SDSS (P14)
	36 ± 9	-36 ± 8	USNO		10 ± 11	18 ± 5	USNO
	39.9 ± 4.9	-38.0 ± 4.9	PPMXL		12.4 ± 5.2	8.5 ± 5.2	PPMXL
	35.7 ± 2.6	-37.2 ± 2.6	HSOY		5.0 ± 2.6	24.2 ± 2.6	HSOY
2	8.9 ± 4.7	8.6 ± 3.7	this work	12	7.3 ± 2.6	21.4 ± 2.9	this work
	-2.6 ± 3.0	15.5 ± 3.0	SDSS (P14)		19.4 ± 2.8	38.1 ± 2.8	SDSS (P14)
	1.1 ± 5.0	2.4 ± 5.0	PPMXL		6 ± 1	24 ± 8	USNO
	6.9 ± 6.1	7.4 ± 1.6	APOP		13.2 ± 5.1	24.1 ± 5.1	PPMXL
	1.5 ± 2.6	0.9 ± 2.4	HSOY		16.1 ± 2.4	28.1 ± 2.4	HSOY
3	5.5 ± 4.0	-10.4 ± 4.7	this work	13	-2.0 ± 2.5	-5.6 ± 2.7	this work
	23.6 ± 3.0	-1.6 ± 3.0	SDSS (P14)		39.6 ± 3.0	-19.1 ± 3.0	SDSS (P14)
	10.2 ± 5.3	-2.3 ± 5.3	PPMXL		38 ± 4	-10 ± 9	USNO
	6.7 ± 1.9	-7.4 ± 6.5	APOP		30.2 ± 4.8	-16.0 ± 4.8	PPMXL
	15.3 ± 2.4	-3.6 ± 2.5	HSOY		-12.2 ± 5.1	-2.3 ± 3.6	APOP
					26.2 ± 2.3	-20.0 ± 2.3	HSOY
4	-12.9 ± 2.4	-20.0 ± 4.1	this work	14	-0.9 ± 2.9	-1.3 ± 2.4	this work
	-117.2 ± 5.9	206.8 ± 5.9	SDSS (P14)		-5.7 ± 3.9	-44.5 ± 3.9	SDSS (P14)
	-122 ± 8	218 ± 14	USNO		-6 ± 8	-52 ± 18	USNO
	-126.5 ± 5.4	213.4 ± 5.4	PPMXL		-6.1 ± 6.9	-54.2 ± 6.9	PPMXL
	-17.5 ± 2.8	-19.5 ± 2.9	UCAC4		1.5 ± 1.9	2.1 ± 1.3	APOP
	-18.0 ± 1.4	-6.7 ± 0.8	APOP		-4.2 ± 3.2	-36.5 ± 3.4	HSOY
	-10.7 ± 5.3	-31.8 ± 5.3	UCAC5				
5	-0.5 ± 3.1	61.5 ± 3.1	SDSS (P14)	15	1.1 ± 2.2	-2.2 ± 2.3	this work
	-2 ± 2	70 ± 11	USNO		-58.6 ± 5.4	8.1 ± 5.4	SDSS (P14)
	-3.0 ± 5.1	66.1 ± 5.1	PPMXL		-58 ± 2	10 ± 2	USNO
					-63.5 ± 5.5	7.0 ± 5.5	PPMXL
					0.3 ± 2.1	-5.9 ± 0.9	APOP
6	5.8 ± 2.2	-4.5 ± 2.5	this work	16	-5.2 ± 4.6	1.1 ± 5.1	this work
	-41.6 ± 5.5	20.1 ± 5.5	SDSS (P14)		0.8 ± 5.7	-58.1 ± 5.7	SDSS (P14)
	-60 ± 8	32 ± 6	USNO		-2.9 ± 6.7	10.6 ± 6.7	PPMXL
	-54.4 ± 8.3	38.0 ± 8.3	PPMXL		-1.5 ± 2.7	1.3 ± 2.7	HSOY
	2.6 ± 3.0	-7.0 ± 2.4	APOP				
7	-23.6 ± 2.6	29.9 ± 2.6	SDSS (P14)	17	12.5 ± 3.2	13.0 ± 3.5	this work
	-22 ± 3	28 ± 6	USNO		25.2 ± 2.5	42.1 ± 2.5	SDSS (P14)
	-24.4 ± 5.4	27.7 ± 5.4	PPMXL		16 ± 5	36 ± 10	USNO
	-23.5 ± 2.4	24.7 ± 2.4	HSOY		21.4 ± 4.8	38.7 ± 4.8	PPMXL
					20.6 ± 2.4	31.4 ± 2.3	HSOY
8	-18.9 ± 2.9	48.3 ± 2.9	SDSS (P14)	18	1.8 ± 2.3	-28.6 ± 3.5	this work
	-16 ± 7	50 ± 7	USNO		7.2 ± 3.1	-32.2 ± 3.1	SDSS (P14)
	-12.3 ± 5.3	41.5 ± 5.3	PPMXL		10 ± 8	-24 ± 3	USNO
	-13.2 ± 2.5	33.4 ± 2.4	HSOY		8.0 ± 5.4	-25.6 ± 5.4	PPMXL

					11.4 ± 3.9	-31.1 ± 13.7	APOP
					4.4 ± 2.5	-28.3 ± 2.5	HSOY
9	-3.1 ± 3.1	-8.5 ± 3.2	this work	19	-9.0 ± 2.0	-2.8 ± 1.7	this work
	4.8 ± 2.9	-65.3 ± 2.9	SDSS (P14)		-28.8 ± 6.9	8.7 ± 6.9	SDSS (P14)
	8 ± 1	-58 ± 11	USNO		-30 ± 2	12 ± 13	USNO
	6.2 ± 5.1	-61.8 ± 5.1	PPMXL		-37.2 ± 9.7	2.2 ± 9.7	PPMXL
	2.9 ± 2.4	-56.9 ± 2.4	HSOY		-6.0 ± 7.6	0.5 ± 4.4	APOP
10	19.7 ± 2.9	-56.4 ± 2.9	SDSS (P14)	20	-0.4 ± 2.4	-1.0 ± 3.1	this work
	20 ± 6	-50 ± 3	USNO		15.4 ± 5.8	-5.8 ± 5.8	SDSS (P14)
	19.2 ± 5.1	-52.5 ± 5.1	PPMXL		32 ± 10	-8 ± 9	USNO
	15.0 ± 2.3	-48.6 ± 2.3	HSOY		25.1 ± 7.6	-6.1 ± 7.6	PPMXL
					20.9 ± 2.4	-15.7 ± 2.2	APOP
					11.1 ± 3.3	-3.9 ± 3.3	HSOY

Table 5.5: Catalogue values of proper motion of all stars of the P14 sample compared to our measurements.

5.4.1   APOP consistent with our work

For most of the stars with APOP proper motions, their values are in quite good agreement with our values. The overall behaviour is that the stars have the highest probability of being unbound with the proper motions of the catalogues depending on each other. Star #2 has kinematics like a disk star for HSOY and PPMXL, like a halo star for APOP and our proper motion (see Figure 5.4, Table A.2, and Chapter 3.5) and only shows high probability for being unbound for SDSS in combination with the lower mass models. The position of disk crossing is highly uncertain.

Star #3 shows a similiar behaviour with the difference that it seems to be a disk star for APOP and our proper motion (see Table A.3) while PPMXL proper motion leads to an intermediate kinematic between disk and halo star, while HSOY leads to halo kinematic (see Figures 5.5 and 5.6. In these figures the calculations for all three mass models is shown, the model independence is exemplarily shown). Only SDSS leads to the chance of being unbound.

Star #4 is the most extreme case (see Table A.4). Our proper motions are in good agreement with APOP, UCAC4, and UCAC5 and lead to the kinematic behaviour of a disk star. These values are totally discrepant to PPMXL, SDSS, and USNO-B1.0 which lead to a highly unbound orbit. There is no clear evidence for the cause of this discrepancy, especially as this star is the brightest of the whole sample. Stars #6, #13, #14, #15, and #19 behave similar to that star, just with smaller absolute values (see Tables A.6, A.13, A.14, A.15, and A.19).

Star #18 is the star with the highest probability of being unbound in the sample with our proper motions (see Table A.18). As the values are quite close to the catalogue values its kinematics are similar in all calculations. If not unbound, the star might be a halo star.
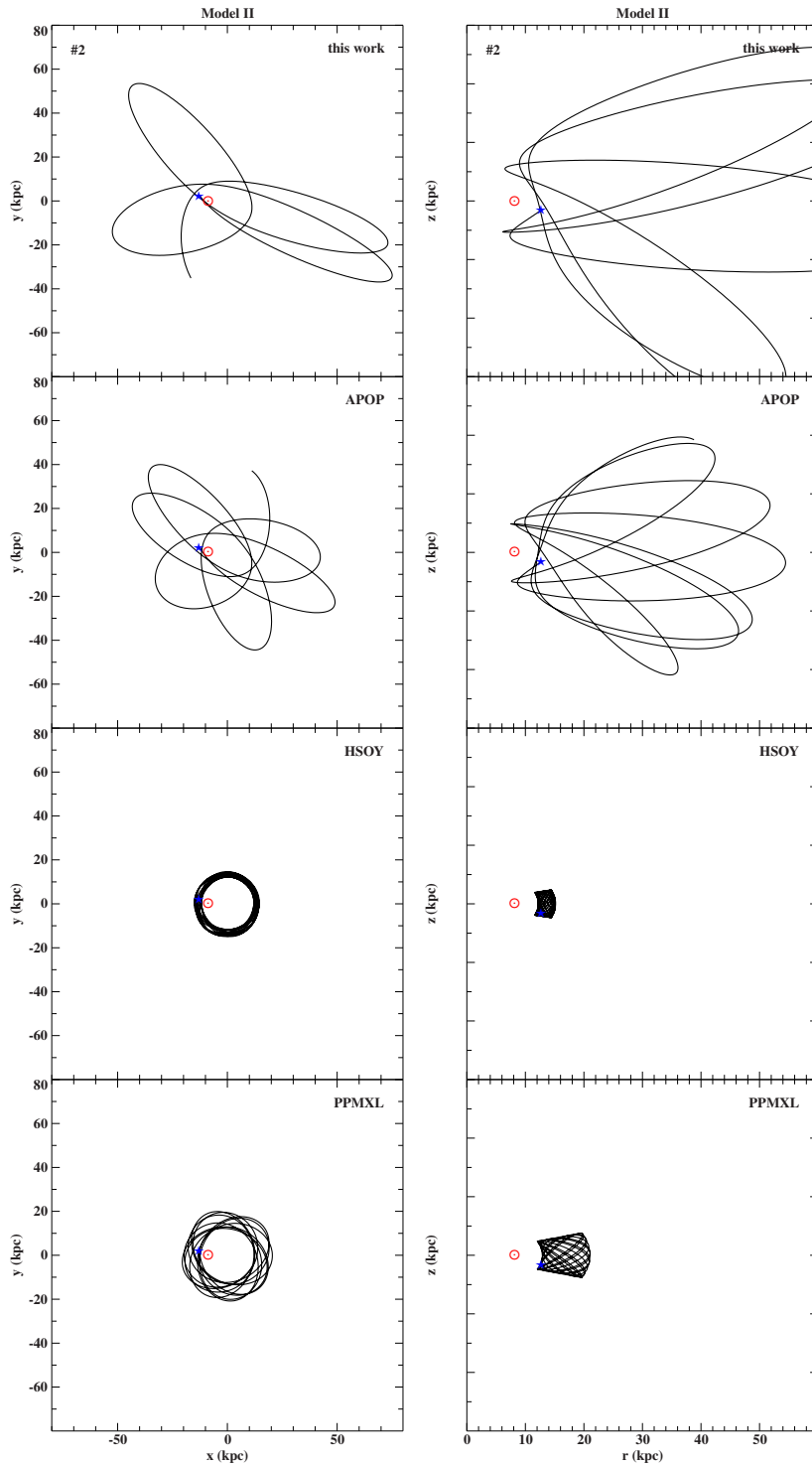
Figure 5.4: Galactic orbits for star #2 calculated for proper motions from this work (top panels) and from different astrometric catalogues (APOP, HSOY, and PPMXL). *Left panel:* $x - y$-diagram. *Right panel:* $r - z$-diagram. The red solar symbol indicates the position of the Sun, the blue star indicates the current position of star #2. The orbits have been calculated 5000 Myr into the past in model II of Irrgang et al. (2013).
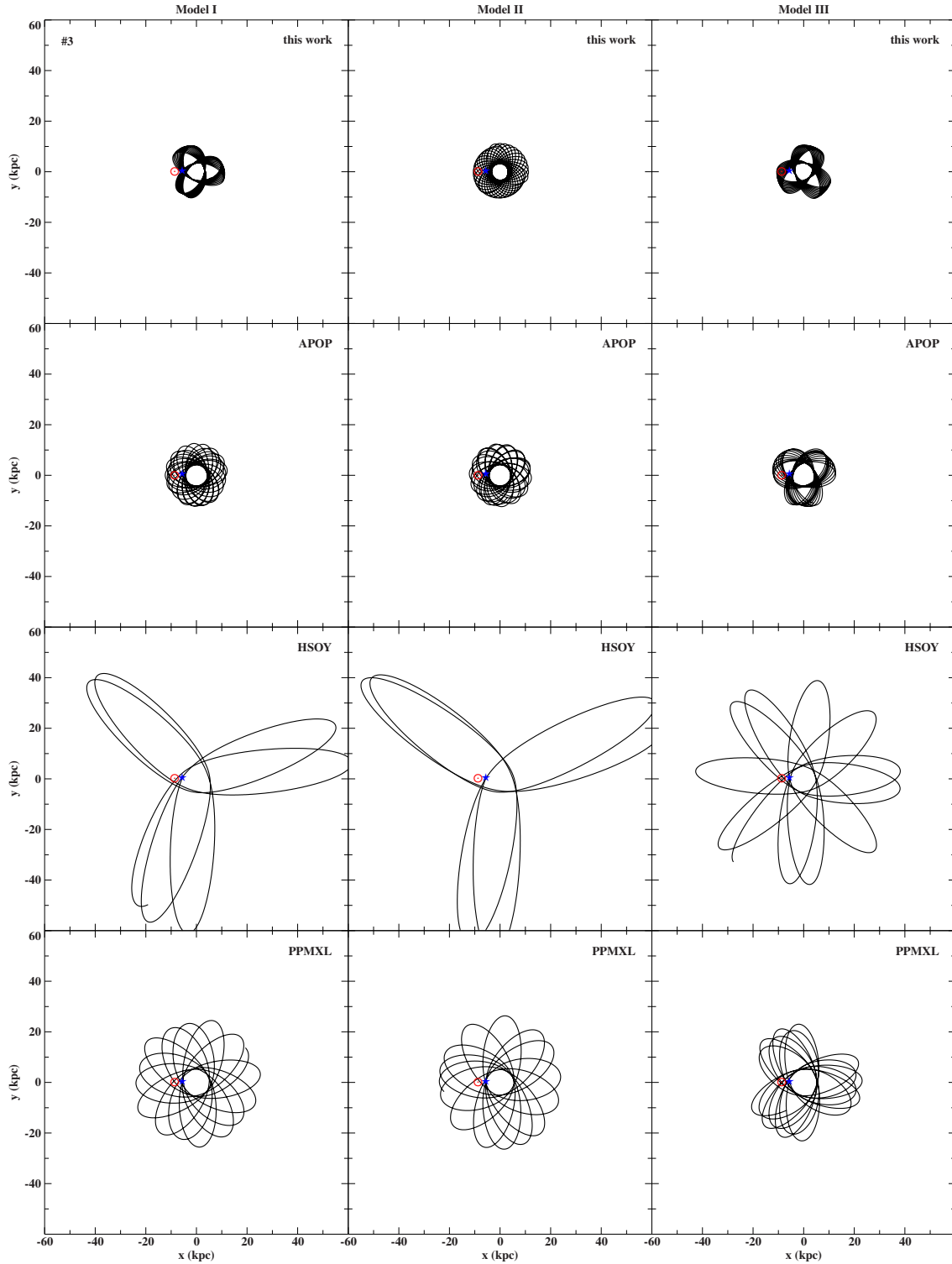
Figure 5.5: Galactic orbits for star #3 in the $x - y$-plane. The red solar symbol indicates the position of the Sun, the blue star indicates the current position of star #3. The orbits has been calculated 5000 Myr into the past in the three mass models of Irrgang et al. (2013), respectively (left to right panels) and proper motions from this work (top panels) and different astrometric catalogues (APOP, HSOY, and PPMXL).
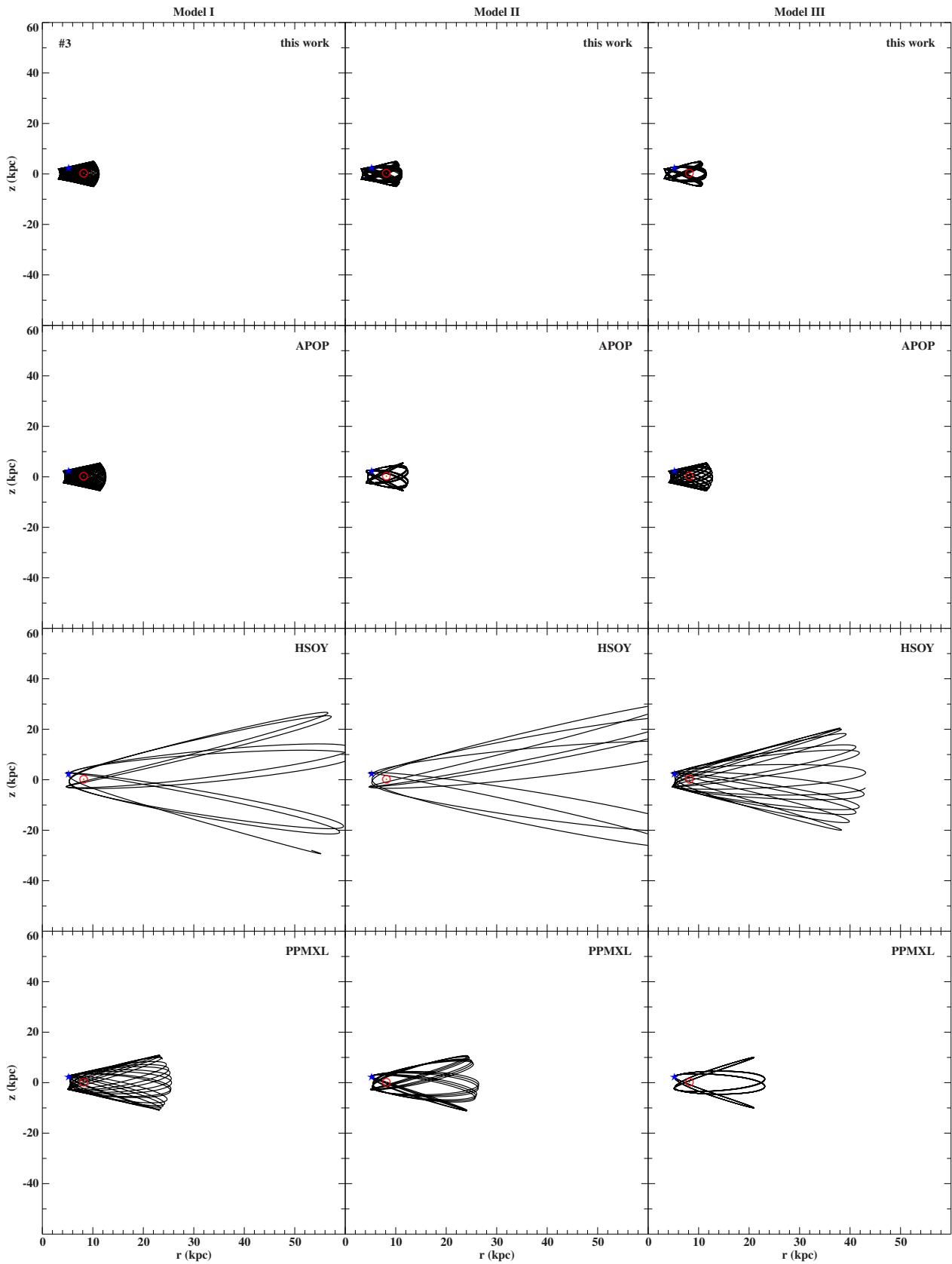
Figure 5.6: Same as Figure 5.5, but in the $r-z$-plane.

5.4.2   APOP inconsistent with our work

Unlike for the other stars, the APOP proper motions show extreme values for star #20. The star shows a behaviour very much dependent of the applied proper motion. While it is bound and behaves like a thick disk star for our values, it still remains bound for the HSOY values but behaving like a halo star. For the rest of the catalogue values it has a quite high probability of being unbound (see Table A.20).

5.4.3   Stars without own proper motion measurements

Because we were unable to measure proper motions for stars #1, #5, #7, #8, #10, and #11 we would have to rely on catalogue values. Unfortunately none of these stars are listed in the APOP catalogue. Only catalogues which depend on each other are available and therefore, all the proper motions are consistent within their uncertainties. Only star #11 shows an outlier in one component of PPMXL. For the given proper motions the bound probability of all stars is very low. An independent proper motion measurement is needed to confirm this. The kinematic properties for these stars can be found in Tables A.1 -A.11.

5.4.4   Stars with no APOP

Star #9 behaves like a disk star with our proper motion and is unbound with all the catalogue values (see Table A.9). Star #12 behaves most likely like a halo star with our proper motion. It also shows a similar behaviour for all the catalogue values with a slight increasement of unbound probability (see Table A.12).

Star #16 shows kinematics like a disk star for our proper motion and HSOY. For PPMXL it shows an extreme disk behaviour, meaning it stays in the Galactic plane but the highly eccentric orbit reaches the outskirts of the Galaxy. With SDSS proper motions it has a high probability of being unbound in the lower mass models (see Table A.16).

Star #17 behaves like a thick disk star for our proper motion, like a halo star for HSOY. For the rest of the catalogue values it acts either like a halo star or possibly unbound for the lower mass models (see Table A.17).

5.5   Runaway, disk, or halo stars?

Since all 14 candidates for which we were able to measure proper motions are bound and none comes from anywhere near the GC, these stars have to be dismissed as HVS stars. P14 discussed whether they might be disk runaways or genuine halo stars. In Figure 5.7 the Galactic radial velocity component v_r is plotted against the rotational velocity component v_ϕ and compared with contour lines denoting the limits for the thin and thick disk by Pauli et al. (2006). As all stars, except #2, #12, and, #18, lie within or close to these contours, we conclude that their kinematics belong to the thick disk, some maybe to the thin disk. However, kinematics cannot easily distinguish between thick disk and runaway origins. Because most runaways are launched at modest velocities from the rotating disk, their kinematic and spatial distributions will naturally look quite similar to those of the thick disk (Bromley
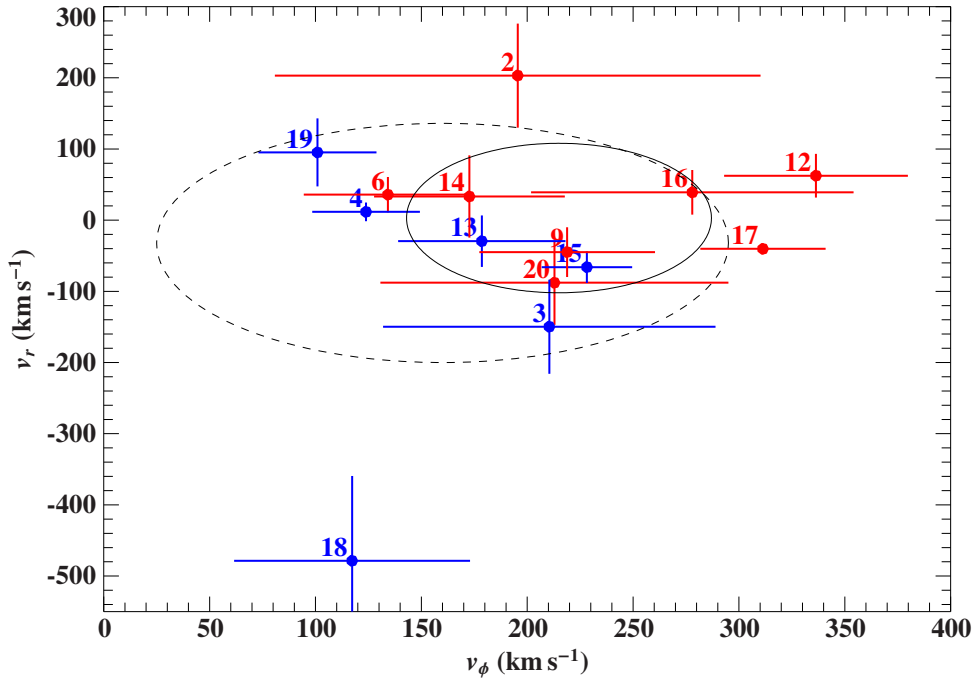
Figure 5.7: $v_r - v_\phi$-diagram, numbered dots with error bars: stars examined in this work (red indicates stars with [Fe/H]> -0.7, blue [Fe/H]< -0.7), dashed line: 3σ contour of the thick disk, solid line: 3σ contour of the thin disk.

et al., 2009). Population membership can also be assigned by chemical tagging, using [Fe/H] and [α/Fe] as indicators. According to Fuhrmann (2011), thin-disk stars have [Fe/H] $>$-0.5 and [α/Fe]$<$0.2, whereas thick-disk stars have [Fe/H] $<$-0.3 and [α/Fe]$>$0.2 (see Figure 15 of Fuhrmann, 2011). However, some halo stars may have similar chemical abundances as thick-disk stars. In Figure 5.8 we plot [α/Fe] vs. [Fe/H] for the 14 stars and conclude that most stars have chemical characterics of the thick disk, whereas stars #2, #16, and #17 are more likely to be thin-disk stars. The chemical composition of star #18 strengthens the conclusion that it is a halo star.

Dynamical ejection in dense star clusters or binary supernova ejection may result in disk runaway stars. Kenyon et al. (2014) simulated the Galactic populations of (i) HVS stars ejected from the GC via the SMBH slingshot mechanism, (ii) runaway stars from the disk ejected at distances of 3 to 30 kpc from the GC by either the binary supernova mechanism or dynamcial ejection from clusters. They compared their predictions to the observed properties of B-type HVS (Brown et al., 2014) and B-type runaway stars (Silva & Napiwotzki, 2011) as well as to the P14 sample of G- and K-type HVS candidates. Kenyon et al. (2014) concluded that the runaway sample of B-type stars can be matched by their simulation for binary supernova ejection or dynamical ejection, but not by the SMBH slingshot. The HVS sample of B-type stars (Brown et al., 2014), on the other hand, is well reproduced by the prediction from the SMBH slingshot, but the data cannot be explained by runaway models.

However, SMBH slingshot models fail to account for the observations of the P14 SEGUE HVS candidates of spectral type G and K. In Figure 5.9 we compare the radial velocities and
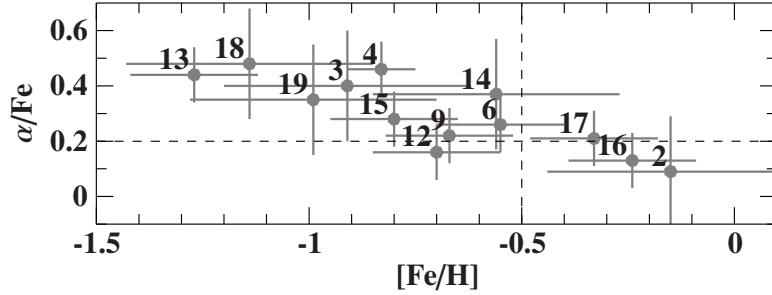
Figure 5.8: Position of the program stars in the ([Fe/H], [α/Fe]) diagram. The dashed lines separate thick-disk (top left) from thin-disk stars (bottom right). Error bars were estimated from the S/N ratio of the spectra using the prescriptions of Allende Prieto et al. (2008) and Lee et al. (2011).

our new proper motions of the 14 P14 stars analysed here to the predictions from simulations for 1 M$_\odot$ runaway stars generated by the binary supernova mechanism. The distribution of stars match the prediction of Kenyon et al. (2014) very well. However, the stellar chemical composition is inconsistent with the disk runaway scenario, except possibly for the three most metal-rich ones. Such stars could be ejected as the surviving donor of an exploding white dwarf in a SN Ia event, as is discussed for Tycho's supernova (Ruiz-Lapuente et al., 2004).

5.6 Conclusions

We presented a revised analysis of the 20 candidate HVSs introduced by P14. Our work was motivated by the warning of P14 that the proper motions they extracted from the SDSS data base were abnormally high and that therefore the stars have to be considered HVS candidates only until their proper motions are confirmed. Volkert (2014) cross-checked the proper motions used by P14 against astrometric catalogues available at that time and found them to be mutually consistent. Therefore, we independently determined proper motions from all astrometric images using grids of distant galaxies as frames of reference for 14 of these candidates. We repeated the analysis of P14 and confirmed the radial velocites, atmospheric parameters, and distances. However, except for two stars, all measured proper motions are significantly lower than those used by P14 or other astrometric catalogues. We carried out a kinematic analysis of the stars in three different Milky Way mass models and confirmed that no star originated from the GC. All stars are bound to the Galaxy and therefore have to be dismissed as HVS. We considered the possibilities that the stars are either old stars of the halo or thick-disk stars, as suggested by their metallicities and α element enhancements from the (U,V) diagram or disk-runaway stars. The stellar kinematics as well as their chemical composition indicate that they mostly belong to the thick-disk population. We speculate that the more metal rich ones could be runaway stars from the thin disk. Accordingly, star #18 might belong to the halo. However, the disk-runaway option would also be consistent with model predictions by Kenyon et al. (2014) for all stars (except for star #18). However, this is at variance with the stellar chemical composition except for the three most metal-rich
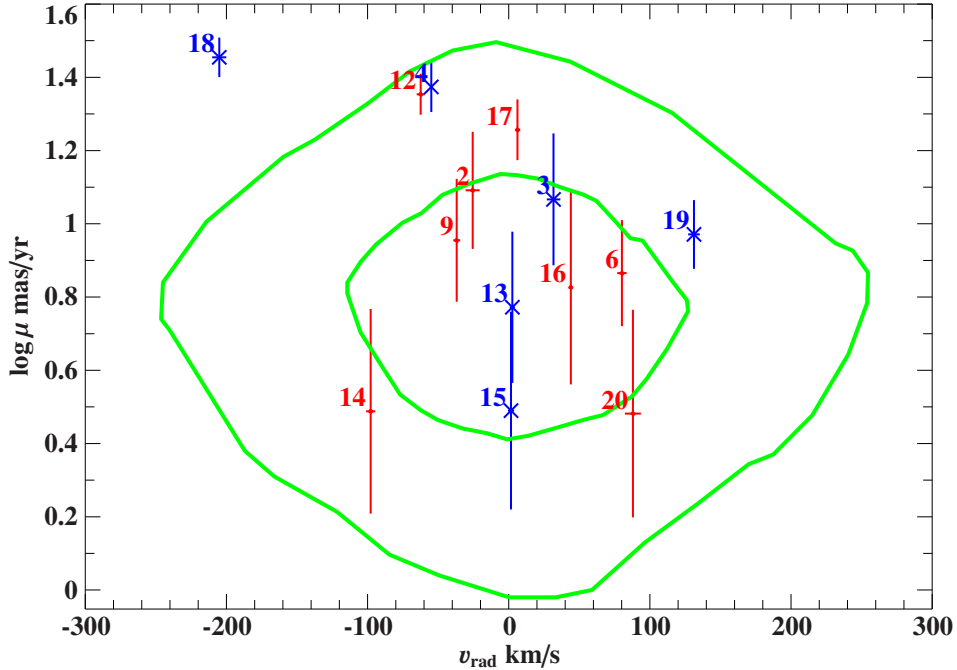
Figure 5.9: Comparison of the HVS candidates from P14 with proper motions derived by us (red indicates stars with [Fe/H]> -0.7, blue crosses [Fe/H]< -0.7) in the proper motion vs. radial velocity plane with predictions of simulations for a sample of 1 $M_\odot$ runaways (green curves) generated by the binary supernova mechanism (Kenyon et al., 2014). The inner contour includes 50% of the stars in the distance-limited sample, while the outer one includes 90% (adapted from Fig. 25 of Kenyon et al., 2014).

stars, which might be runaway stars from the thin-disk population.

Further we conclude that the uncertainty in the proper motion of SDSS has already been introduced earlier. As the catalogues depend on each others results the uncertainty was most likely already introduced in the first approach. Because new astrometric catalogues became available, we cross-checked them against our measured proper motions. The APOP catalogue, which is the most independent catalogue, gives proper motions consistent to the ones we measured for most of the stars. HSOY was a promising catalogue, as it includes the first data release of *Gaia*. Another catalogue which uses data from the first *Gaia* data release is UCAC5. Unfortunately, only one of the program stars is listed in this catalogue, star #4 but it shows good agreement with our proper measurement. But as it also is based on the PPMXL catalogue, the uncertainty also propagates into this catalogue. The second data release of *Gaia* is more promising as it will depend on *Gaia* positions only and will therefore be a completely independent proper motion measurement.

Chapter 6

Analysis of hot subdwarfs at high velocities

The HVS radial velocity survey of Brown et al. (2014) targeted late B-type stars of $3 - 4\,M_\odot$ and successfully discovered about two dozens such HVSs. However, HVSs were also found among hot subdwarf stars. By the time of the beginning of this work the only known unbound subluminous HVS was US 708, a He-sdO. It was discovered by Hirsch et al. (2005) as the second HVS.

We embarked on a systematic spectroscopic survey for HVSs among hot subluminous stars, the Hyper-Massive Unseen Companions to Hot Faint Underluminous Stars from SDSS (MUCHFUSS) project. The results reported in this chapter have already been published (Geier et al., 2015a; Németh et al., 2016; Ziegerer et al., 2017) and the text is based on these publications.

6.1 The Hyper-MUCHFUSS project

The MUCHFUSS project was originated to find hot subdwarf stars with massive compact companions such as white dwarfs with masses $M > 1.0\,M_\odot$, neutron stars or stellar black holes (Geier et al., 2015b). Hot subdwarf stars were selected from the SDSS by colour and visual inspection of the spectra. Hot subdwarf stars with high radial velocity variations were selected as candidates for follow-up spectroscopy to derive the radial velocity curves and the binary mass functions (Geier et al., 2011).

In the course of the MUCHFUSS project CD–30° 11223 was observed. It turned out that it is the most compact hot subdwarf binary discovered so far. It has the shortest known orbital period and highest radial velocity amplitude. A WD is orbited by a hot subdwarf with a period of $\simeq 0.049879$ d (Geier et al., 2013). The subdwarf will start to transfer material in less than 50 Myr as the separation is shrinking due to the emission of gravitational waves until the sdB fills its Roche lobe. According to its atmospheric parameters, the sdB has just started the core-burning phase, which typically lasts for about 100 Myrs. Therefore, helium-rich material is transferred to WD companion, which, according to its mass, mostly consists of carbon and oxygen. The ignition of He-burning at the surface may trigger carbon-burning in the core although the WD is less massive than the Chandrasekhar limit making

this binary a possible progenitor candidate for a SN Ia event. Just before the SN event, the orbital period of the system is predicted to have shrunk to only 0.019 d. At this period the orbital velocity of the sdB will be about 600 km s^{-1} which is close to the Galactic escape velocity. When the WD is disrupted, the sdB will be released. Kinematics show that the system is a member of the thin disc population. Therefore, it belongs to a young stellar population rather than to the old population of stars at high Galactic latitudes. Depending on the direction of ejection relative to the orbit of the system around the GC, the Galactic rest frame velocity could be even higher by up to 240 km s^{-1}. In this case the ejected sdB star would be unbound. It is predicted to be a fast rotator spun up by the tidal influence of its former close companion.

The extension of the MUCHFUSS project – the Hyper-MUCHFUSS project – had the aim to find potentially unbound hot subdwarfs with therefore high but constant radial velocity. In the first campaign of Tillich et al. (2011) twelve sdB stars have been found. These stars either belong to an old population in the Galactic halo or are ejected by i.e. the Hills mechanism or a supernova event and possibly unbound. For interesting candidates follow-up spectroscopic observations have been performed with various instruments.

6.2 US 708 - the fastest star known

US 708 has been classified as a helium-rich hot subdwarf and identified as the first known hot subdwarf O- or B-type HVS by Hirsch et al. (2005). Justham et al. (2009) and Wang & Han (2009) already proposed that US 708 might be the ejected He-donor after the WD companion exploded as SN Ia. The discovery of CD–30° 11223 as a possible progenitor system for such a star like US 708 by Geier et al. (2013) lead us to a more detailed reobservation of US 708. The following results have already been published in Geier et al. (2015a).

The resulting radial velocity turned out to be significantly higher (917 ± 7 km s^{-1}) than the one published by Hirsch et al. (2005) (709 ± 7 km s^{-1}). The proper motion has beed derived from multi-epoch position measurements of Schmidt plates and the SDSS as described in Chapter 3.3.1. Three POSS I, two QVN, four POSS II, and one SDSS epoch, split up in five bands, were available. Additionally, we were able to use data from Panoramic Survey Telescope and Rapid Response System (PanSTARRS), which lead to a timebase of 59 years and 29 additional epochs. For each of these epochs the measured positions were compared to the reference values from the PanSTARRS catalogue. Figure 6.1 shows the resulting proper motion fit.

With a spectroscopic distance of 8.5 ± 1.0 kpc the high radial velocity and proper motion lead to a Galactic rest-frame velocity of $v_{\mathrm{GRF}} = 1157 \pm 53$ km s^{-1} which makes it the fastest known unbound star in our Galaxy. Tracing back its trajectory and assuming no further deviations, we deduced that it crossed the Galactic disk 14.0 ± 3.1 Myr ago with an ejection velocity from the Galactic disk of $v_{\mathrm{ej}} = 998 \pm 68$ km s^{-1}. In order to obtain a high level of significance the Monte Carlo simulation was this time performed with a depth of 10^8. An origin in the GC can be excluded with a high confidence of more than 5σ. Figure 6.2 shows the area of the disk ejection. We also calculated the theoretical needed proper motion if US 708 was coming from the GC. This hypothetical proper motion is also indicated in Figure 6.1. Especially in declination it differs significantly from the measured value including a switch
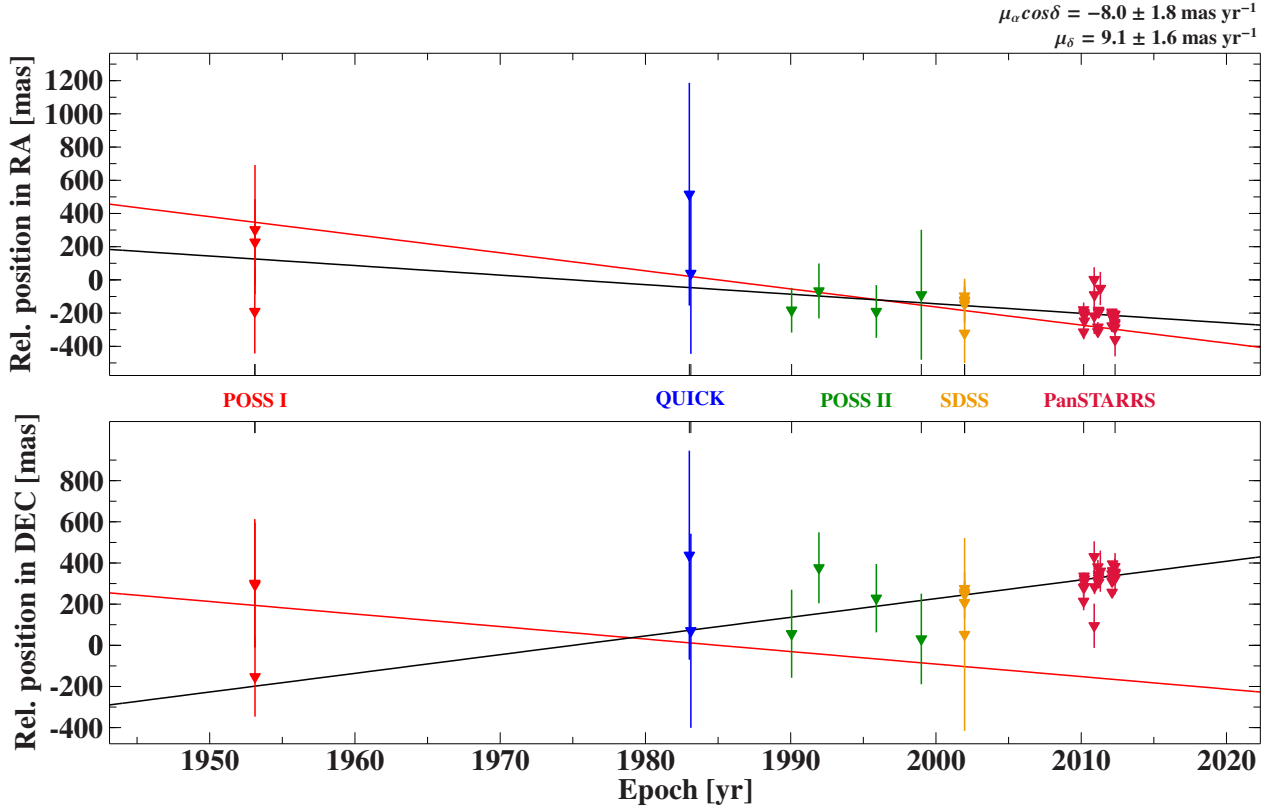
Figure 6.1:   Relative positions of US 708 in right ascension (upper panel) and declination (lower panel). The black lines show the best fit from linear regression. The red lines show the theoretical proper motion components required for the star to originate from the GC (Geier et al., 2015a).

of the sign.

To reach such a high ejection velocity, US 708 is supposed stem from a ultra compact binary where the companion is exploded in a SN Ia event. The WD companion must have been rather massive. The likely progenitor system consists of a compact helium star with a mass of $\sim 0.3\,M_\odot$ and a massive carbon-oxygen WD (1.0 to $1.2\,M_\odot$) with an orbital period of ~ 10 min. The ejection velocity of the He-star equals the radial velocity semiamplitude of the progenitor binary at the moment of the SN explosion ($K = 998 \pm 68$ km s^{-1}) modified by the additional perpendicular velocity component the star received through the SN explosion (~ 200 km s^{-1}).

The measured projected rotational velocity of US 708 $v_{\rm rot} \sin i = 115 \pm 8$ km s^{-1} is significantly higher than the ones of both single sdB (< 10 km s^{-1}) and He-sdO stars ($20 - 30$ km s^{-1}) indicating a close-binary origin. In a very compact binary with short orbital period and high companion mass, the rotation is expected to be synchronised to the orbital motion. Assuming the angular momentum is unchanged when a SN occurs, the ejected donor remnant should remain a fast rotator.

It was proposed by Geier et al. (2013) that CD-30° 11223 might be a possible progenitor of US 708. However, the ejection velocity required from the new results is about 250 km s^{-1}
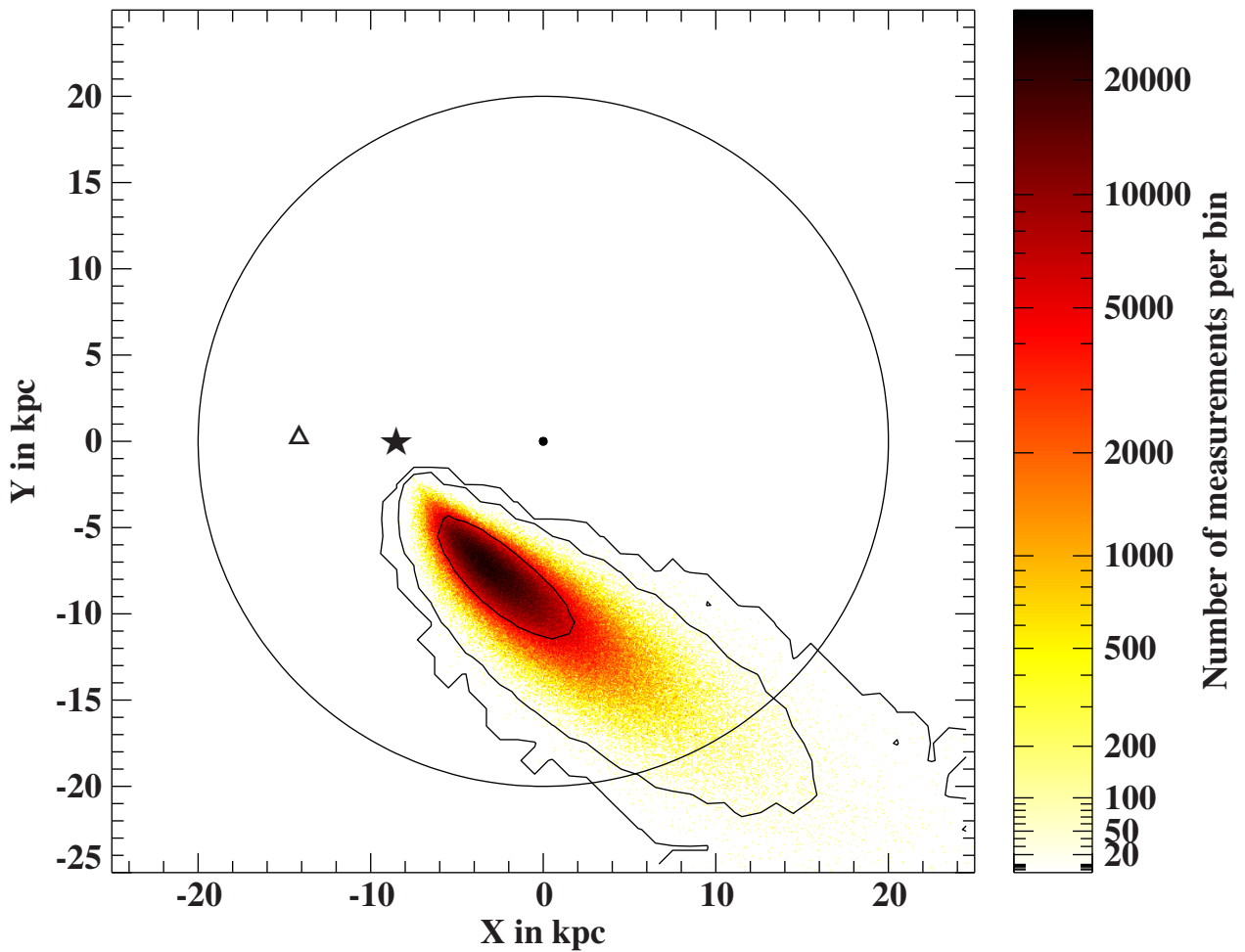
Figure 6.2: Disk passages of US 708 from a Monte Carlo simulation of its past trajectories viewed from the North Galactic pole. Colour-coded are the bins of the positions where the star crossed the Galactic disk (indicated as black circle). The solid lines correspond to the 1σ, 3σ, and 5σ contours. The GC is given by the black dot, the position of the Sun is marked by the star, and the current position of US 708 is denoted by the triangle. (Geier et al., 2015a)
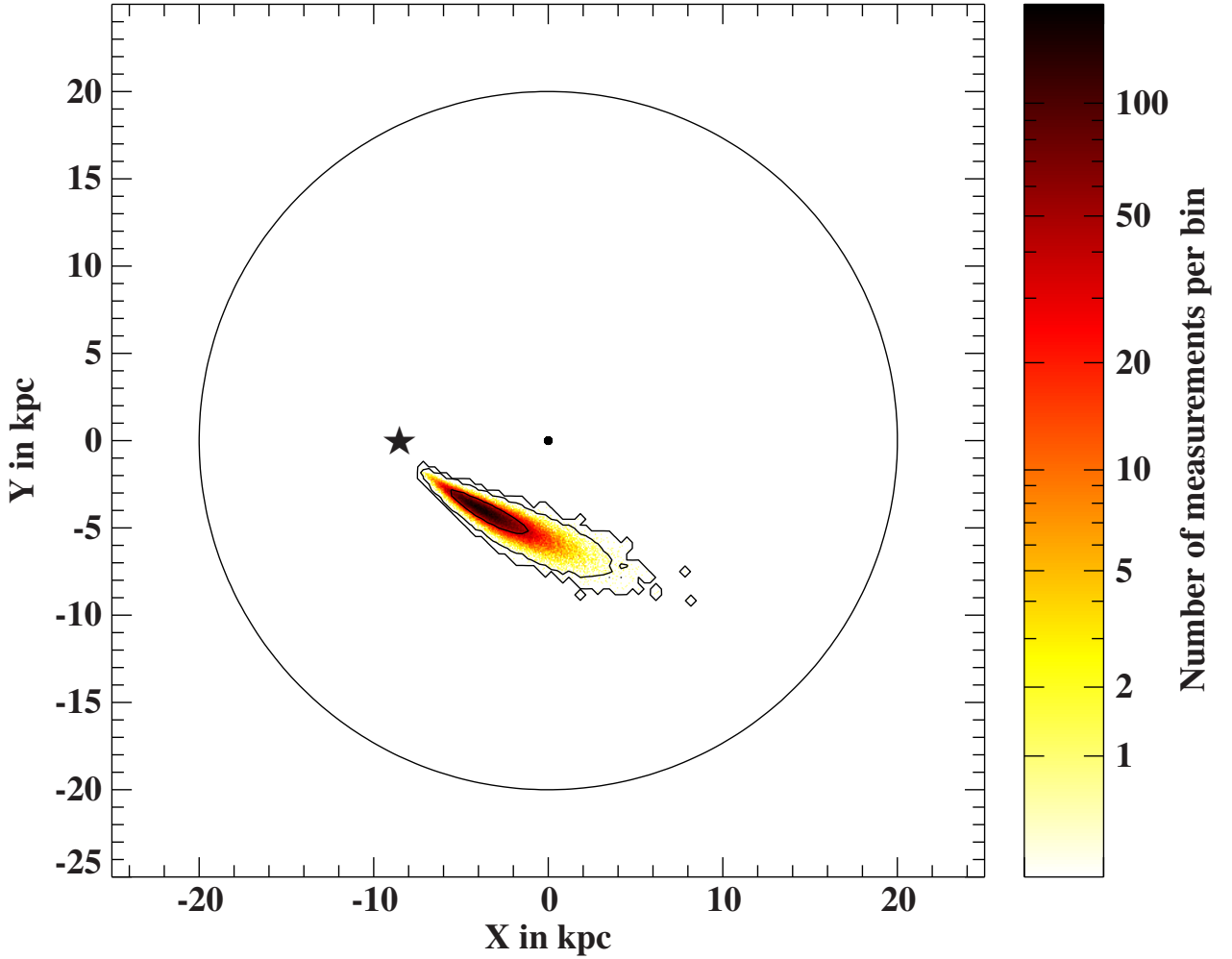
Figure 6.3: Same as Figure 6.2 calculated with proper motion of Brown et al. (2015)

higher than assumed. Based on the new constraints, consistent solutions could be found for low He-star masses ($\sim 0.3 - 0.35\,M_\odot$) and high WD companion masses ($> 1.0\,M_\odot$) (Geier et al., 2015a).

Brown et al. (2015) were able to perform independent proper motions for US 708 with three epochs of the HST. Their values are much more accurate and differ especially in declination from our values ($\mu_\alpha \cos\delta = -7.33 \pm 0.58$ mas yr^{-1}, $\mu_\delta = 2.28 \pm 0.55$ mas yr^{-1}). This brings the value of the declination closer to the theoretical needed proper motion value for US 708 to originate from the GC. To verify our results, we repeated the Monte Carlo simulation with their values but reduced the number of trajectories to 10^6. The Galactic rest-frame velocity is reduced to $v_{\mathrm{GRF}} = 1157 \pm 53$ km s^{-1} and the ejection velocity from the disk is reduced to $v_{\mathrm{ej}} = 998 \pm 68$ km s^{-1}. However, the result of the origin remains the same. Figure 6.3 shows that the area of the disk passage shrinks due to the lower uncertainties. But also with these proper motions, the star is not coming from the GC

6.3 J1211 - a hypervelocity binary candidate

Motivated by the results of the successfull reobservation of US 708 more hot subdwarfs with extreme kinematics were reobserved. The fastest object discovered by Tillich et al. (2011) is another outstanding candidate is SDSS J121150.27+143716.2 (J1211). Tillich et al. (2011) traced its origin back to the outskirts of the Galaxy and found the star to be most likely unbound. The following results are published in Németh et al. (2016).

Surprisingly, new ESI and XSHOOTER spectra revealed a cool companion. The absorption lines of both, the sdB and its K-star companion, are shifted by about 240 $\mathrm{km\,s^{-1}}$ and no radial velocity shift was detected in the 18 available spectra over a timebase of nine years. The orbital period is supposed to be several hundred days and the separation of the stars of several AU.

Using the proper motion of Tillich et al. (2011) and a combined spectroscopic and photometric distance of $d = 5.5 \pm 0.5$ kpc J1211 has a Galactic rest-frame velocity of $v_{\mathrm{GRF}} = 571.3 \pm 76.4$ $\mathrm{km\,s^{-1}}$. This value is close to the Galactic escape velocity which is very much dependent of the actual mass of the halo. Therefore we tested the dynamical properties of J1211 in three different mass models, see Chapter 3.4.3 and models I, II, and III of Irrgang et al. (2013).

It turned out that J1211 is bound with a probability of 99.7% in the most massive model (model III) while in the least massive model (model II) only 40.3% of the trajectories are bound. Model I has a probability of 62.4% bound trajectories. Figure 6.4 shows exemplarily the disk passage and the orbit of J1211 using the most massive Galactic potential, model III of Irrgang et al. (2013). It also shows an estimated orbit of J1211 in the $x - y$-plane and in the $r - z$-diagram calculated 10 Gyr over the past. The other models show similar behaviour.

J1211 is the first and yet only binary HVS candidate. An origin in the GC can be excluded irrespective of the choice of the mass model and therefore the disruption of a hierarchical triple system by the SMBH. That a hierarchical triple system could be ejected through the interactions with the SMBH as a close hypervelocity binary was suggested by Perets (2009). But neither does J1211 come from the GC nor is it a close binary. The SN channel can also be excluded as well as any kind of close encounter with other objects that could possibly lead to such accelerations. A wide binary like this is too fragile to survive these kinds of interactions. Hence, it lacks any explanation. We suggest the formation in the halo or the acceleration from the tidal debris of a dwarf galaxy that was disrupted by the Milky Way (Abadi et al., 2009). It was not possible to associate J1211 with any of the known stellar streams. However, should this be the case, more objects on similar trajectories should be existing which should be discovered by *Gaia* astrometry. Figure 6.5 shows the position of J1211 on the sky in the past.
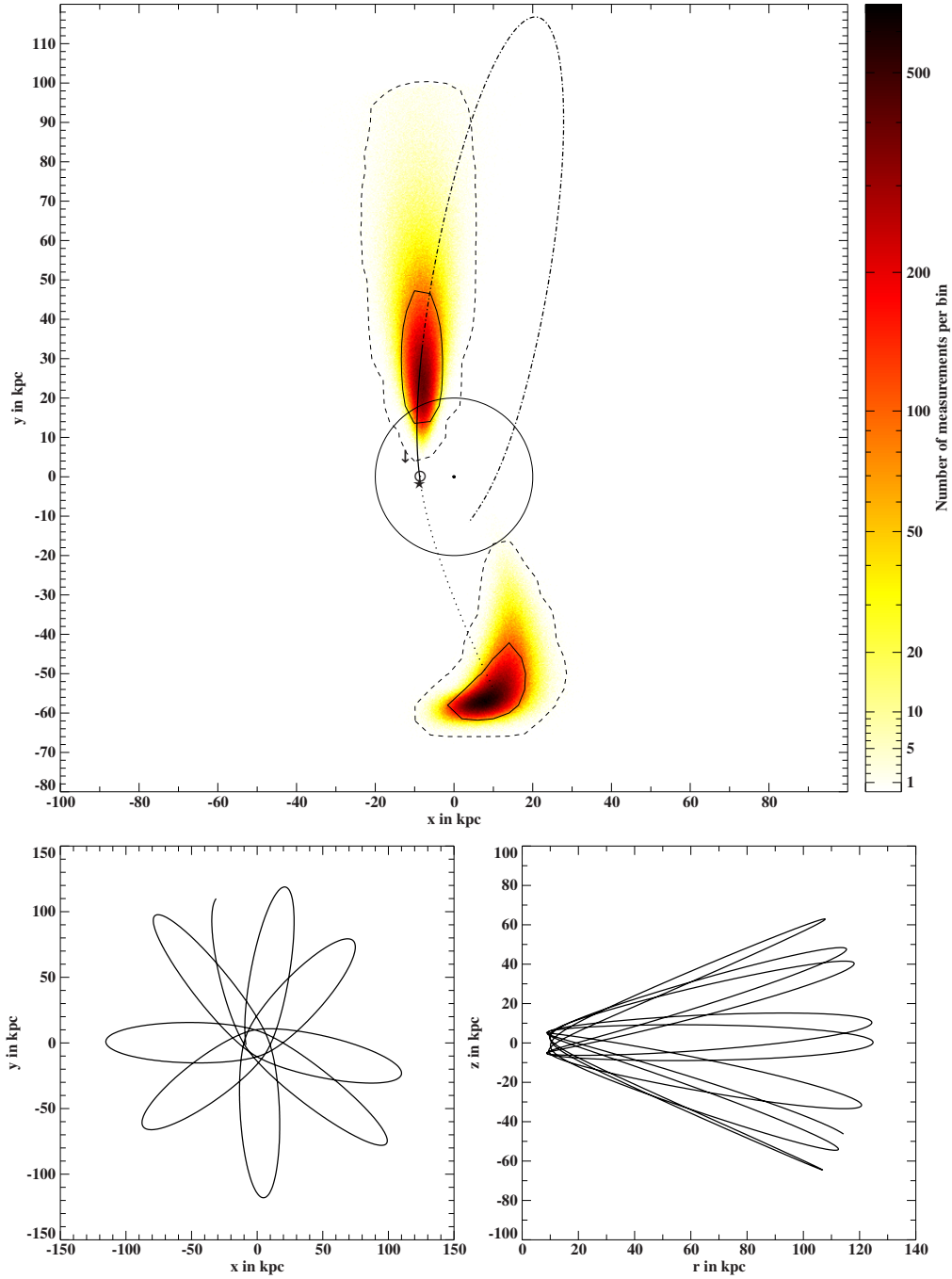
Figure 6.4: Top panel: disk passages (binned and colour coded) of J1211 using model III of Irrgang et al. (2013) with 1σ (solid) 3σ (dashed) contours. The upper passage belongs to the past, the lower passage to the future. The projection of one orbit onto the x-y-plane is shown in the past with the dash-dotted line for $z < 0$, with a full line from $z = 0$ at the disk passage to the current position, and with a dotted line from the current position to the next disk passage in the future. The black dot represents the position of the GC, the solar symbol marks the position of the Sun, and the star denotes the current position of J1211. The arrow points into flightdirection. Bottom panels: estimated orbits of J1211 in the x-y-plane (left) and r-z-diagram. (Németh et al., 2016)
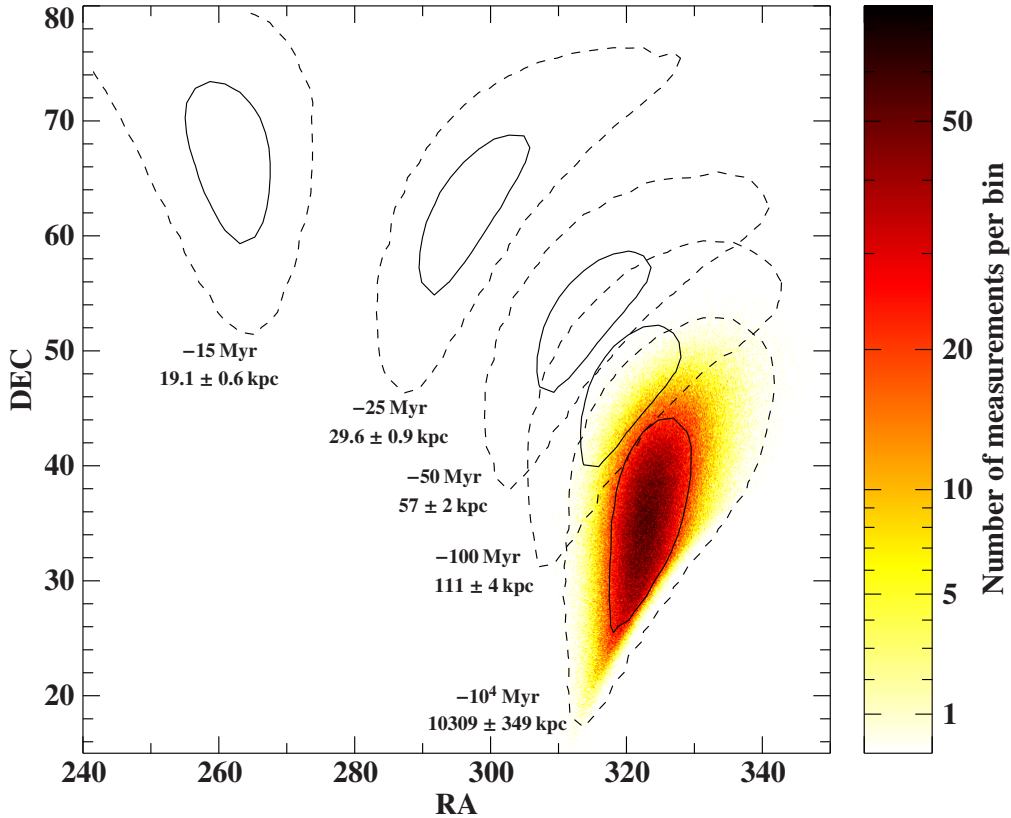
Figure 6.5: Positions of J1211 in the past with 1 and 3σ contours. (Németh et al., 2016)

6.4 Spectroscopic twin to US 708 and three fast sdBs

The results of this section are published in Ziegerer et al. (2017) and the text is based on this publication.

The sdB star SDSS J123137.56+074621.7 (J1231) and the He-sdO star SDSS J205030.39−061957.8 (J2050) have been discovered as new objects with extreme kinematics (Geier et al., 2015b). SDSS J163213.05+205124.0 (J1632) and SDSS J164419.44+452326.7 (J1644) have previously been investigated by Tillich et al. (2011) and are now revisited here. They were reobserved with higher quality data to improve the constraints on their origins and kinematics.

As for the previous stars, preliminary atmospheric parameters, spectroscopic distances, and radial velocities have been obtained from low-resolution SDSS spectra for the preselection of interesting candidates. For the more accurate analyses spectra taken with the SDSS/BOSS, Keck/ESI, ESO-VLT/XSHOOTER, and ESO-VLT/FORS1 spectrographs were used. All spectra were used to search for radial velocity variations in order to search for possible companions. A quantitative spectral analysis also provided the atmospheric parameters effective temperature T_{eff}, surface gravity $\log g$, and helium abundance, as well as limits on the projected rotational velocity $v_{\mathrm{rot}} \sin i$. The results are listed in Table 6.1.

Name	Short	Type	V	A_V	T_{eff}	$\log g$	$\frac{\log n(\mathrm{He})}{\log n(\mathrm{H})}$	$v_{\mathrm{rot}}\sin i$	v_{RV}	d
			(mag)	(mag)	(K)	(cgs)		(km/s)	(km/s)	(kpc)
SDSS J123137.56+074621.7	J1231	sdB	17.44	0.05	25200 ± 500	5.13 ± 0.05	-2.23 ± 0.05	< 45	467 ± 2	$6.3^{+0.5}_{-0.5}$
SDSS J163213.05+205124.0	J1632	sdB	17.62	0.15	28900 ± 500	5.61 ± 0.05	-1.83 ± 0.03	< 33	-239 ± 4	$4.3^{+0.3}_{-0.3}$
SDSS J164419.44+452326.7	J1644	sdB	17.39	0.03	33600 ± 500	5.73 ± 0.05	< -3.0	< 38	-309 ± 9	$4.1^{+0.3}_{-0.3}$
SDSS J205030.39−061957.8	J2050	He-sdO	18.22	0.20	47500 ± 1000	5.70 ± 0.1	$> +2.0$	< 38	-509 ± 19	$7.0^{+0.9}_{-0.8}$

Table 6.1: Atmospheric parameters: apparent magnitude V, reddening in V A_V, effective temperature T_{eff}, gravity $\log g$, helium abundance, projected rotational velocity $v_{\mathrm{rot}}\sin i$, radial velocity v_{RV}, and d is the heliocentric distance. (Ziegerer et al., 2017)

The three sdB stars have typical effective temperatures. However, it is worth mentioning that the low gravity of J1231 implies that the star is close to termination of core helium burning, possibly even beyond that phase. The helium content of J1231 and J1632 is typical for the majority of sdB stars. However, no helium lines could be detected in the hot J1644, which implies that its abundance (He/H $< 1/1000$) is considerably lower than expected for sdBs of similar temperature (Edelmann et al., 2003). The sdO star J2050 does not show any hydrogen, and a lower limit of the helium-to-hydrogen ratio of 100 is given. Its temperature, gravity, and helium content are typical for He-sdO stars (Stroeer et al., 2007), in particular similar to that of the hypervelocity sdO star US 708 (Geier et al., 2015a). For US 708 an unexpected high projected rotational velocity of $v_{\mathrm{rot}}\sin i = 115 \pm 8\,\mathrm{km\,s^{-1}}$ was found. In comparison to US 708, these four stars show moderate $v_{\mathrm{rot}}\sin i < 45\,\mathrm{km\,s^{-1}}$. A photometric consistency check was performed by fits of the observed SED. The obtained values for distances and reddening from SED-fitting fit to those obtained by spectroscopy within their uncertainties.

Photometric magnitudes from GALEX DR6[13] and SDSS DR12 were available for all stars. BATC DR1[14], UKIDSS DR9 (Lawrence et al., 2007), and ALLWISE (Cutri & et al., 2013) were only available for J1231. Therefore, data in the infrared were only available for one star, and it was possible only for this one star to search for an infrared excess as an indication for a cooler companion. There is no sign of a cooler companion as was seen in the SED of the fast sdB star J1211 (Németh et al., 2016). Absorption lines of the companion of J1211 were also visible in the spectrum. No such lines were found in the four stars. Hence, there is no evidence for a cool companion to any of these four program stars.

6.4.1 Proper motions

The proper motions of the program stars were either taken from Tillich et al. (2011) or determined by the same method as described in Chapter 3.3.1. The comparison of our proper motions with catalogues such as APOP (Qi et al., 2015), HSOY (Altmann et al., 2017), PPMXL (Roeser et al., 2010), SDSS (Ahn et al., 2012), USNO-B1.0 (Monet et al., 2003), and UCAC4 (Zacharias et al., 2013) showed that our values are in good agreement within the uncertainties, see Table 6.2. The HSOY catalogue is a combination of *Gaia* DR1

---

[13]Available in the MAST archive: http://galex.stsci.edu/GR6/?page=mastform
[14]http://vizier.cfa.harvard.edu/viz-bin/Cat?II/262

Name	$\mu_\alpha \cos\delta$	μ_δ	catalogue
	(mas yr^{-1})	(mas yr^{-1})	
J1231	-7.9 ± 3.4	-5.0 ± 2.8	this work
	-2.5 ± 1.3	-6.8 ± 1.9	APOP
	-10.5 ± 2.5	-7.0 ± 2.5	HSOY
	-7.5 ± 5.6	-4.1 ± 5.6	PPMXL
	-4 ± 3	-2 ± 3	SDSS
J1632	-12.5 ± 3.0	-1.6 ± 3.6	T11
	-8 ± 2.7	-3.5 ± 3.4	APOP
	-16.6 ± 5.3	-5.8 ± 5.3	PPMXL
	-13 ± 3	-4 ± 3	SDSS
	-10 ± 2	0 ± 2	USNO-B1.0
J1644	4.7 ± 2.8	-26.1 ± 3.3	T11
	-1.1 ± 3.2	-16.4 ± 3.2	APOP
	-7 ± 5.9	-27.5 ± 5.9	PPMXL
	-1 ± 3	-26 ± 3	SDSS
	-2 ± 6	-26 ± 3	USNO-B1.0
J2050	5.5 ± 4.8	-8.9 ± 3.5	this work
	3.2 ± 3.7	-2.9 ± 2.1	APOP
	1.8 ± 2.4	-9.7 ± 2.4	HSOY
	-3.8 ± 6.2	-7.5 ± 6.2	PPMXL
	0 ± 3	-4 ± 3	SDSS

Table 6.2: Comparison of catalogue proper motions. The first line represents the applied proper motion, respectively. Either proper motion by Tillich et al. (2011) (T11) or own proper motions were used. (Ziegerer et al., 2017)

and PPMXL data. The resulting values are in good agreement with the values of our proper motion with smaller uncertainties than for PPMXL alone.

For J1644 alone, the values for one of the two proper motion ($\mu_\alpha \cos\delta$) components differ between the different measurements. Therefore, we discuss two different options for J1644. First, we use the proper motion obtained by Tillich et al. (2011), and second, a weighted mean of the catalogue values (denoted as J1644b). For the remaining program stars we used our proper motion or the one obtained from Tillich et al. (2011) for the further analysis.

6.4.2   Extreme halo or ejected stars

Trajectories for the four stars were calculated for four different mass models in the way described in Chapter 3.4.3 to trace the orbits back to the Galactic disk to obtain their dynamical properties and possible origins. All resulting velocity components and the probability of being bound for models I, II, and III of Irrgang et al. (2013) and the model of Rossi et al. (2017) can be found in Table 6.3 (1σ uncertainties are given). As can be seen, the choice of model potential is of no importance because all velocities derived from the different models agree within their mutual uncertainties. While J1632 is certainly bound to the Galaxy, the

Name/ Model	v_x (km/s)	v_y (km/s)	v_z (km/s)	v_r (km/s)	v_ϕ (km/s)	v_{GRF} (km/s)	v_{ej} (km/s)	bound
J1231	-66 ± 97	-136 ± 86	378 ± 29	99 ± 102	-114 ± 81	428 ± 32		
I	-157 ± 105	-144 ± 76	429 ± 27	128 ± 102	-152 ± 111	495 ± 51	611 ± 67	99.9%
II	-156 ± 105	-146 ± 76	429 ± 27	127 ± 102	-154 ± 111	495 ± 51	612 ± 67	99.3%
III	-154 ± 104	-146 ± 76	429 ± 27	125 ± 102	-154 ± 110	494 ± 51	612 ± 67	100%
R	-153 ± 106	-147 ± 76	435 ± 27	124 ± 102	-155 ± 111	499 ± 51	617 ± 67	99.5%
J1632	-179 ± 58	-39 ± 61	33 ± 50	155 ± 67	-97 ± 51	203 ± 54		
I	-305 ± 58	144 ± 79	256 ± 63	-4 ± 143	-304 ± 103	435 ± 62	612 ± 65	100%
II	-306 ± 60	152 ± 82	254 ± 64	-11 ± 145	-309 ± 104	438 ± 63	616 ± 65	100%
III	-302 ± 58	131 ± 76	263 ± 64	16 ± 134	-300 ± 96	432 ± 65	609 ± 65	100%
R	-317 ± 70	185 ± 113	281 ± 90	39 ± 153	-339 ± 114	481 ± 92	661 ± 90	100%
J1644	433 ± 72	-83 ± 41	-257 ± 42	-432 ± 73	84 ± 41	514 ± 69		
I	-467 ± 117	-66 ± 104	430 ± 82	40 ± 252	402 ± 145	660 ± 51	553 ± 50	91.5%
II	-451 ± 120	-72 ± 112	430 ± 88	72 ± 250	381 ± 149	652 ± 52	551 ± 53	79.3%
III	-489 ± 118	-40 ± 95	435 ± 78	-1 ± 267	410 ± 155	675 ± 58	568 ± 55	100%
R	-489 ± 90	-48 ± 128	372 ± 102	338 ± 181	304 ± 162	640 ± 64	572 ± 44	84.5%
J1644b	355 ± 70	-142 ± 51	-162 ± 55	-382 ± 72	0 ± 49	422 ± 69		
I	-408 ± 148	116 ± 124	247 ± 159	312 ± 252	97 ± 218	527 ± 161	546 ± 116	99.5%
II	-396 ± 153	114 ± 125	237 ± 159	316 ± 239	87 ± 209	511 ± 168	537 ± 120	97.9%
III	-424 ± 136	132 ± 119	267 ± 159	302 ± 277	90 ± 231	551 ± 149	570 ± 112	100%
R	-488 ± 90	-48 ± 128	372 ± 102	338 ± 181	304 ± 162	640 ± 64	572 ± 44	84.5%
J2050	-299 ± 73	-191 ± 71	107 ± 92	52 ± 139	-332 ± 66	394 ± 40		
I	-114 ± 149	46 ± 74	-104 ± 35	-94 ± 144	-107 ± 41	215 ± 92	385 ± 79	99.8%
II	-120 ± 146	41 ± 74	-102 ± 35	-101 ± 142	-104 ± 41	215 ± 93	383 ± 80	99.6%
III	-91 ± 160	53 ± 79	-107 ± 38	-69 ± 157	-110 ± 39	217 ± 92	389 ± 78	100%
R	-140 ± 140	33 ± 76	-112 ± 35	-118 ± 138	-106 ± 43	226 ± 94	390 ± 82	99.7%

Table 6.3: Velocity components and the probability of being bound to the Galaxy. The values of the first line are the current values, next lines are the values at the last disk passage based on models I, II, and III of Irrgang et al. (2013) and the model of Rossi et al. (2017, R), respectively. (Ziegerer et al., 2017)

probability that J1231, J1644, and J2050 are unbound is also low, regardless of the choice of Galactic potential. Therefore we conclude that our program stars belong to an old Galactic stellar population and investigate their kinematical properties from long-term evolution of their Galactic orbits.

Figure 6.6 shows the position of the four hot subdwarf stars in the $v_r - v_\phi$-velocity diagram compared to 3σ contours of the thick and thin disk as introduced by Pauli et al. (2006). All stars lie well outside the disk region and can therefore be considered as halo stars.

Figure 6.7 shows the J_z-e-diagram. Thin-disk stars are located at the top left end of the diagram, having very low eccentricities e and negative J_z. Tillich et al. (2011) suggested that stars inside the box belong to the thick disk, while stars inside the ellipse are typical halo stars as they show only little effect of the disk rotation and cross the Galactic plane almost perpendicular on highly eccentric orbits. Again, our stars lie well outside the disk region.
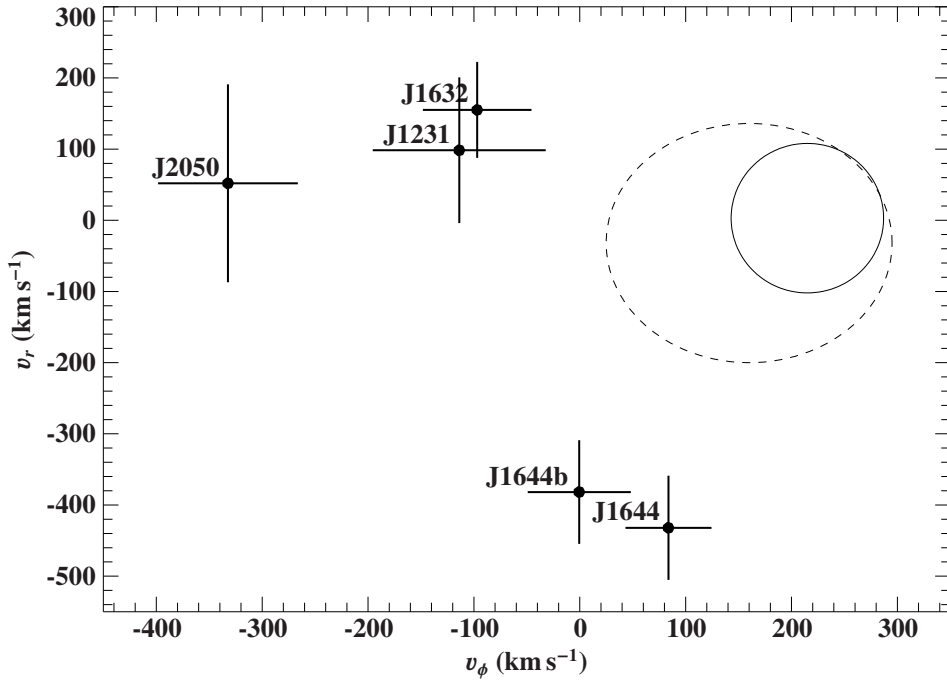
Figure 6.6: Comparison of the program stars in the $v_r - v_\phi$-velocity diagram with 3σ contour of the thick disk (dashed line) and 3σ contour of the thin disk (solid line) according to Pauli et al. (2006). (Ziegerer et al., 2017)
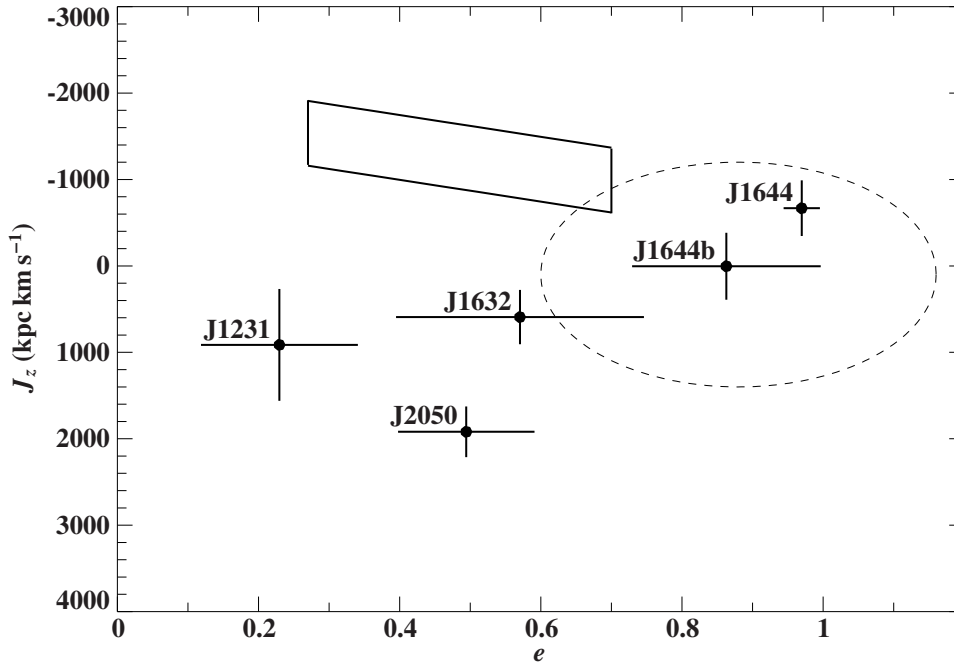
Figure 6.7: $J_z - e$-diagram, the dashed line indicates the region of typical halo stars. The solid line marks the thick-disk region. Thin-disk stars would populate the continuation of the parallelogram to lower eccentricities. (Ziegerer et al., 2017)

6.4.3   J1644 - an extreme halo star

The fastest of these four stars is also the most precarious. Because of the discrepancy in proper motions (see Section 6.4.1), we carried out the kinematic analyses twice, adopting the proper motions of Tillich et al. (2011) and a weighted mean of the catalogue values, respectively.

Regardless of the choice of the proper motion, J1644 has an extreme kinematic behaviour, as becomes obvious from its position in the $v_r - v_\phi$- and the $J_z - e$-diagrams (see Figures 6.6 and 6.7). However, the orbit strongly depends on the choice of their values, as demonstrated in the left panel of Figure 6.8. When we adopt the proper motion of Tillich et al. (2011), J1644 is on a highly eccentric orbit, which leads the star to distances of up to 129 ± 73 kpc away from the GC. The travel time since its last approach to the GC is much longer, 1558 ± 988 Myr, than the lifetime of an EHB star. If J1644 were ejected from the GC, it would have been a main-sequence star or subgiant at the time and had to evolve into an sdB on the way. Adopting the weighted mean of the catalogue proper motion values leads to a shorter travel time of only 113 ± 72 Myr and reaches only distances of 20 ± 6 kpc away from the GC, which is consistent with the EHB lifetime of < 100 Myr, meaning that it is possible to reach the star's current position within the lifetime. The right-hand panel of Figure 6.8 shows that the GC lies within the 1σ contours of the disk passages, regardless of the choice of the proper motion. Although J1644 has the highest $v_{\mathrm{GRF}} = 514 \pm 69$ km s^{-1} (or $v_{\mathrm{GRF}} = 422 \pm 69$ km s^{-1} for the weighted mean of the catalogue proper motions) of all program stars, it is heading towards the GC and must therefore still be bound.

6.4.4   Possibly ejected stars

Tillich et al. (2011) suggested that halo stars outside the ellipse in the $J_z - e$-diagram (Figure 6.7) could be ejected stars. Accordingly, J1231, J1632, and J2050, all on retrograde orbits (see Figure 6.6), could be runaway stars from the Galactic disk or bound HVS from the GC rather than extreme halo stars. While J1231, and J2050 cannot originate from the GC (see Figures 6.11 and 6.12, right panels), the disk-crossing area of the trajectories of J1632 include the GC (see Figure 6.10 right panel). We diskuss this object first before addressing the disk runaways J1231 and J2050.

J1632 - a potentially bound HVS

The analysis of its trajectory indicates that J1632 may originate from the GC and therefore could be a bound HVS (see Figure 6.10 left panel). J1632 has a relatively low $v_{\mathrm{GRF}} = 203 \pm 54$ km s^{-1} of the order of typical disk stars and is approaching us. Similarly, the velocity perpendicular to the Galactic disk is very low ($v_z = 33 \pm 50$ km s^{-1}), similar to that of a thick-disk star. In addition, the eccentricity speaks for a thick-disk star. Therefore the orbit looks like that of a typical thick-disk star (see left-hand panel of Figure 6.10). However, the star is revolving retrograde around the GC, and consequently, it cannot be an ordinary thick-disk star. Randall et al. (2015) found the intermediate He-sdB LS IV-14°116 on a similar orbit. Figure 6.10 shows the orbit of LS IV-14°116 in the $x-y$-plane and the $r-z$-diagram. It seems like that of a thick disk star with low inclination. However, it is revolving retrograde which
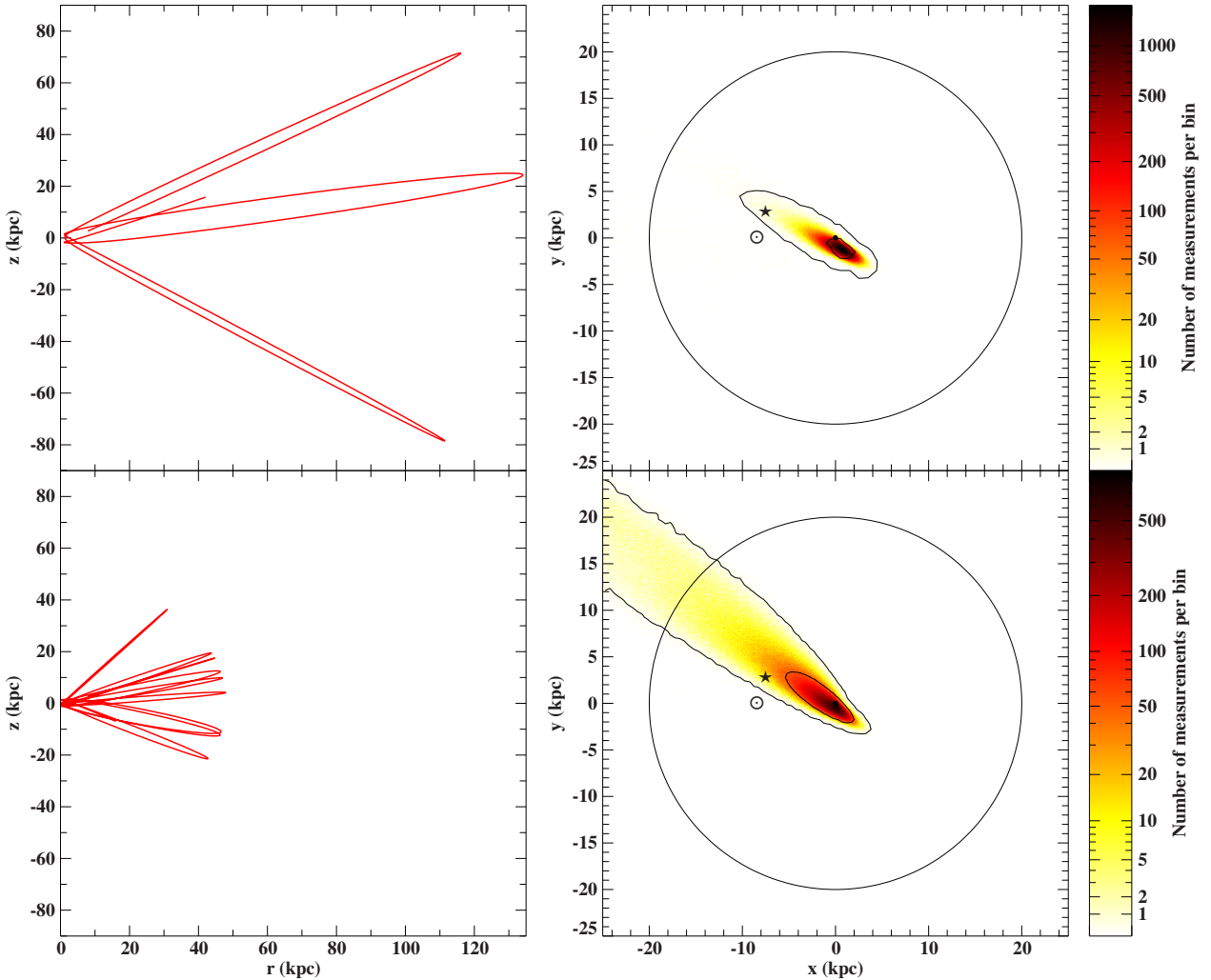
Figure 6.8: *Left panel*: $r - z$-diagram of J1644 using the Tillich et al. (2011) proper motion (top) and the weighted mean of the catalogue proper motions (bottom), respectively. *Right panel:* disk passages binned and colour-coded of J1644 with 1 and 3σ contours using the Tillich et al. (2011) proper motion (top) and the weighted mean of the catalogue proper motions (bottom), respectively. The black dot marks the GC, the star the current position of J1644, and the solar symbol the position of the Sun. The circle indicates the Galactic disk. All calculations were performed with model I of Irrgang et al. (2013). (Ziegerer et al., 2017)
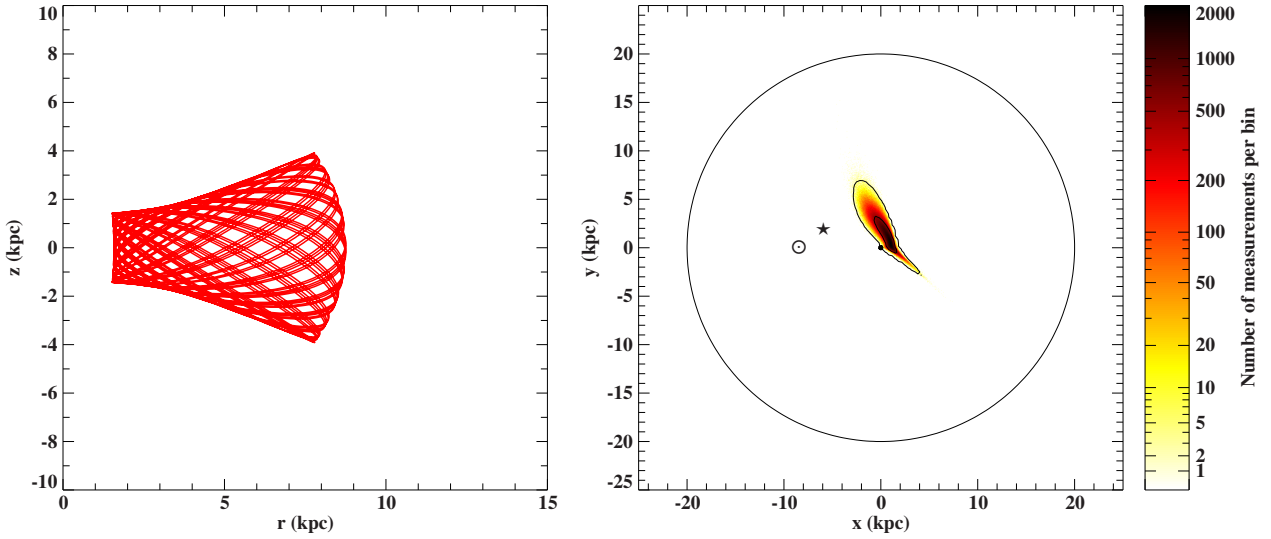
Figure 6.9: *Left panel*: $r - z$-diagram of J1632. *Right panel:* disk passages binned and colour-coded of J1632 with 1 and 3σ contours. The black dot marks the GC, the star the current position of J1632, and the solar symbol the position of the Sun. The circle indicates the Galactic disk. All calculations were performed with model I of Irrgang et al. (2013). (Ziegerer et al., 2017)

speaks for a halo membership or the ejection from the disk. LS IV-14°116 shows extremely peculiar atmospheric abundances as well as long-period pulsations that cannot be explained. And indeed, halo and globular cluster hot subdwarfs show different atmospheric properties to those in the Galactic disk (Németh et al., 2012; Latour et al., 2014).

An origin from the GC for J1632 is conceivable (see right-hand panel of Figure 6.10). Possibly, J1632 could have been ejected into a low-inclination orbit when the former binary was disrupted by the SMBH. With a travel time of 23.7 ± 5.4 Myr from the GC to its current position, this scenario is consistent with the EHB lifetime of such stars of < 100 Myr.

J1231 and J2050 - potential disk runaways

The constant radial velocity, proper motion, and spectroscopic distance of J1231 indicate a Galactic rest-frame velocity of $v_{\mathrm{GRF}} = 428 \pm 32\,\mathrm{km\,s^{-1}}$ and a likely origin in the Galactic disk rather than the GC (see right-hand panel of Figure 6.11). A travel time of 14.4 ± 1.6 Myr from the Galactic disk to its current position is consistent with the EHB lifetime of such stars of < 100 Myr. Although the star is the only one of the program stars receding from us, it is bound with a probability of 99.9%. In the context of population membership, J1231 shows a quite chaotic orbit like that of an extreme halo star (see left-hand panel of Figure 6.11). It reaches distances of more than 50 kpc away from the Galactic disk.

The traced orbits of J2050 show that the star does not approach anywhere near the GC (see right-hand panel of Figure 6.12) with a typical halo orbit (see left-hand panel Figure 6.12). With $v_{\mathrm{GRF}} = 394 \pm 40\,\mathrm{km\,s^{-1}}$ on a retrograde orbit, it has a probability of being bound of 99.8%. Its travel time from the outskirts of the Galactic disk is 113 ± 72 Myr, which is consistent with the lifetime of EHB stars.
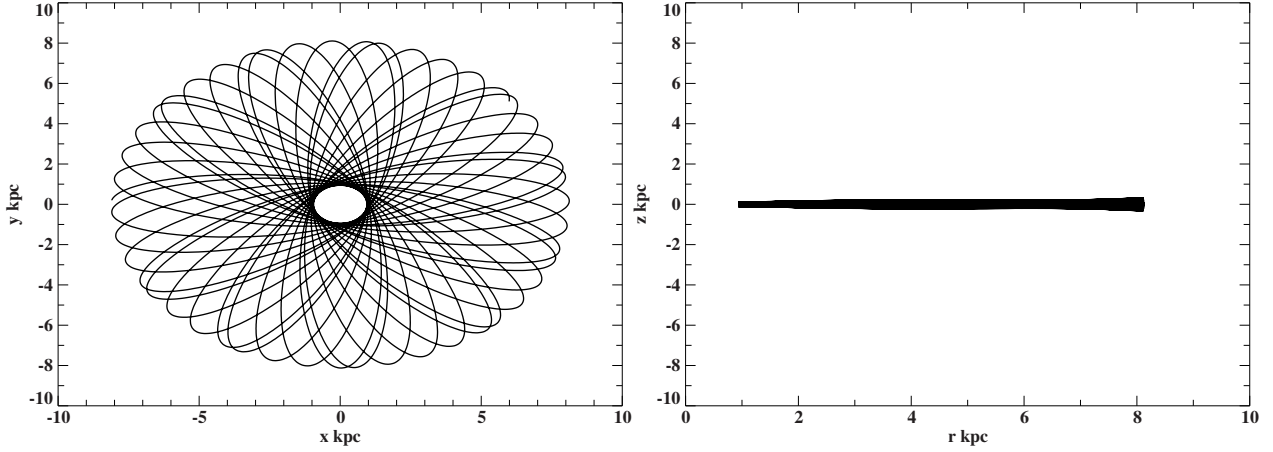
Figure 6.10: LS IV-14°116 in the $x - y$-plane and the $r - z$-diagram
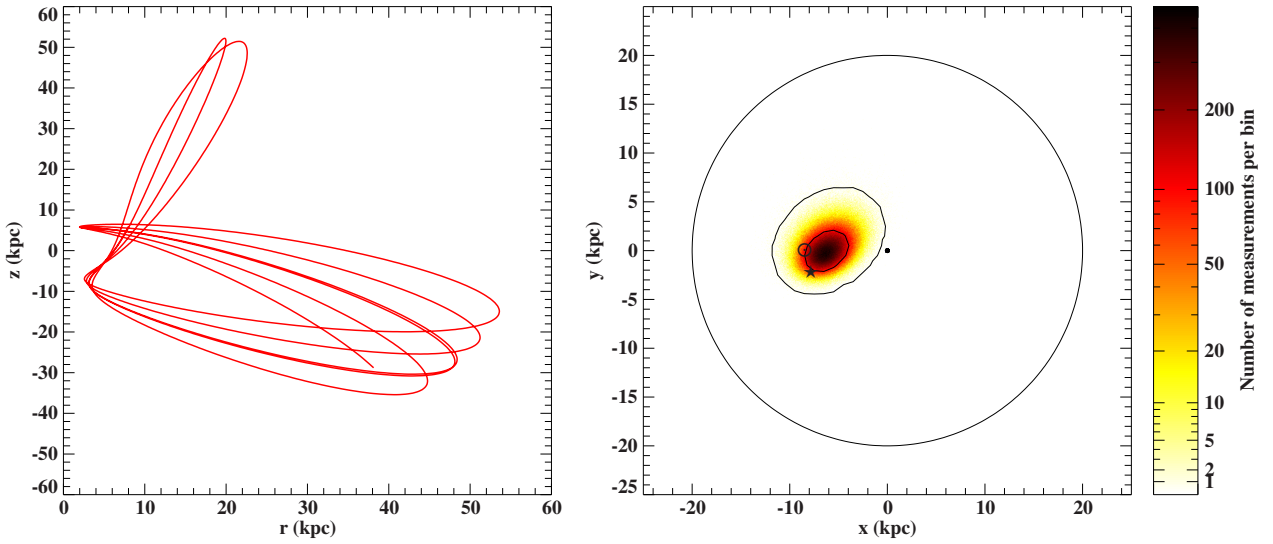
Figure 6.11: *Left panel*: $r - z$-diagram of J1231. *Right panel:* disk passages binned and colour-coded of J1231 with 1 and 3σ contours. The black dot marks the GC, the star the current position of J1231, and the solar symbol the position of the Sun. The circle indicates the Galactic disk. All calculations were performed with model I of Irrgang et al. (2013). (Ziegerer et al., 2017)
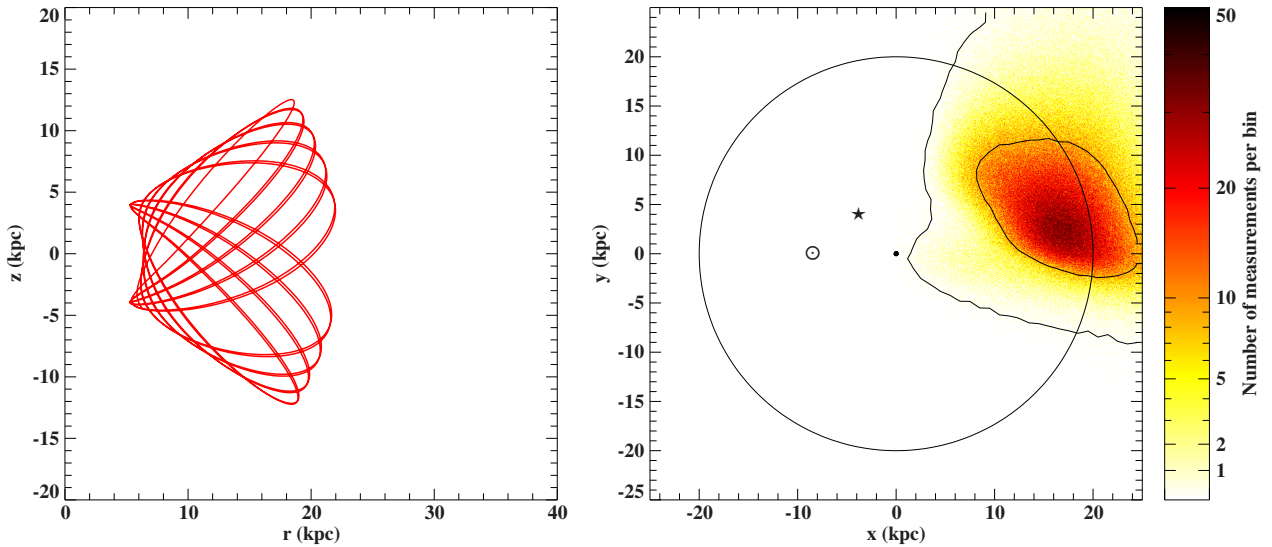
Figure 6.12: *Left panel*: $r - z$-diagram of J2050. *Right panel:* disk passages binned and colour-coded of J2050 with 1 and 3σ contours. The black dot marks the GC, the star the current position of J2050, and the solar symbol the position of the Sun. The circle indicates the Galactic disk. All calculations were performed with model I of Irrgang et al. (2013). (Ziegerer et al., 2017)

6.5 Conclusions

We have performed a spectroscopic and kinematic follow-up analysis of the only confirmed HVS hot subdwarf, three known hot subdwarfs from the first Hyper-MUCHFUSS campaign as well as two new ones with extreme kinematics. Radial velocity measurements, spectral identification, and photometry (when available) were used to exclude binarity or variability of the stars. Proper motions were either taken from Tillich et al. (2011) or measured in the same way. The goal of this work was to place constraints on the place of origin of the stars and the possible mechanisms that led the stars to their extreme kinematics.

While we cannot rule out that the program stars could be genuine halo stars on extreme Galactic orbits, we considered the relevance of three ejection scenarios for our program stars, that is, the Hills scenario, the binary supernova scenario, and a potential extragalactic origin. The Hills slingshot scenario may be valid only for two of our program stars because their last disk passages came close to the GC (J1632 and J1644). The lifetime of EHB stars is about 100 Myr. If the stars have been formed in a binary and then have been disrupted by the SMBH, the travel time from the GC to their current position must be consistent with this lifetime. This is the case for J1632. For J1644 this is only the case if we adopt the weighted mean of the catalogue proper motions, however. When we adopt the proper motion we measured on our own, the travel time is far too long, which means, if this scenario is true, that the star must have evolved to an sdB after the former binary was disrupted by the SMBH through one of the single evolution channels for hot subdwarfs. Another option is the disruption of a hierarchical triple by the SMBH and the subsequent production of an sdB through the merger of two helium white dwarfs. Alternatively, the star has evolved to an sdB with a low-mass
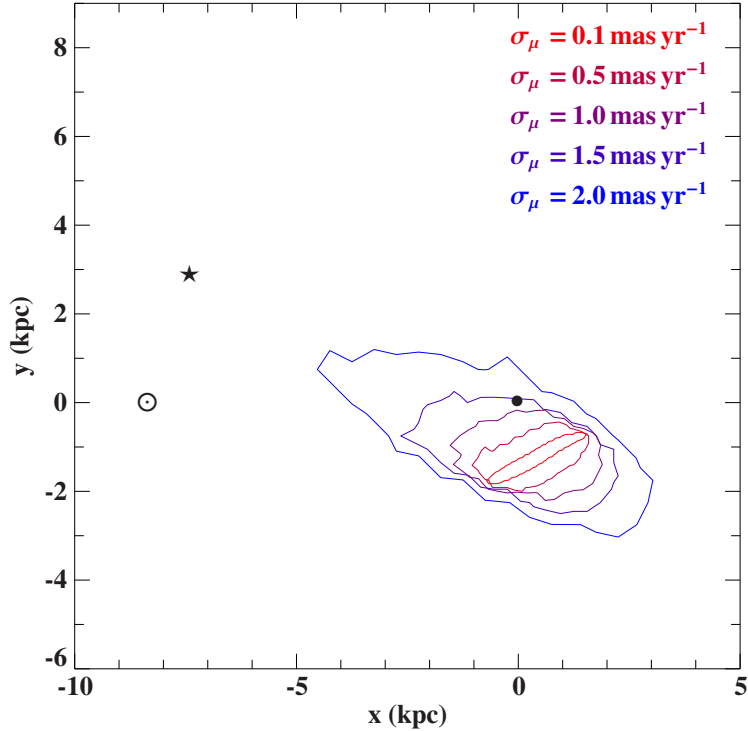
Figure 6.13: Disk passage 3σ contour of J1644 using the Tillich et al. (2011) proper motion as in Fig. 6.8 (upper right) and for uncertainties σ_μ reduced from $2.0\,\mathrm{mas\,yr^{-1}}$ to $0.1\,\mathrm{mas\,yr^{-1}}$. The latter is expected to be the *Gaia* end-of-mission accuracy. The black dot marks the GC, the star the current position of J1644, and the solar symbol the position of the Sun. (Ziegerer et al., 2017)

companion, such as a planet, that probably did not survive the common-envelope phase. Accurate astrometry by *Gaia* will solve this uncertainty in the proper motion measurements. Figure 6.13 shows how the area of disk passages shrinks when the uncertainties in proper motion are reduced. An uncertainty of $0.1\,\mathrm{mas\,yr^{-1}}$ was also applied, which is a realistic uncertainty that the *Gaia* mission will provide (de Bruijne, 2012).

As the star with the highest velocity known (US 708, Geier et al., 2015a) is a hot subdwarf that was not accelerated by the slingshot mechanism but rather a supernova explosion in a close binary, this is the scenario that should be considered next. J2050 is a spectroscopic twin of US 708 and therefore a promising candidate of a surviving secondary of a supernova, as proposed for US 708. It could be originating from a system similar to CD–30° 11223 (Geier et al., 2013). For J2050 the ejection velocity $v_{\mathrm{ej}} = 385 \pm 79\,\mathrm{km\,s^{-1}}$ and the $v_{\mathrm{rot}} \sin i < 38\,\mathrm{km\,s^{-1}}$ are both moderate in comparison to the values of US 708: $v_{\mathrm{ej}} = 998 \pm 68\,\mathrm{km\,s^{-1}}$, $v_{\mathrm{rot}} \sin i = 115 \pm 8\,\mathrm{km\,s^{-1}}$. As subdwarfs in compact binaries are assumed to have been spun up by the tidal influence, the progenitor system does not need to have been as tight as CD–30° 11223. The progenitor system of J2050 could have had properties similar to that of the sdB + WD binary KPD 1930+2752 (Maxted et al., 2000; Geier et al., 2007). In this system, the time in which the two objects will merge as a result of the radiation of gravitational waves

is about twice as long as the lifetime of the sdB on the EHB. Owing to the shrinkage of the orbit, Roche-lobe overflow might be possible before the sdB evolves into a white dwarf (Geier et al., 2007). The travel time from the disk to the current position of J2050 is consistent with the lifetime. The same is true for the potential disk runaway sdB star J1231.

The accretion scenario has been proposed by Németh et al. (2016) in order to explain the origin of the binary sdB J1211. According to this, J1211 was accreted from the debris of a destroyed satellite galaxy. This scenario could also be valid for our program stars. If this is the case, the stars should belong to stellar streams in the halo that are yet to be discovered from *Gaia* astrometry.

Chapter 7

Outlook

The *Gaia* mission will measure accurate space-based proper motions of all stars brighter than ~ 21 mag. The end-of-mission proper motions will be one or two orders of magnitude more accurate ($0.03 - 0.6$ mas yr^{-1}) than currently available ground-based proper motions ($\sim 1.0 - 5.0$ mas yr^{-1}). Its precursor Hipparcos reached an accuracy of ~ 1.0 mas yr^{-1}. The second *Gaia* data release, which is the first to include proper motions based on *Gaia* data only, is scheduled for April 2018 followed by yearly releases with higher accuracy until the final catalogue will be published in 2022. The accuracy of the kinematic analysis will then be limited by the accuracy of the spectroscopic distances derived from the atmospheric parameters. Of course, *Gaia* will also provide parallaxes with unprecedented precision. This will allow us using near-by stars to test the accuracy of the spectroscopic distances derived from detailed quantitative spectroscopy using model atmospheres. The accuracy of spectroscopic parallaxes is limited by the uncertainties of the surface gravity (~ 0.05 dex) which translates into distance errors of 7%. The accuracy of the *Gaia* distances ranges from 0.001% for the stars nearest to the Sun to 20% for stars with distances of about 10 kpc. Thus, *Gaia* parallaxes will be more accurate than spectroscopic distances only for stars closer than roughly about $2 - 4$ kpc, dependent of the spectral type. However, the known HVSs are all more distant than that (up to 100 kpc), which reinforce the need for detailed quantitative spectral analyses.

Having this precision at hand, the adopted mass potentials will need improvement. The rotating bar, the spiral arms, and globular clusters in the halo are not included in the models. Their influence may not remain negligible when the orbits are traced back to the Galactic plane with the precision needed. Trajectories that reach large distances from the GC may be affected by satellite galaxies of the Milky Way which are also not included in the models except of the LMC (Fink, 2013). As one of the goals of *Gaia* is to provide a 3D-map of our Galaxy including the motion of the stars down to 20 mag, we may be able by the end of this mission to develop a new complex and time-dependent mass model of yet unprecedented accuracy.

In order to find more HVS candidates the massive stars of spectral type O and B may seem the most promising candidates as they are very bright and only live for a few million years so they should be found close to their birthplace and flighttime considerations can easily be applied when these stars are found far-off from star-forming regions. However, we

have to search for all kinds of stars as different acceleration mechanisms may apply for the different kinds of stars. In particular for the hot subdwarf stars, we will have to crossmatch the catalogue of stars from the MUCHFUSS project (> 5500 stars, Geier et al., 2017) with the catalogue from *Gaia* for proper motions and parallaxes. However, we have learned from the P14 sample that searching for the stars with the highest proper motion values does not neccessarily lead to finding the fastest stars. We will need to perform this task with great care to make sure to exclude outliers and false positive measurements to get a clean sample of candidates by crosschecking other independent proper motion catalogues for consistency. A radial velocity follow-up is then required for the proper motion selected stars as *Gaia* measures the radial velocity down to about 17 mag. However, the spectral range, which is chosen in the near-infrared to include the CaII triplet, is not suited for early-type stars as the lines are not visible in their spectra. Nevertheless, *Gaia* photometry and ground-based photometric surveys (e.g. Skymapper) will allow a HVS survey of the Southern hemisphere, which is of utmost importance to study the dark matter distribution of the halo.

A sample of at least 50-100 HVSs from a search covering the whole sky to get their spatial distribution is needed to put constraints on ejection mechanisms (Levin, 2006; Abadi et al., 2009; Zhang et al., 2013). Again, *Gaia* will perform this task of covering the whole sky. If J1211, for example, is the debris of a destroyed satellite galaxy the remaining stellar stream in the halo should be discovered by *Gaia* astrometry and there should exist several other stars on similar orbits.

Acknowledgements

Thank you Uli for your never ending patience, all your support and the great opportunities you gave me (including not only to travel to remote places for observing, visiting conferences, summer schools, introducing me to the sdOB community, supervising undergraduate students and so on, but also giving interviews, writing a popular science article, and even pretending to be an actress).

Thank you Stephan for supporting me the whole time even after you left Bamberg. It is an interesting journey to work with you, we never know where we end up, on purpose or by chance, but it is always worth the try. Sorry Andreas#1 for wasting your precious time, for being so blond, for asking you these absolutely not groundbreaking questions and for hugging you from time to time (against your will). But thank you for giving me your time and patience and for so many funny moments. Thanks to all the current and former members of the stellar group for making the work environment so pleasant and fruitful, especially the ones I have been working close together with: Peter, Veronika, Marco, Thomas, Christian, Simon. I wouldn't have survived university bureaucracy without Edith, thank you!

To all colleagues at the observatory: Thank you for making this place more than just a working place. You are more than just colleagues, some of you became really good friends. Thank you for sharing all the joy and pain, for crying and laughing together. I am pretty sure to forget someone so I hesitate to list all the names. I greatly enjoyed our skiing trips, I hope we'll do this until we're old, grey and have to be carried to the slopes!

A special thanks goes to Christian (to the helmets and watch out for the dragons!), Eugenia (the car gossip), Ralf (for being my therapist and I owe you a huge amount of candy), Nela (Lästerschwester!), Simon (it's so slippery!), Fritz (the day will come that shut off my desktop effects), Marilyn (merci et à vos casques!), Matthias, Basti, Tobi, Katha, Mirjam, Tommy, Rosamunde, Andrea, Macarena, Mina, and Wiebke for always having an open ear and helping me with my work-related and non-work-related problems.

Thank you to the LSWB-Team, especially Judith, for supporting me and giving me the flexibility that I needed, throughout my studies from the very first semester 15 years ago until now. I am deeply grateful for my girls Chrissi, Steffi, Tina, and Kathi for keeping me grounded, encouraging me, and being there for me basically already my whole life.

The last but most important THANK YOU goes to my family who never lost faith in me and supported me the whole time with all my ideas I'm coming up with. I couldn't be doing what I do now without you!!!

Appendix A

Kinematic of P14 stars

PM/ Model	x (kpc)	y (kpc)	z (kpc)	v_x (km/s)	v_y (km/s)	v_z (km/s)	v_r (km/s)	v_ϕ (km/s)	v_{GRF} (km/s)	v_{ej} (km/s)	bound
SDSS (P14)	-10.6 ± 0.2	2.5 ± 0.2	1.6 ± 0.1	-480 ± 57	-513 ± 67	386 ± 53	346 ± 37	-612 ± 82	803 ± 92		
I	-8.5 ± 0.3	4.6 ± 0.5	0	-501 ± 57	-505 ± 67	390 ± 53	195 ± 19	-683 ± 91	813 ± 90	1023 ± 93	0.9%
II	-8.5 ± 0.3	4.6 ± 0.5	0	-500 ± 57	-507 ± 67	391 ± 53	193 ± 19	-685 ± 91	814 ± 90	1024 ± 93	0.20%
III	-8.5 ± 0.3	4.7 ± 0.5	0	-501 ± 57	-508 ± 67	390 ± 53	193 ± 19	-686 ± 91	814 ± 90	1024 ± 93	44.74%
USNO	-10.6 ± 0.2	2.5 ± 0.2	1.6 ± 0.1	-412 ± 120	-447 ± 120	372 ± 145	295 ± 98	-531 ± 140	728 ± 164		
I	-8.1 ± 5.7	4.7 ± 1.9	0	-437 ± 123	-434 ± 126	379 ± 140	148 ± 97	-595 ± 159	740 ± 160	943 ± 163	20.2%
II	-8.1 ± 5.7	4.7 ± 2.0	0	-436 ± 123	-436 ± 127	379 ± 141	146 ± 97	-596 ± 159	741 ± 160	944 ± 163	13.12%
III	-8.1 ± 6.2	4.7 ± 2.0	0	-437 ± 123	-436 ± 127	378 ± 141	146 ± 97	-597 ± 160	741 ± 160	945 ± 164	65.41%
PPMXL	-10.6 ± 0.2	2.5 ± 0.2	1.6 ± 0.1	-435 ± 80	-499 ± 85	423 ± 86	306 ± 61	-587 ± 101	791 ± 116		
I	-8.8 ± 0.5	4.4 ± 0.5	0	-455 ± 81	-492 ± 85	427 ± 85	180 ± 26	-646 ± 113	800 ± 114	1003 ± 117	3.7%
II	-8.8 ± 0.5	4.4 ± 0.5	0	-455 ± 81	-493 ± 85	427 ± 85	179 ± 26	-647 ± 113	800 ± 114	1004 ± 117	1.34%
III	-8.8 ± 0.5	4.4 ± 0.5	0	-455 ± 81	-494 ± 85	427 ± 85	179 ± 26	-648 ± 113	801 ± 114	1004 ± 117	50.64%
HSOY	-10.6 ± 0.2	2.5 ± 0.2	1.6 ± 0.1	-440 ± 81	-465 ± 83	362 ± 84	319 ± 62	-555 ± 99	741 ± 113		
I	-8.5 ± 0.7	4.6 ± 0.6	0	-463 ± 82	-456 ± 83	367 ± 83	182 ± 30	-624 ± 114	752 ± 111	960 ± 114	8.8%
II	-8.5 ± 0.7	4.6 ± 0.6	0	-463 ± 82	-457 ± 83	367 ± 83	180 ± 30	-625 ± 114	753 ± 111	961 ± 114	3.81%
III	-8.5 ± 0.7	4.6 ± 0.6	0	-463 ± 82	-458 ± 83	367 ± 82	180 ± 30	-626 ± 114	753 ± 111	961 ± 114	67.47%

Table A.1: SDSS J060306.77+825829.1 (#1) positions, velocity components and the probability of being bound to the Galaxy based on proper motions from different astrometric catalogues. The values of the first line are the current values, next lines are the values and the time at the last disk passage based on models I, II, and III of Irrgang et al. (2013), respectively.

PM/ Model	x (kpc)	y (kpc)	z (kpc)	v_x (km/s)	v_y (km/s)	v_z (km/s)	v_r (km/s)	v_ϕ (km/s)	v_{GRF} (km/s)	v_{ej} (km/s)	bound
this work	-12.6 ± 0.3	2.4 ± 0.2	-2.9 ± 0.2	-164 ± 85	230 ± 104	289 ± 93	205 ± 73	195 ± 114	425 ± 100		
I	46.3 ± 19.5	-18.0 ± 7.8	0	69 ± 138	-88 ± 65	-92 ± 34	103 ± 141	58 ± 42	194 ± 87	246 ± 73	92.31%
II	55.2 ± 29.3	-21.6 ± 11.1	0	28 ± 114	-65 ± 49	-81 ± 40	57 ± 113	51 ± 43	156 ± 65	221 ± 51	84.69%
III	31.5 ± 9.4	-12.0 ± 4.2	0	119 ± 150	-127 ± 81	-132 ± 30	166 ± 153	79 ± 50	258 ± 106	284 ± 97	99.93%
SDSS (P14)	-12.6 ± 0.3	2.4 ± 0.2	-2.9 ± 0.2	4 ± 54	548 ± 77	312 ± 73	100 ± 49	539 ± 81	636 ± 87		
I	37.7 ± 4.9	-29.3 ± 15.2	0	181 ± 61	-269 ± 57	-76 ± 22	306 ± 69	114 ± 22	337 ± 69	334 ± 55	23.36%
II	53.4 ± 8.0	-44.7 ± 27.4	0	133 ± 61	-187 ± 52	-48 ± 14	220 ± 72	72 ± 12	240 ± 61	269 ± 47	10.73%
III	25.4 ± 2.4	-17.8 ± 5.9	0	229 ± 64	-406 ± 73	-141 ± 38	420 ± 71	208 ± 39	491 ± 83	446 ± 74	94.40%
PPMXL	-12.6 ± 0.3	2.4 ± 0.2	-2.9 ± 0.2	0 ± 91	264 ± 122	81 ± 116	50 ± 79	259 ± 130	314 ± 118		
I	11.8 ± 21.2	-20.4 ± 27.4	0	-88 ± 135	5 ± 149	-98 ± 60	-5 ± 137	146 ± 89	230 ± 92	191 ± 92	97.84%
II	12.9 ± 24.8	-22.3 ± 33.1	0	-96 ± 126	21 ± 139	-96 ± 62	-22 ± 125	142 ± 93	222 ± 94	188 ± 89	95.62%
III	8.3 ± 15.4	-15.2 ± 15.4	0	-83 ± 141	-29 ± 167	-108 ± 56	25 ± 148	162 ± 82	251 ± 85	194 ± 101	99.97%
APOP	-12.6 ± 0.3	2.4 ± 0.2	-2.9 ± 0.2	-125 ± 108	245 ± 111	245 ± 74	169 ± 86	217 ± 129	401 ± 62		
I	48.1 ± 17.9	-24.5 ± 21.8	0	47 ± 89	-87 ± 62	-73 ± 21	87 ± 98	57 ± 32	153 ± 62	211 ± 54	98.54%
II	57.1 ± 26.2	-29.1 ± 25.6	0	29 ± 75	-71 ± 51	-64 ± 23	63 ± 84	50 ± 28	129 ± 47	200 ± 39	96.36%
III	31.1 ± 9.0	-15.6 ± 12.4	0	69 ± 93	-123 ± 72	-108 ± 23	128 ± 92	82 ± 46	206 ± 61	229 ± 65	99.99%
HSOY	-12.6 ± 0.3	2.4 ± 0.2	-2.9 ± 0.2	-1 ± 47	231 ± 61	55 ± 56	45 ± 41	226 ± 65	248 ± 61		
I	4.8 ± 10.7	-13.7 ± 9.3	0	-181 ± 75	-5 ± 95	-97 ± 43	-25 ± 63	198 ± 59	233 ± 65	131 ± 50	100%
II	4.9 ± 11.5	-14.2 ± 10.6	0	-178 ± 75	1 ± 94	-96 ± 43	-27 ± 63	195 ± 61	230 ± 66	132 ± 49	100%
III	4.1 ± 8.8	-12.1 ± 6.4	0	-185 ± 75	-20 ± 98	-102 ± 41	-14 ± 64	208 ± 51	243 ± 55	127 ± 52	100%

Table A.2: Same as Table A.1 but for SDSS J023433.42+262327.5 (#2).

PM/ Model	x (kpc)	y (kpc)	z (kpc)	v_x (km/s)	v_y (km/s)	v_z (km/s)	v_r (km/s)	v_ϕ (km/s)	v_{GRF} (km/s)	v_{ej} (km/s)	bound
this work	-5.3 ± 0.6	0.9 ± 0.2	2.5 ± 0.5	182 ± 64	182 ± 85	-125 ± 70	-150 ± 67	211 ± 79	305 ± 76		
I	-1.9 ± 2.0	-7.7 ± 5.6	0	-186 ± 69	-91 ± 120	137 ± 52	161 ± 111	147 ± 45	273 ± 94	249 ± 92	99.97%
II	-2.0 ± 2.0	-7.9 ± 6.0	0	-184 ± 69	-87 ± 117	135 ± 50	159 ± 111	142 ± 43	268 ± 92	247 ± 91	99.92%
III	-1.9 ± 2.0	-7.1 ± 4.5	0	-191 ± 68	-97 ± 123	143 ± 58	166 ± 108	153 ± 51	282 ± 99	254 ± 94	100%
SDSS (P14)	-5.3 ± 0.6	0.9 ± 0.2	2.5 ± 0.5	219 ± 51	532 ± 75	-290 ± 73	-126 ± 43	561 ± 81	647 ± 97		
I	8.8 ± 3.5	-20.4 ± 12.1	0	20 ± 31	-395 ± 96	95 ± 43	365 ± 85	151 ± 57	410 ± 99	393 ± 74	49.27%
II	11.4 ± 5.0	-27.9 ± 18.8	0	28 ± 30	-327 ± 98	69 ± 34	308 ± 91	112 ± 46	338 ± 98	343 ± 70	33.28%
III	5.6 ± 1.8	-12.9 ± 5.6	0	-21 ± 42	-511 ± 93	157 ± 60	455 ± 83	231 ± 69	538 ± 104	488 ± 88	96.28%
PPMXL	-5.3 ± 0.6	0.9 ± 0.2	2.5 ± 0.5	131 ± 70	355 ± 103	-122 ± 86	-70 ± 74	372 ± 100	413 ± 103		
I	1.7 ± 5.9	-24.0 ± 28.2	0	-95 ± 55	-33 ± 196	83 ± 44	46 ± 180	119 ± 55	224 ± 103	224 ± 86	97.80%
II	1.8 ± 6.7	-26.1 ± 34.1	0	-95 ± 54	-12 ± 184	80 ± 43	28 ± 171	114 ± 56	212 ± 95	217 ± 77	95.74%
III	1.0 ± 3.9	-18.7 ± 15.2	0	-102 ± 51	-79 ± 216	94 ± 49	88 ± 192	133 ± 56	250 ± 119	239 ± 103	99.96%
APOP	-5.3 ± 0.6	0.9 ± 0.2	2.5 ± 0.5	160 ± 74	238 ± 96	-118 ± 63	-118 ± 86	262 ± 84	335 ± 54		
I	-1.6 ± 1.2	-10.7 ± 5.9	0	-165 ± 72	-44 ± 141	121 ± 58	83 ± 155	145 ± 44	248 ± 103	224 ± 93	99.98%
II	-1.7 ± 1.2	-10.9 ± 6.2	0	-163 ± 72	-40 ± 139	120 ± 56	80 ± 156	142 ± 42	245 ± 101	224 ± 92	99.9%
III	-1.6 ± 1.2	-10.3 ± 5.4	0	-169 ± 74	-53 ± 140	125 ± 65	92 ± 153	150 ± 47	255 ± 107	228 ± 95	100%
HSOY	-5.3 ± 0.6	0.9 ± 0.2	2.5 ± 0.5	181 ± 41	401 ± 53	-199 ± 56	-111 ± 35	426 ± 57	486 ± 67		
I	5.8 ± 3.0	-27.0 ± 12.8	0	-38 ± 32	-242 ± 134	69 ± 33	228 ± 129	95 ± 37	266 ± 120	286 ± 96	98.2%
II	6.5 ± 3.8	-31.9 ± 17.0	0	-33 ± 32	-208 ± 126	59 ± 27	196 ± 123	81 ± 31	232 ± 108	265 ± 84	95.04%
III	4.1 ± 1.8	-18.3 ± 6.8	0	-61 ± 31	-303 ± 125	96 ± 42	280 ± 119	134 ± 43	330 ± 120	322 ± 102	100%

Table A.3: Same as Table A.1 but for SDSS J160620.65+042451.5 (#3).

PM/ Model	x (kpc)	y (kpc)	z (kpc)	v_x (km/s)	v_y (km/s)	v_z (km/s)	v_r (km/s)	v_ϕ (km/s)	v_{GRF} (km/s)	v_{ej} (km/s)	bound
this work	-8.9 ± 0.1	0.5 ± 0.1	0.8 ± 0.1	-5 ± 13	126 ± 25	5 ± 15	12 ± 13	125 ± 26	128 ± 23		
I	-5.9 ± 1.3	-2.9 ± 1.1	0	-202 ± 46	82 ± 19	49 ± 9	137 ± 29	170 ± 43	227 ± 37	168 ± 32	100%
II	-5.9 ± 1.3	-2.8 ± 1.1	0	-199 ± 46	82 ± 19	49 ± 9	136 ± 30	167 ± 43	224 ± 37	169 ± 32	100%
III	-5.9 ± 1.3	-2.8 ± 1.1	0	-199 ± 46	82 ± 19	49 ± 9	136 ± 30	167 ± 43	224 ± 37	169 ± 32	100%
SDSS (P14)	-8.9 ± 0.1	0.5 ± 0.1	0.8 ± 0.1	-609 ± 121	820 ± 111	-813 ± 144	654 ± 134	784 ± 99	1306 ± 213		
I	25.1 ± 3.8	-5.0 ± 1.5	0	322 ± 87	-203 ± 33	102 ± 22	355 ± 84	141 ± 25	397 ± 82	381 ± 73	0.04%
II	34.0 ± 3.7	-7.9 ± 1.6	0	247 ± 88	-152 ± 23	67 ± 12	275 ± 86	96 ± 13	301 ± 79	312 ± 69	0.02%
III	16.4 ± 1.4	-2.4 ± 0.5	0	452 ± 57	-315 ± 36	203 ± 35	493 ± 58	248 ± 33	588 ± 73	534 ± 65	0.95%
USNO	-8.9 ± 0.1	0.5 ± 0.1	0.8 ± 0.1	-637 ± 128	855 ± 128	-853 ± 156	684 ± 142	817 ± 116	1366 ± 232		
I	25.5 ± 4.0	-5.1 ± 1.6	0	318 ± 86	-199 ± 36	101 ± 24	350 ± 86	138 ± 27	390 ± 88	377 ± 75	0.03%
II	33.7 ± 5.3	-8.1 ± 1.8	0	229 ± 103	-149 ± 28	66 ± 13	259 ± 95	97 ± 21	289 ± 86	298 ± 78	0.02%
III	16.5 ± 1.5	-2.4 ± 0.6	0	451 ± 61	-312 ± 40	202 ± 37	491 ± 62	246 ± 37	585 ± 78	532 ± 69	0.68%
UCAC4	-8.9 ± 0.1	0.5 ± 0.1	0.8 ± 0.1	-25 ± 17	119 ± 24	-3 ± 11	32 ± 17	117 ± 25	124 ± 20		
I	-4.7 ± 1.2	-2.8 ± 0.9	0	-254 ± 42	62 ± 21	55 ± 10	176 ± 37	191 ± 44	269 ± 37	196 ± 40	100%
II	-4.7 ± 1.2	-2.8 ± 0.9	0	-252 ± 42	62 ± 21	54 ± 10	176 ± 37	188 ± 44	267 ± 38	197 ± 40	100%
III	-4.7 ± 1.2	-2.8 ± 0.9	0	-252 ± 41	61 ± 20	55 ± 11	176 ± 37	187 ± 43	267 ± 36	197 ± 40	100%
PPMXL	-8.9 ± 0.1	0.5 ± 0.1	0.8 ± 0.1	-653 ± 128	828 ± 112	-846 ± 149	699 ± 141	790 ± 99	1353 ± 222		
I	26.4 ± 4.0	-5.3 ± 1.7	0	310 ± 86	-191 ± 34	96 ± 23	341 ± 86	132 ± 25	378 ± 88	368 ± 75	0.03%
II	26.4 ± 4.0	-5.3 ± 1.7	0	310 ± 86	-191 ± 34	96 ± 23	341 ± 86	132 ± 25	378 ± 88	368 ± 75	0.03%
III	16.6 ± 1.4	-2.4 ± 0.6	0	455 ± 60	-308 ± 36	201 ± 35	493 ± 60	243 ± 33	586 ± 74	534 ± 67	0.67%
APOP	-8.9 ± 0.1	0.5 ± 0.1	0.8 ± 0.1	-36 ± 15	167 ± 12	-41 ± 4	45 ± 15	164 ± 13	176 ± 8		
I	-0.2 ± 0.5	-4.8 ± 0.6	0	-309 ± 15	-41 ± 17	91 ± 16	46 ± 19	307 ± 18	325 ± 20	125 ± 20	100%
II	-0.2 ± 0.6	-4.8 ± 0.6	0	-308 ± 16	-42 ± 19	89 ± 15	48 ± 19	307 ± 19	324 ± 21	125 ± 20	100%
III	-0.2 ± 0.6	-4.8 ± 0.6	0	-308 ± 16	-42 ± 19	89 ± 15	48 ± 19	307 ± 19	324 ± 21	125 ± 20	100%
UCAC5	-8.9 ± 0.1	0.5 ± 0.1	0.8 ± 0.1	12 ± 24	84 ± 35	43 ± 23	-8 ± 23	84 ± 36	104 ± 23		
I	-8.1 ± 0.8	-0.9 ± 0.9	0	-93 ± 51	79 ± 29	62 ± 18	79 ± 44	92 ± 40	146 ± 32	187 ± 41	100%
II	-8.2 ± 0.8	-0.9 ± 0.9	0	-91 ± 50	77 ± 29	62 ± 18	78 ± 43	90 ± 40	144 ± 32	188 ± 41	100%
III	-8.1 ± 0.8	-0.9 ± 0.9	0	-92 ± 50	77 ± 29	61 ± 18	79 ± 43	89 ± 40	144 ± 32	188 ± 41	100%

Table A.4: Same as Table A.1 but for SDSS J113102.87+665751.1 (#4).

PM/ Model	x (kpc)	y (kpc)	z (kpc)	v_x (km/s)	v_y (km/s)	v_z (km/s)	v_r (km/s)	v_ϕ (km/s)	v_{GRF} (km/s)	v_{ej} (km/s)	bound
SDSS (P14)	-6.4 ± 0.2	2.4 ± 0.2	0.5 ± 0.1	-632 ± 66	785 ± 50	421 ± 57	870 ± 95	507 ± 22	1094 ± 86		
I	-5.6 ± 0.2	1.5 ± 0.2	0	-643 ± 66	789 ± 51	423 ± 57	823 ± 94	595 ± 31	1103 ± 87	993 ± 95	0.0%
II	-5.6 ± 0.2	1.5 ± 0.2	0	-642 ± 66	787 ± 51	423 ± 57	823 ± 94	593 ± 31	1102 ± 87	992 ± 96	0.0%
III	-5.6 ± 0.2	1.5 ± 0.2	0	-642 ± 66	786 ± 51	423 ± 57	823 ± 94	593 ± 31	1101 ± 87	991 ± 96	0.04%
USNO	-6.4 ± 0.2	2.4 ± 0.2	0.5 ± 0.1	-721 ± 138	845 ± 99	497 ± 86	974 ± 174	531 ± 43	1218 ± 183		
I	-5.7 ± 0.2	1.6 ± 0.2	0	-730 ± 137	847 ± 99	499 ± 86	932 ± 173	616 ± 49	1226 ± 183	1122 ± 191	0.02%
II	-5.7 ± 0.2	1.6 ± 0.2	0	-730 ± 137	846 ± 99	499 ± 86	931 ± 173	615 ± 49	1225 ± 183	1121 ± 191	0.01%
III	-5.7 ± 0.2	1.6 ± 0.2	0	-730 ± 137	845 ± 99	499 ± 86	931 ± 172	614 ± 49	1224 ± 182	1121 ± 191	1.13%
PPMXL	-6.4 ± 0.2	2.4 ± 0.2	0.5 ± 0.1	-674 ± 84	808 ± 65	485 ± 86	917 ± 114	513 ± 32	1161 ± 109		
I	-5.7 ± 0.3	1.6 ± 0.2	0	-683 ± 84	811 ± 66	487 ± 85	875 ± 112	595 ± 48	1170 ± 109	1066 ± 118	0.0%
II	-5.7 ± 0.3	1.6 ± 0.2	0	-683 ± 84	809 ± 66	487 ± 85	875 ± 112	594 ± 48	1168 ± 110	1065 ± 118	0.00%
III	-5.7 ± 0.3	1.6 ± 0.2	0	-683 ± 84	808 ± 66	487 ± 85	875 ± 112	593 ± 48	1168 ± 110	1065 ± 118	0.03%

Table A.5: Same as Table A.1 but for SDSS J185018.09+191236.1 (#5).

PM/ Model	x (kpc)	y (kpc)	z (kpc)	v_x (km/s)	v_y (km/s)	v_z (km/s)	v_r (km/s)	v_ϕ (km/s)	v_{GRF} (km/s)	v_{ej} (km/s)	bound
this work	-10.6 ± 0.4	0.6 ± 0.1	-2.1 ± 0.4	-44 ± 25	132 ± 40	-17 ± 26	36 ± 25	135 ± 40	145 ± 38		
I	-4.4 ± 3.0	-4.5 ± 1.3	0	-254 ± 65	27 ± 75	-98 ± 30	123 ± 73	223 ± 69	286 ± 61	180 ± 60	100%
II	-4.5 ± 3.0	-4.4 ± 1.3	0	-251 ± 66	27.5 ± 75	-97 ± 29	123 ± 73	221 ± 70	283 ± 62	180 ± 60	100%
III	-4.4 ± 3.0	-4.4 ± 1.3	0	-253 ± 64	26 ± 72	-98 ± 32	124 ± 72	221 ± 68	285 ± 61	181 ± 61	100%
SDSS (P14)	-10.6 ± 0.4	-0.6 ± 0.1	-2.1 ± 0.4	37 ± 60	859 ± 137	-325 ± 79	-89 ± 64	855 ± 136	923 ± 148		
I	-10.7 ± 0.6	-6.2 ± 1.6	0	7 ± 64	849 ± 137	-331 ± 78	-436 ± 119	729 ± 93	916 ± 147	741 ± 154	0.82%
II	-10.7 ± 0.6	-6.2 ± 1.6	0	8 ± 64	848 ± 137	-331 ± 79	-435 ± 119	728 ± 93	914 ± 148	740 ± 155	0.31%
III	-10.7 ± 0.6	-6.2 ± 1.6	0	7 ± 64	847 ± 137	-331 ± 78	-434 ± 118	728 ± 93	913 ± 147	739 ± 154	19.78%
USNO	-10.6 ± 0.4	-0.6 ± 0.1	-2.1 ± 0.4	48 ± 73	1166 ± 196	-431 ± 109	-119 ± 80	1161 ± 193	1248 ± 213		
I	-10.8 ± 0.6	-6.4 ± 1.6	0	26 ± 77	1159 ± 196	-436 ± 108	617 ± 165	981 ± 135	1243 ± 213	1066 ± 221	0.03%
II	-10.8 ± 0.6	-6.4 ± 1.6	0	27 ± 77	1158 ± 195	-436 ± 108	-616 ± 165	980 ± 135	1241 ± 213	1064 ± 220	0.01%
III	-10.8 ± 0.6	-6.4 ± 1.6	0	26 ± 77	1156 ± 195	-435 ± 108	-614 ± 165	979 ± 135	1240 ± 213	1063 ± 220	1.14%
PPMXL	-10.6 ± 0.4	-0.6 ± 0.1	-2.1 ± 0.4	-36 ± 87	1175 ± 208	-343 ± 107	-35 ± 88	1176 ± 208	1232 ± 217		
I	-10.1 ± 1.4	-8.3 ± 3.9	0	-63 ± 92	1165 ± 207	-350 ± 106	-675 ± 203	946 ± 143	1225 ± 216	1053 ± 225	0.04%
II	-10.1 ± 1.3	-8.3 ± 3.8	0	-62 ± 92	1164 ± 207	-350 ± 106	-674 ± 203	945 ± 142	1223 ± 216	1051 ± 225	0.02%
III	-10.1 ± 1.5	-8.3 ± 4.1	0	-63 ± 92	1163 ± 207	-349 ± 106	-673 ± 203	945 ± 143	1222 ± 216	1050 ± 225	1.47%
APOP	-10.6 ± 0.4	-0.6 ± 0.1	-2.1 ± 0.4	-3 ± 29	135 ± 44	-62 ± 32	-4 ± 29	135 ± 44	155 ± 43		
I	-8.3 ± 2.2	-3.8 ± 1.0	0	-147 ± 76	96 ± 57	-100 ± 21	83 ± 66	161 ± 52	219 ± 48	168 ± 51	100%
II	-8.3 ± 2.2	-3.7 ± 1.0	0	-144 ± 76	96 ± 57	-100 ± 21	82 ± 66	158 ± 52	217 ± 47	169 ± 51	100%
III	-8.3 ± 2.2	-3.7 ± 1.0	0	-148 ± 75	94 ± 57	-100 ± 22	85 ± 66	159 ± 52	218 ± 48	169 ± 52	100%

Table A.6: Same as Table A.1 but for SDSS J035429.27-061354.1 (#6).

PM/ Model	x (kpc)	y (kpc)	z (kpc)	v_x (km/s)	v_y (km/s)	v_z (km/s)	v_r (km/s)	v_ϕ (km/s)	v_{GRF} (km/s)	v_{ej} (km/s)	bound
SDSS (P14)	-11.4 ± 0.5	-0.3 ± 0.1	0.6 ± 0.1	-87 ± 17	783 ± 103	-114 ± 44	67 ± 12	785 ± 104	797 ± 106		
I	59.4 ± 59.2	-129.3 ± 143.8	0	-21 ± 143	147 ± 342	8 ± 7	-137 ± 355	86 ± 82	346 ± 198	369 ± 163	2.44%
II	57.9 ± 72.6	-157.7 ± 159.9	0	-110 ± 70	355 ± 262	7 ± 6	-360 ± 254	92 ± 97	402 ± 223	420 ± 186	0.89%
III	31.4 ± 21.4	-33.5 ± 59.6	0	249 ± 121	-377 ± 203	33 ± 20	406 ± 213	207 ± 87	496 ± 127	457 ± 94	48.02%
USNO	-11.4 ± 0.5	-0.3 ± 0.1	0.6 ± 0.1	-82 ± 17	750 ± 122	-105 ± 58	62 ± 13	752 ± 122	764 ± 121		
I	27.3 ± 46.1	-87.1 ± 128.7	0	-40 ± 160	367 ± 438	19 ± 19	-319 ± 429	193 ± 174	543 ± 243	520 ± 208	6.75%
II	24.6 ± 51.6	-101.2 ± 140.2	0	-107 ± 92	537 ± 325	15 ± 15	-490 ± 308	206 ± 190	595 ± 246	568 ± 208	2.92%
III	28.0 ± 27.2	-40.0 ± 81.9	0	203 ± 181	-225 ± 400	43 ± 34	255 ± 391	230 ± 116	514 ± 153	466 ± 124	60.53%
PPMXL	-11.4 ± 0.5	-0.3 ± 0.1	0.6 ± 0.1	-90 ± 23	760 ± 121	-138 ± 82	70 ± 19	762 ± 121	782 ± 125		
I	19.4 ± 45.3	-72.0 ± 117.8	0	-64 ± 137	431 ± 383	24 ± 24	-338 ± 356	261 ± 214	556 ± 216	504 ± 174	5.45%
II	15.5 ± 47.0	-77.5 ± 122.6	0	-111 ± 74	554 ± 268	23 ± 24	-456 ± 249	279 ± 222	595 ± 208	537 ± 171	2.31%
III	24.8 ± 28.1	-37.1 ± 76.8	0	185 ± 198	-170 ± 438	49 ± 38	213 ± 404	257 ± 140	524 ± 154	466 ± 117	54.96%
HSOY	-11.4 ± 0.5	-0.3 ± 0.1	0.6 ± 0.1	-86 ± 16	713 ± 90	-144 ± 45	68 ± 12	715 ± 91	734 ± 95		
I	48.3 ± 25.3	-45.3 ± 51.4	0	167 ± 110	-220 ± 127	19 ± 12	261 ± 157	101 ± 43	306 ± 108	317 ± 74	6.42%
II	80.9 ± 47.6	-96.1 ± 87.0	0	42 ± 115	-60 ± 154	9 ± 5	70 ± 183	52 ± 31	179 ± 102	238 ± 69	2.49%
III	23.7 ± 6.4	-12.6 ± 13.5	0	308 ± 66	-432 ± 73	56 ± 24	457 ± 75	268 ± 70	536 ± 89	470 ± 67	72.14%

Table A.7: Same as Table A.1 but for SDSS J064337.13+291410.0 (#7).

PM/ Model	x (kpc)	y (kpc)	z (kpc)	v_x (km/s)	v_y (km/s)	v_z (km/s)	v_r (km/s)	v_ϕ (km/s)	v_{GRF} (km/s)	v_{ej} (km/s)	bound
SDSS (P14)	-7.0 ± 0.2	2.0 ± 0.4	-0.6 ± 0.1	-211 ± 50	565 ± 59	482 ± 93	358 ± 88	482 ± 27	774 ± 111		
I	22.7 ± 4.3	-8.8 ± 2.1	0	303 ± 54	-260 ± 42	-106 ± 27	376 ± 63	136 ± 25	414 ± 70	402 ± 58	8.89%
II	31.6 ± 5.2	-12.8 ± 2.8	0	249 ± 62	-199 ± 35	-69 ± 17	305 ± 68	94 ± 16	327 ± 68	338 ± 56	4.08%
III	14.3 ± 1.8	-5.5 ± 0.8	0	383 ± 43	-389 ± 49	-208 ± 46	498 ± 58	224 ± 30	585 ± 74	541 ± 67	67.45%
USNO	-7.0 ± 0.2	2.0 ± 0.4	-0.6 ± 0.1	-242 ± 84	579 ± 77	465 ± 116	392 ± 118	488 ± 40	787 ± 135		
I	28.3 ± 13.6	-13.0 ± 9.4	0	278 ± 74	-244 ± 58	-90 ± 40	351 ± 87	115 ± 37	383 ± 92	384 ± 71	10.85%
II	41.3 ± 23.6	-20.1 ± 16.3	0	215 ± 84	-180 ± 56	-59 ± 29	270 ± 96	79 ± 28	291 ± 91	317 ± 66	5.60%
III	16.2 ± 4.7	-7.0 ± 3.1	0	374 ± 60	-373 ± 59	-180 ± 64	488 ± 74	200 ± 46	561 ± 90	526 ± 78	61.85%
PPMXL	-7.0 ± 0.2	2.0 ± 0.4	-0.6 ± 0.1	-205 ± 66	528 ± 62	378 ± 91	342 ± 98	449 ± 31	685 ± 106		
I	31.8 ± 13.5	-16.0 ± 9.4	0	257 ± 82	-231 ± 62	-76 ± 35	331 ± 97	98 ± 33	356 ± 99	367 ± 77	31.02%
II	46.2 ± 22.4	-24.4 ± 15.6	0	192 ± 87	-167 ± 56	-49 ± 23	246 ± 100	67 ± 24	265 ± 93	301 ± 68	18.36%
III	18.0 ± 5.1	-8.7 ± 3.5	0	350 ± 71	-353 ± 68	-151 ± 58	466 ± 91	170 ± 43	521 ± 104	498 ± 92	89.73%
HSOY	-7.0 ± 0.2	2.0 ± 0.4	-0.6 ± 0.1	-140 ± 37	470 ± 42	337 ± 66	264 ± 67	412 ± 19	597 ± 76		
I	27.1 ± 6.3	-13.7 ± 3.7	0	256 ± 70	-242 ± 56	-84 ± 28	337 ± 87	102 ± 24	363 ± 90	370 ± 75	67.13%
II	37.0 ± 7.5	-19.1 ± 4.7	0	207 ± 70	-186 ± 44	-57 ± 16	269 ± 81	72 ± 15	286 ± 78	313 ± 63	47.11%
III	17.3 ± 3.0	-8.8 ± 1.7	0	307 ± 66	-335 ± 67	-146 ± 47	426 ± 90	159 ± 29	479 ± 101	458 ± 93	99.71%

Table A.8: Same as Table A.1 but for SDSS J202446.41+121813.4 (#8).

PM/ Model	x (kpc)	y (kpc)	z (kpc)	v_x (km/s)	v_y (km/s)	v_z (km/s)	v_r (km/s)	v_ϕ (km/s)	v_{GRF} (km/s)	v_{ej} (km/s)	bound
this work	-10.3 ± 0.3	2.4 ± 0.4	-1.3 ± 0.2	92 ± 42	205 ± 35	-105 ± 52	-45 ± 35	220 ± 41	255 ± 43		
I	-10.9 ± 1.1	-0.7 ± 2.1	0	20 ± 65	206 ± 34	-118 ± 46	-36 ± 50	209 ± 30	251 ± 34	138 ± 50	100%
II	-10.9 ± 1.1	-0.7 ± 2.1	0	21 ± 64	205 ± 34	-118 ± 46	-37 ± 50	207 ± 30	250 ± 34	139 ± 49	100%
III	-10.8 ± 1.1	-0.7 ± 2.1	0	19 ± 66	204 ± 34	-117 ± 46	-35 ± 50	207 ± 30	249 ± 34	138 ± 50	100%
SDSS (P14)	-10.3 ± 0.3	2.4 ± 0.4	-1.3 ± 0.2	134 ± 42	-211 ± 86	-901 ± 173	-180 ± 52	-175 ± 78	937 ± 187		
I	-10.5 ± 0.4	2.7 ± 0.5	0	127 ± 42	-210 ± 86	-903 ± 173	-177 ± 54	-171 ± 76	937 ± 187	1008 ± 190	3.29%
II	-10.5 ± 0.4	2.7 ± 0.5	0	127 ± 42	-211 ± 86	-903 ± 173	-178 ± 54	-172 ± 76	938 ± 187	1008 ± 190	1.88%
III	-10.5 ± 0.4	2.7 ± 0.5	0	127 ± 42	-212 ± 86	-902 ± 173	-178 ± 54	-173 ± 76	938 ± 187	1008 ± 190	22.56%
USNO	-10.3 ± 0.3	2.4 ± 0.4	-1.3 ± 0.2	76 ± 32	-197 ± 103	-792 ± 217	-120 ± 53	-174 ± 92	821 ± 236		
I	-10.4 ± 0.4	2.7 ± 0.6	0	67 ± 33	-194 ± 103	-793 ± 217	-116 ± 59	-171 ± 89	821 ± 235	901 ± 238	16.99%
II	-10.4 ± 0.4	2.7 ± 0.6	0	67 ± 34	-196 ± 103	-793 ± 217	-116 ± 59	-172 ± 90	822 ± 236	901 ± 238	12.27%
III	-10.4 ± 0.4	2.7 ± 0.6	0	67 ± 33	-197 ± 103	-793 ± 217	-116 ± 59	-173 ± 90	822 ± 236	902 ± 238	48.01%
PPMXL	-10.3 ± 0.3	2.4 ± 0.4	-1.3 ± 0.2	108 ± 68	-205 ± 97	-849 ± 175	-153 ± 67	-174 ± 96	884 ± 190		
I	-10.5 ± 0.4	2.7 ± 0.6	0	100 ± 68	-201 ± 97	-850 ± 174	-150 ± 67	-169 ± 94	884 ± 190	958 ± 193	5.98%
II	-10.5 ± 0.4	2.7 ± 0.6	0	100 ± 68	-203 ± 97	-850 ± 175	-150 ± 67	-171 ± 94	884 ± 190	959 ± 193	3.62%
III	-10.5 ± 0.4	2.7 ± 0.6	0	100 ± 68	-203 ± 97	-850 ± 174	-150 ± 67	-172 ± 94	885 ± 190	959 ± 193	32.70%
HSOY	-10.3 ± 0.3	2.4 ± 0.4	-1.3 ± 0.2	137 ± 36	-143 ± 72	-785 ± 150	-167 ± 45	-108 ± 64	811 ± 161		
I	-10.5 ± 0.4	2.6 ± 0.5	0	128 ± 37	-141 ± 72	-786 ± 150	-161 ± 47	-105 ± 62	811 ± 161	874 ± 164	9.03%
II	-10.5 ± 0.4	2.6 ± 0.5	0	129 ± 37	-143 ± 72	-786 ± 150	-161 ± 47	-106 ± 62	811 ± 161	874 ± 164	5.43%
III	-10.5 ± 0.4	2.6 ± 0.5	0	128 ± 37	-143 ± 72	-786 ± 150	-161 ± 47	-107 ± 62	811 ± 161	875 ± 164	46.08%

Table A.9: Same as Table A.1 but for SDSS J011933.45+384913.0 (#9).

PM/ Model	x (kpc)	y (kpc)	z (kpc)	v_x (km/s)	v_y (km/s)	v_z (km/s)	v_r (km/s)	v_ϕ (km/s)	v_{GRF} (km/s)	v_{ej} (km/s)	bound
SDSS (P14)	-5.4 ± 0.6	1.8 ± 0.3	1.5 ± 0.3	648 ± 120	-252 ± 103	-706 ± 138	-696 ± 146	-18 ± 45	994 ± 197		
I	3.4 ± 0.3	-0.7 ± 0.2	0	-130 ± 45	-24 ± 68	581 ± 48	-121 ± 58	46 ± 64	601 ± 48	625 ± 67	3.45%
II	3.3 ± 0.3	-0.6 ± 0.2	0	-88 ± 35	-50 ± 58	562 ± 44	-75 ± 46	64 ± 53	575 ± 40	593 ± 58	1.98%
III	3.6 ± 0.2	-0.7 ± 0.1	0	-242 ± 55	51 ± 63	647 ± 52	-247 ± 65	-5 ± 57	697 ± 66	735 ± 76	20.75%
USNO	-5.4 ± 0.5	1.8 ± 0.3	1.5 ± 0.3	577 ± 107	-169 ± 104	-661 ± 153	-602 ± 126	35 ± 69	900 ± 186		
I	3.2 ± 0.7	-0.7 ± 0.3	0	-143 ± 68	-22 ± 109	577 ± 48	-128 ± 86	47 ± 107	608 ± 48	630 ± 75	7.32%
II	3.0 ± 0.7	-0.6 ± 0.4	0	-109 ± 60	-32 ± 113	558 ± 49	-89 ± 75	48 ± 116	584 ± 44	605 ± 76	4.05%
III	3.4 ± 0.5	-0.8 ± 0.3	0	-246 ± 68	37 ± 105	641 ± 56	-244 ± 85	18 ± 104	698 ± 67	728 ± 81	35.6%
PPMXL	-5.4 ± 0.5	1.8 ± 0.3	1.5 ± 0.3	605 ± 122	-210 ± 118	-669 ± 150	-641 ± 149	8 ± 70	932 ± 201		
I	3.2 ± 0.6	-0.7 ± 0.3	0	-137 ± 61	-32 ± 101	576 ± 48	-121 ± 79	57 ± 98	604 ± 49	623 ± 74	6.23%
II	3.1 ± 0.6	-0.7 ± 0.3	0	-104 ± 54	-52 ± 100	561 ± 55	-83 ± 76	69 ± 94	584 ± 47	598 ± 76	4.09%
III	3.4 ± 0.5	-0.8 ± 0.3	0	-245 ± 66	38 ± 99	639 ± 56	-243 ± 83	16 ± 97	695 ± 69	725 ± 83	31.42%
HSOY	-5.4 ± 0.5	1.8 ± 0.3	1.5 ± 0.3	556 ± 102	-202 ± 90	-576 ± 112	-593 ± 125	-2 ± 37	828 ± 165		
I	3.0 ± 0.3	-0.7 ± 0.1	0	-155 ± 44	-11 ± 61	585 ± 40	-147 ± 57	44 ± 56	609 ± 45	633 ± 60	12.57%
II	2.9 ± 0.3	-0.7 ± 0.2	0	-115 ± 36	-45 ± 66	565 ± 52	-98 ± 53	68 ± 62	584 ± 45	598 ± 67	7.82%
III	3.1 ± 0.2	-0.7 ± 0.1	0	-265 ± 61	65 ± 68	637 ± 53	-272 ± 74	-2 ± 59	697 ± 71	733 ± 81	51.76%

Table A.10: Same as Table A.1 but for SDSS J172630.60+075544.0 (#10).

PM/ Model	x (kpc)	y (kpc)	z (kpc)	v_x (km/s)	v_y (km/s)	v_z (km/s)	v_r (km/s)	v_ϕ (km/s)	v_{GRF} (km/s)	v_{ej} (km/s)	bound
SDSS (P14)	-11.7 ± 0.3	-1.3 ± 0.1	1.1 ± 0.1	-120 ± 24	621 ± 56	335 ± 53	48 ± 20	630 ± 58	717 ± 64		
I	-11.2 ± 0.3	-3.4 ± 0.4	0	-135 ± 25	620 ± 56	337 ± 53	-51 ± 15	632 ± 58	720 ± 64	525 ± 64	1.39%
II	-11.2 ± 0.3	-3.4 ± 0.4	0	-135 ± 25	618 ± 56	337 ± 53	-51 ± 15	631 ± 58	719 ± 64	524 ± 64	0.17%
III	-11.2 ± 0.3	-3.4 ± 0.4	0	-136 ± 25	617 ± 56	337 ± 53	-50 ± 15	630 ± 58	718 ± 64	523 ± 64	85.58%
USNO	-11.7 ± 0.3	-1.3 ± 0.1	1.1 ± 0.1	-62 ± 81	457 ± 96	306 ± 174	9 ± 73	461 ± 103	584 ± 104		
I	-9.3 ± 17.2	-5.5 ± 18.3	0	-80 ± 91	443 ± 102	317 ± 162	-81 ± 79	443 ± 111	580 ± 111	424 ± 123	50.85%
II	-9.5 ± 16.7	-5.4 ± 17.9	0	-81 ± 90	444 ± 98	317 ± 162	-82 ± 79	443 ± 110	580 ± 109	423 ± 123	34.59%
III	-8.9 ± 14.9	-5.5 ± 14.6	0	-77 ± 97	433 ± 125	314 ± 164	-74 ± 87	438 ± 115	575 ± 116	421 ± 125	96.53%
PPMXL	-11.7 ± 0.3	-1.3 ± 0.1	1.1 ± 0.1	-47 ± 43	453 ± 87	346 ± 91	-5.1 ± 37	456 ± 90	580 ± 96		
I	-11.4 ± 0.5	-2.9 ± 0.8	0	-63 ± 46	453 ± 87	348 ± 90	-52 ± 21	455 ± 91	582 ± 96	424 ± 95	51.73%
II	-11.4 ± 0.4	-2.9 ± 0.6	0	-63 ± 46	451 ± 87	348 ± 90	-52 ± 21	454 ± 91	581 ± 96	423 ± 96	34.62%
III	-11.4 ± 0.4	-2.9 ± 0.6	0	-63 ± 46	450 ± 87	348 ± 91	-51 ± 21	453 ± 91	580 ± 96	422 ± 96	98.00%
HSOY	-11.7 ± 0.3	-1.3 ± 0.1	1.1 ± 0.1	-123 ± 22	578 ± 51	272 ± 48	56 ± 18	589 ± 53	652 ± 57		
I	-11.1 ± 0.3	-3.7 ± 0.5	0	-142 ± 24	576 ± 51	275 ± 47	-49 ± 16	591 ± 53	655 ± 57	453 ± 58	11.04%
II	-11.1 ± 0.3	-3.7 ± 0.5	0	-142 ± 24	574 ± 51	275 ± 47	-48 ± 16	590 ± 53	654 ± 57	452 ± 58	2.24%
III	-11.1 ± 0.3	-3.7 ± 0.5	0	-143 ± 24	573 ± 51	274 ± 47	-47.1 ± 15.8	589 ± 53	653 ± 57	452 ± 58	98.56%

Table A.11: Same as Table A.1 but for SDSS J073542.35+164941.4 (#11).

PM/ Model	x (kpc)	y (kpc)	z (kpc)	v_x (km/s)	v_y (km/s)	v_z (km/s)	v_r (km/s)	v_ϕ (km/s)	$v_{\rm GRF}$ (km/s)	$v_{\rm ej}$ (km/s)	bound
this work	-10.9 ± 0.5	1.4 ± 0.3	-1.2 ± 0.2	-19 ± 28	343 ± 43	336 ± 68	63 ± 31	338 ± 43	483 ± 70		
I	23.0 ± 2.4	-7.4 ± 1.0	0	222 ± 63	-228 ± 45	-151 ± 34	282 ± 68	150 ± 29	354 ± 76	331 ± 67	91.70%
II	26.2 ± 2.7	-8.8 ± 1.0	0	206 ± 62	-200 ± 34	-123 ± 20	260 ± 64	125 ± 20	315 ± 62	305 ± 57	81.06%
III	18.1 ± 1.3	-5.6 ± 0.5	0	223 ± 66	-273 ± 48	-204 ± 44	295 ± 70	196 ± 33	410 ± 82	362 ± 80	99.98%
SDSS (P14)	-10.9 ± 0.5	1.4 ± 0.3	-1.2 ± 0.2	-137 ± 44	372 ± 46	618 ± 113	185 ± 50	350 ± 44	736 ± 117		
I	20.2 ± 1.7	-4.1 ± 0.5	0	306 ± 45	-216 ± 29	-206 ± 34	344 ± 46	151 ± 23	428 ± 58	409 ± 52	11.00%
II	23.9 ± 1.7	-5.2 ± 0.5	0	274 ± 49	-182 ± 22	-156 ± 22	307 ± 49	121 ± 16	365 ± 52	360 ± 48	5.55%
III	16.5 ± 0.7	-3.3 ± 0.2	0	369.1 ± 45	-281 ± 35	-328 ± 50	417 ± 48	204 ± 28	569 ± 69	532 ± 67	68.44%
USNO	-10.9 ± 0.5	1.4 ± 0.3	-1.2 ± 0.2	-9 ± 17	378 ± 78	358 ± 114	58 ± 29	373 ± 76	522 ± 134		
I	21.5 ± 3.8	-7.7 ± 1.5	0	181 ± 105	-227 ± 53	-144 ± 38	249 ± 101	159 ± 34	334 ± 94	302 ± 89	70.51%
II	24.3 ± 4.8	-9.2 ± 1.5	0	157 ± 105	-196 ± 39	-117.5 ± 21	219 ± 96	133 ± 25	289 ± 76	271 ± 77	59.84%
III	16.9 ± 2.0	-5.5 ± 1.0	0	212 ± 103	-296 ± 69	-214 ± 64	293 ± 104	221 ± 47	428 ± 119	369 ± 115	96.61%
PPMXL	-10.9 ± 0.5	1.4 ± 0.3	-1.2 ± 0.2	-73 ± 52	307 ± 70	409 ± 99	112 ± 51	294 ± 73	523 ± 102		
I	24.7 ± 4.0	-6.6 ± 1.2	0	236 ± 82	-187 ± 55	-159 ± 38	278 ± 85	121 ± 39	345 ± 89	341 ± 77	74.45%
II	28.7 ± 4.9	-7.9 ± 1.3	0	208 ± 79	-159 ± 45	-127 ± 20	244 ± 80	99 ± 30	297 ± 73	306 ± 64	61.11%
III	18.9 ± 2.0	-4.8 ± 0.7	0	269 ± 87	-239 ± 67	-234 ± 59	322 ± 90	167 ± 52	435 ± 106	407 ± 100	98.87%
HSOY	-10.9 ± 0.5	1.4 ± 0.3	-1.2 ± 0.2	-101 ± 37	314 ± 37	475 ± 87	141 ± 41	298 ± 36	581 ± 88		
I	22.8 ± 2.1	-5.3 ± 0.6	0	287 ± 54	-199 ± 32	-186 ± 35	325 ± 57	130 ± 22	397 ± 66	388 ± 60	54.46%
II	26.9 ± 2.2	-6.5 ± 0.6	0	257 ± 54	-170 ± 24	-143 ± 20	290 ± 55	105 ± 16	341 ± 56	344 ± 51	36.42%
III	18.4 ± 0.9	-4.2 ± 0.3	0	330 ± 63	-250 ± 38	-277 ± 54	378 ± 66	171 ± 27	500 ± 84	473 ± 83	98.51%

Table A.12: Same as Table A.1 but for SDSS J025450.18+333158.4 (#12).

PM/ Model	x (kpc)	y (kpc)	z (kpc)	v_x (km/s)	v_y (km/s)	v_z (km/s)	v_r (km/s)	v_ϕ (km/s)	$v_{\rm GRF}$ (km/s)	$v_{\rm ej}$ (km/s)	bound
this work	-8.0 ± 0.1	0.4 ± 0.1	2.8 ± 0.5	39 ± 36	178 ± 39	16 ± 7	-30 ± 36	180 ± 38	187 ± 36		
I	-5.0 ± 1.1	-5.6 ± 1.6	0	-189 ± 32	80 ± 24	114 ± 20	65 ± 49	190 ± 32	237 ± 30	149 ± 39	100%
II	-5.0 ± 1.1	-5.6 ± 1.6	0	-187 ± 33	80 ± 24	114 ± 19	64 ± 50	188 ± 33	236 ± 30	150 ± 39	100%
III	-5.0 ± 1.1	-5.6 ± 1.6	0	-185 ± 30	79 ± 23	113 ± 20	64 ± 48	186 ± 32	233 ± 29	149 ± 39	100%
SDSS (P14)	-8.0 ± 0.1	0.4 ± 0.1	2.8 ± 0.5	593 ± 112	387 ± 48	-99 ± 21	-573 ± 107	418 ± 54	718 ± 110		
I	-70.1 ± 26	-100.2 ± 27.5	0	-104 ± 53	-105 ± 84	9 ± 2	146 ± 99	25 ± 10	160 ± 80	246 ± 52	16.90%
II	-102.0 ± 52.7	-146.4 ± 66.2	0	-25 ± 28	0 ± 57	7 ± 4	14 ± 62	20 ± 14	59 ± 34	185 ± 17	8.91%
III	-38.4 ± 10.9	-48.1 ± 8.3	0	-273 ± 78	-259 ± 80	22 ± 4	373 ± 109	51 ± 11	379 ± 106	410 ± 94	79.36%
USNO	-8.0 ± 0.1	0.4 ± 0.1	2.8 ± 0.5	497 ± 125	470 ± 111	-96 ± 22	-473 ± 124	495 ± 111	702 ± 110		
I	-73.7 ± 39.7	-149.7 ± 84.4	0	-54 ± 49	-38 ± 94	8 ± 3	58 ± 106	23 ± 13	106 ± 66	208 ± 42	20.65%
II	-96.4 ± 65.8	-191.6 ± 128	0	1 ± 25	60 ± 64	7 ± 5	-54 ± 68	22 ± 17	77 ± 49	185 ± 28	11.14%
III	-37.4 ± 15.8	-72.9 ± 30.3	0	-187 ± 88	-235 ± 110	18 ± 4	302 ± 130	46 ± 12	309 ± 123	352 ± 103	82.90%
PPMXL	-8.0 ± 0.1	0.4 ± 0.1	2.8 ± 0.5	468 ± 105	339 ± 68	-73 ± 20	-450 ± 102	363 ± 71	587 ± 102		
I	-98.4 ± 68.7	-112.1 ± 70.0	0	-10 ± 48	26 ± 70	12 ± 7	-14 ± 82	26 ± 18	79 ± 44	192 ± 24	60.98%
II	-116.1 ± 98.8	-131.1 ± 105.3	0	37 ± 31	80 ± 40	12 ± 8	-87 ± 43	25 ± 19	95 ± 40	192 ± 26	45.58%
III	-54.6 ± 25.7	-60.4 ± 21.8	0	-138 ± 87	-99 ± 107	18.5 ± 4.3	166 ± 137	38 ± 14	185 ± 118	258 ± 93	97.55%
APOP	-8.0 ± 0.1	0.4 ± 0.1	2.8 ± 0.5	-97 ± 66	125 ± 63	44 ± 16	102 ± 65	119 ± 65	182 ± 49		
I	-2.4 ± 1.3	-2.9 ± 1.9	0	-318 ± 71	49 ± 37	165 ± 46	158 ± 122	236 ± 119	365 ± 78	265 ± 116	100%
II	-2.4 ± 1.3	-2.8 ± 1.9	0	-321 ± 75	47 ± 39	164 ± 46	160 ± 125	236 ± 123	367 ± 81	267 ± 118	100%
III	-2.5 ± 1.3	-2.8 ± 1.9	0	-310 ± 68	52 ± 35	168 ± 48	160 ± 118	227 ± 117	360 ± 77	266 ± 115	100%
HSOY	-8.0 ± 0.1	0.4 ± 0.1	2.8 ± 0.5	461 ± 87	262 ± 33	-61 ± 14	-447 ± 84	285 ± 34	536 ± 79		
I	-117.4 ± 85.9	-93.7 ± 58.8	0	9 ± 38	38 ± 44	12 ± 6	-33 ± 55	23 ± 17	64 ± 32	186 ± 18	82.29%
II	-135.8 ± 118	-109.0 ± 86.3	0	53 ± 27	74 ± 26	12 ± 7	-90 ± 28	23 ± 17	95 ± 29	194 ± 24	67.18%
III	-65.6 ± 34.3	-49.9 ± 18.6	0	-97 ± 63	-32 ± 59	18 ± 4	95 ± 87	33 ± 15	114 ± 72	211 ± 53	99.89%

Table A.13: Same as Table A.1 but for SDSS J134427.80+282502.7 (#13).

PM/ Model	x (kpc)	y (kpc)	z (kpc)	v_x (km/s)	v_y (km/s)	v_z (km/s)	v_r (km/s)	v_ϕ (km/s)	$v_{\rm GRF}$ (km/s)	$v_{\rm ej}$ (km/s)	bound
this work	-7.9 ± 0.1	3.2 ± 0.6	-3.3 ± 0.6	32 ± 61	174 ± 40	70 ± 40	35 ± 58	174 ± 45	202 ± 51		
I	0.7 ± 3.0	-6.8 ± 3.8	0	-231 ± 58	-17 ± 48	-165 ± 37	26 ± 76	224 ± 53	290 ± 60	191 ± 44	100%
II	0.7 ± 3.0	-6.8 ± 3.9	0	-231 ± 60	-18 ± 46	-164 ± 38	26 ± 77	223 ± 55	290 ± 62	191 ± 44	100%
III	0.6 ± 2.9	-6.7 ± 3.3	0	-226 ± 54	-17 ± 52	-166 ± 37	30 ± 76	220 ± 48	288 ± 56	191 ± 44	100%
SDSS (P14)	-7.9 ± 0.1	3.2 ± 0.6	-3.3 ± 0.6	595 ± 137	-417 ± 126	-411 ± 107	-710 ± 172	-156 ± 67	840 ± 194		
I	-12.5 ± 1.2	6.4 ± 1.3	0	561 ± 142	-401 ± 126	-422 ± 106	-684 ± 177	-97 ± 44	813 ± 198	875 ± 186	11.31%
II	-12.5 ± 1.2	6.4 ± 1.3	0	561 ± 142	-403 ± 126	-422 ± 106	-686 ± 177	-98 ± 44	815 ± 198	876 ± 187	7.44%
III	-12.5 ± 1.2	6.4 ± 1.3	0	560 ± 141	-403 ± 126	-422 ± 106	-685 ± 177	-98 ± 44	814 ± 198	876 ± 186	43.28%
USNO	-7.9 ± 0.1	3.2 ± 0.6	-3.3 ± 0.6	683 ± 280	-524 ± 298	-500 ± 256	-832 ± 358	-222 ± 198	1020 ± 428		
I	-13.1 ± 9.3	6.1 ± 3.3	0	644 ± 302	-512 ± 297	-514 ± 247	-818 ± 388	-145 ± 125	994 ± 441	1056 ± 435	16.88%
II	-13.1 ± 9.2	6.1 ± 3.5	0	645 ± 301	-514 ± 296	-514 ± 247	-820 ± 387	-146 ± 125	995 ± 441	1057 ± 434	14.05%
III	-13.1 ± 8.0	6.1 ± 2.9	0	642 ± 304	-514 ± 297	-513 ± 247	-816 ± 391	-145 ± 126	993 ± 442	1055 ± 436	33.00%
PPMXL	-7.9 ± 0.1	3.2 ± 0.6	-3.3 ± 0.6	709 ± 199	-555 ± 173	-526 ± 152	-867 ± 238	-241 ± 115	1054 ± 262		
I	-12.4 ± 1.7	6.6 ± 1.3	0	681 ± 201	-541 ± 174	-534 ± 151	-860 ± 240	-151 ± 79	1032 ± 266	1093 ± 255	3.58%
II	-12.4 ± 1.7	6.6 ± 1.3	0	682 ± 201	-543 ± 174	-534 ± 151	-862 ± 240	-152 ± 79	1033 ± 266	1095 ± 255	2.25%
III	-12.4 ± 1.6	6.6 ± 1.3	0	682 ± 201	-543 ± 174	-534 ± 151	-862 ± 240	-153 ± 79	1034 ± 266	1095 ± 255	16.94%
APOP	-7.9 ± 0.1	3.2 ± 0.6	-3.3 ± 0.6	-51 ± 40	206 ± 23	89 ± 24	123 ± 41	171 ± 30	234 ± 29		
I	3.9 ± 1.8	-7.1 ± 2.4	0	-214 ± 38	-13 ± 27	-184 ± 31	-86 ± 41	193 ± 40	284 ± 45	215 ± 40	100%
II	3.9 ± 1.8	-7.0 ± 2.5	0	-214 ± 39	-15 ± 26	-185 ± 32	-86 ± 41	194 ± 41	285 ± 46	216 ± 40	100%
III	3.9 ± 1.8	-7.2 ± 2.3	0	-207 ± 38	-10 ± 28	-181 ± 32	-83 ± 42	187 ± 39	277 ± 45	212 ± 40	100%
HSOY	-7.9 ± 0.1	3.2 ± 0.6	-3.3 ± 0.6	480 ± 112	-313 ± 104	-328 ± 89	-564 ± 140	-105 ± 56	665 ± 160		
I	-12.5 ± 1.2	6.1 ± 1.4	0	437 ± 118	-293 ± 105	-342 ± 88	-523 ± 147	-65 ± 37	631 ± 165	698 ± 153	36.76%
II	-12.5 ± 1.2	6.1 ± 1.4	0	437 ± 118	-295 ± 105	-342 ± 88	-525 ± 147	-66 ± 37	633 ± 165	700 ± 153	27.19%
III	-12.5 ± 1.2	6.1 ± 1.4	0	436 ± 117	-295 ± 105	-342 ± 88	-524 ± 147	-66 ± 37	632 ± 165	699 ± 152	80.19%

Table A.14: Same as Table A.1 but for SDSS J225912.13+074356.5 (#14).

PM/ Model	x (kpc)	y (kpc)	z (kpc)	v_x (km/s)	v_y (km/s)	v_z (km/s)	v_r (km/s)	v_ϕ (km/s)	$v_{\rm GRF}$ (km/s)	$v_{\rm ej}$ (km/s)	bound
this work	-9.3 ± 0.2	-1.4 ± 0.3	1.5 ± 0.3	31 ± 22	237 ± 19	5 ± 18	-66 ± 22	230 ± 21	241 ± 18		
I	-6.0 ± 2.2	-9.1 ± 1.0	0	-147 ± 40	111 ± 65	56 ± 8	-15 ± 39	194 ± 18	207 ± 19	82 ± 17	100%
II	-6.1 ± 2.2	-9.1 ± 1.0	0	-144 ± 40	114 ± 63	56 ± 8	-17 ± 39	193 ± 18	205 ± 19	84 ± 17	100%
III	-6.1 ± 2.2	-9.1 ± 1.0	0	-144 ± 40	114 ± 63	56 ± 8	-17 ± 39	193 ± 18	205 ± 19	84 ± 17	100%
SDSS (P14)	-9.3 ± 0.2	-1.4 ± 0.3	1.5 ± 0.3	-512 ± 108	236 ± 44	-330 ± 75	470 ± 99	312 ± 53	657 ± 117		
I	110.8 ± 41.1	-9.1 ± 7.7	0	96 ± 135	-28 ± 8	29 ± 12	98 ± 133	27 ± 16	150 ± 83	239 ± 55	33.81%
II	151.7 ± 88.1	-14.3 ± 12.1	0	-25 ± 86	-17 ± 11	24 ± 15	-22 ± 83	25 ± 21	84 ± 48	196 ± 20	21.65%
III	51.7 ± 10.9	-2.3 ± 3.4	0	335 ± 160	-59 ± 14	70 ± 25	338 ± 157	54 ± 11	356 ± 144	392 ± 124	88.29%
USNO	-9.3 ± 0.2	-1.4 ± 0.3	1.5 ± 0.3	-516 ± 97	250 ± 16	-317 ± 61	472 ± 88	327 ± 31	657 ± 104		
I	122.2 ± 36.3	-11.5 ± 3.6	0	86 ± 127	-29 ± 7	24 ± 9	89 ± 124	26 ± 16	141 ± 72	233 ± 45	30.81%
II	168.1 ± 93.6	-18.3 ± 8.0	0	-43 ± 72	-16 ± 9	21 ± 14	-39 ± 69	24 ± 21	75 ± 48	190 ± 18	18.50%
III	53.8 ± 8.5	-2.7 ± 2.4	0	344 ± 155	-65 ± 8	64 ± 19	347 ± 152	55 ± 11	362 ± 140	397 ± 120	90.78%
PPMXL	-9.3 ± 0.2	-1.4 ± 0.3	1.5 ± 0.3	-547 ± 114	218 ± 46	-367 ± 81	507 ± 106	300 ± 53	697 ± 126		
I	106.4 ± 35.5	-7.2 ± 6.3	0	119 ± 135	-28 ± 7	31 ± 12	121 ± 133	26 ± 14	163 ± 87	249 ± 59	23.56%
II	149 ± 80	-11.9 ± 9.9	0	-10 ± 88	-18 ± 10	25 ± 15	-8 ± 85	23 ± 20	83 ± 47	198 ± 20	14.26%
III	48.2 ± 9.8	-1.3 ± 2.7	0	370 ± 151	-56 ± 15	79 ± 28	372 ± 148	55 ± 11	388 ± 139	421 ± 120	79.41%
APOP	-9.3 ± 0.2	-1.4 ± 0.3	1.5 ± 0.3	43 ± 19	205 ± 12	-17 ± 15	-73 ± 20	196 ± 14	212 ± 10		
I	-4.0 ± 2.5	-8.9 ± 0.7	0	-181 ± 34	20 ± 68	58 ± 12	48 ± 34	187 ± 22	204 ± 28	98 ± 21	100%
II	-4.2 ± 2.5	-8.9 ± 0.7	0	-178 ± 34	25 ± 66	58 ± 12	45 ± 34	184 ± 22	201 ± 27	99 ± 21	100%
III	-3.8 ± 2.6	-8.8 ± 0.7	0	-185 ± 33	12.6 ± 68	57 ± 13	53 ± 33	188 ± 23	206 ± 28	100 ± 22	100%

Table A.15: Same as Table A.1 but for SDSS J095816.39+005224.4 (#15).

PM/ Model	x (kpc)	y (kpc)	z (kpc)	v_x (km/s)	v_y (km/s)	v_z (km/s)	v_r (km/s)	v_ϕ (km/s)	v_{GRF} (km/s)	v_{ej} (km/s)	bound
this work	-11.2 ± 0.2	-1.1 ± 0.1	1.1 ± 0.1	-66 ± 36	274 ± 74	-40 ± 68	39 ± 31	279 ± 76	294 ± 74		
I	7.6 ± 16.5	-11.8 ± 9.2	0	-152 ± 81	27 ± 160	64 ± 37	-44 ± 74	208 ± 72	237 ± 72	122 ± 52	99.98%
II	8.0 ± 18.9	-12.4 ± 11.0	0	-154 ± 77	34 ± 158	64 ± 38	-48 ± 73	206 ± 74	236 ± 74	124 ± 52	99.92%
III	6.0 ± 12.3	-10.4 ± 6.3	0	-145 ± 90	9 ± 166	67 ± 38	-29 ± 75	215 ± 63	242 ± 64	116 ± 51	100%
SDSS (P14)	-11.2 ± 0.2	-1.1 ± 0.1	1.1 ± 0.1	170 ± 46	-579 ± 106	-291 ± 86	-111 ± 39	-593 ± 109	676 ± 113		
I	15.1 ± 5.2	9.1 ± 17.0	0	159 ± 52	375 ± 82	145 ± 50	309 ± 66	-270 ± 50	441 ± 62	608 ± 65	22.18%
II	16.8 ± 7.6	12.4 ± 24.4	0	156 ± 58	314 ± 95	117 ± 43	285 ± 89	-212 ± 39	384 ± 60	541 ± 58	12.03%
III	13.2 ± 2.1	6.4 ± 7.4	0	155 ± 51	501 ± 81	200 ± 63	346 ± 50	-396 ± 66	568 ± 76	748 ± 78	83.50%
PPMXL	-11.2 ± 0.2	-1.1 ± 0.1	1.1 ± 0.1	-82 ± 51	397 ± 98	43 ± 97	42 ± 45	403 ± 101	421 ± 102		
I	4.0 ± 30.5	-16.0 ± 27.1	0	-128 ± 91	268 ± 194	84 ± 62	-113 ± 117	298 ± 138	356 ± 134	222 ± 96	94.20%
II	4.2 ± 34.7	-16.6 ± 30.8	0	-134 ± 80	277 ± 183	85 ± 62	-121 ± 108	299 ± 138	358 ± 134	223 ± 96	88.28%
III	1.4 ± 19.8	-13.2 ± 15.9	0	-119 ± 104	243 ± 217	85 ± 61	-92 ± 128	299 ± 130	354 ± 130	215 ± 98	99.96%
HSOY	-11.2 ± 0.2	-1.1 ± 0.1	1.1 ± 0.1	-42 ± 21	261 ± 39	10 ± 39	16 ± 18	264 ± 40	268 ± 41		
I	-3.9 ± 6.6	-9.6 ± 3.5	0	-178 ± 52	130 ± 114	54 ± 17	-37 ± 44	245 ± 33	258 ± 33	82 ± 29	100%
II	-4.1 ± 6.5	-9.6 ± 3.6	0	-176 ± 52	134 ± 111	54 ± 17	-38 ± 44	244 ± 34	257 ± 33	83 ± 29	100%
III	-3.8 ± 6.5	-9.4 ± 3.3	0	-180 ± 53	122 ± 119	53 ± 17	-32 ± 42	246 ± 32	257 ± 32	78 ± 27	100%

Table A.16: Same as Table A.1 but for SDSS J074728.84+185520.4 (#16).

PM/ Model	x (kpc)	y (kpc)	z (kpc)	v_x (km/s)	v_y (km/s)	v_z (km/s)	v_r (km/s)	v_ϕ (km/s)	v_{GRF} (km/s)	v_{ej} (km/s)	bound
this work	-10.1 ± 0.1	0.056 ± 0.004	0.44 ± 0.04	42 ± 8	313 ± 30	145 ± 29	-40 ± 8	313 ± 30	348 ± 31		
I	-10.2 ± 0.1	-0.9 ± 0.2	0	24 ± 11	312 ± 30	147 ± 28	-53 ± 9	308 ± 29	347 ± 31	173 ± 31	100%
II	-10.2 ± 0.1	-0.9 ± 0.2	0	25 ± 11	310 ± 29	147 ± 28	-53 ± 9	307 ± 29	345 ± 31	172 ± 31	100%
III	-10.2 ± 0.1	-0.9 ± 0.2	0	24 ± 11	310 ± 30	146 ± 28	-52 ± 9	306 ± 29	345 ± 31	172 ± 31	100%
SDSS (P14)	-10.1 ± 0.1	0.056 ± 0.004	0.44 ± 0.04	97 ± 9	494 ± 28	334 ± 33	-94 ± 9	494 ± 28	604 ± 37		
I	-10.2 ± 0.1	-0.6 ± 0.1	0	89 ± 9	494 ± 28	335 ± 33	-118 ± 11	487 ± 28	603 ± 37	434 ± 39	44.35%
II	-10.2 ± 0.1	-0.6 ± 0.1	0	89 ± 9	492 ± 28	335 ± 33	-118 ± 11	486 ± 28	602 ± 37	433 ± 39	10.89%
III	-10.2 ± 0.1	-0.6 ± 0.1	0	89 ± 9	491 ± 28	335 ± 33	-118 ± 10	485 ± 28	602 ± 37	432 ± 39	100%
USNO	-10.1 ± 0.1	0.056 ± 0.004	0.44 ± 0.04	73 ± 15	476 ± 81	245 ± 53	-71 ± 15	477 ± 81	542 ± 88		
I	-10.2 ± 0.1	-0.8 ± 0.2	0	63 ± 18	478 ± 81	246 ± 53	-102 ± 21	471 ± 80	543 ± 88	357 ± 83	73.55%
II	-10.3 ± 0.1	-0.8 ± 0.2	0	63 ± 18	476 ± 81	246 ± 53	-102 ± 21	469 ± 79	541 ± 88	356 ± 83	56.98%
III	-10.2 ± 0.1	-0.8 ± 0.2	0	63 ± 18	475 ± 81	246 ± 53	-101 ± 21	469 ± 79	541 ± 88	356 ± 83	99.70%
PPMXL	-10.1 ± 0.1	0.056 ± 0.004	0.44 ± 0.04	86 ± 12	479 ± 44	294 ± 45	-84 ± 12	479 ± 44	570 ± 49		
I	-10.2 ± 0.1	-0.7 ± 0.1	0	78 ± 13	480 ± 44	295 ± 45	-110 ± 13	474 ± 44	571 ± 49	395 ± 50	70.98%
II	-10.2 ± 0.1	-0.7 ± 0.1	0	78 ± 13	479 ± 44	295 ± 45	-109 ± 13	472 ± 43	569 ± 49	394 ± 50	39.83%
III	-10.2 ± 0.1	-0.7 ± 0.1	0	78 ± 13	478 ± 44	295 ± 45	-109 ± 13	472 ± 43	569 ± 49	394 ± 50	100%
HSOY	-10.1 ± 0.1	0.056 ± 0.004	0.44 ± 0.04	77 ± 8	425 ± 24	264 ± 28	-74 ± 8	425 ± 24	507 ± 30		
I	-10.2 ± 0.1	-0.7 ± 0.1	0	67 ± 8	426 ± 24	265 ± 28	-95 ± 9	421 ± 24	507 ± 30	336 ± 32	99.66%
II	-10.2 ± 0.1	-0.7 ± 0.1	0	67 ± 8	425 ± 24	265 ± 28	-95 ± 9	419 ± 24	506 ± 30	335 ± 32	93.71%
III	-10.2 ± 0.1	-0.7 ± 0.1	0	67 ± 8	424 ± 24	265 ± 28	-94 ± 9	419 ± 24	505 ± 30	335 ± 32	100%

Table A.17: Same as Table A.1 but for SDSS J064257.02+371604.2 (#17).

PM/ Model	x (kpc)	y (kpc)	z (kpc)	v_x (km/s)	v_y (km/s)	v_z (km/s)	v_r (km/s)	v_ϕ (km/s)	v_{GRF} (km/s)	v_{ej} (km/s)	bound
this work	-6.9 ± 0.3	3.1 ± 0.6	2.7 ± 0.5	486 ± 120	-96 ± 55	-199 ± 41	-480 ± 120	119 ± 56	537 ± 124		
I	-2.7 ± 6.0	-1.0 ± 2.3	0	-507 ± 81	-40 ± 94	255 ± 89	367 ± 167	299 ± 148	585 ± 68	512 ± 55	74.57%
II	-2.9 ± 6.7	-1.0 ± 2.6	0	-487 ± 77	-50 ± 96	251 ± 90	367 ± 152	275 ± 144	566 ± 69	501 ± 50	63.58%
III	-2.8 ± 5.2	-1.0 ± 2.0	0	-552 ± 94	-3 ± 91	260 ± 90	391 ± 200	324 ± 155	626 ± 74	547 ± 73	97.85%
SDSS (P14)	-6.9 ± 0.3	3.1 ± 0.6	2.7 ± 0.5	574 ± 129	-59 ± 55	-294 ± 60	-544 ± 120	190 ± 76	651 ± 135		
I	0.5 ± 2.1	-1.7 ± 0.9	0	-453 ± 114	-159 ± 79	390 ± 67	77 ± 184	449 ± 96	636 ± 50	506 ± 40	41.37%
II	0.5 ± 2.4	-1.6 ± 1.0	0	-422 ± 116	-176 ± 81	387 ± 68	103 ± 174	423 ± 94	617 ± 47	494 ± 38	29.80%
III	0.2 ± 1.7	-1.9 ± 0.7	0	-545 ± 120	-113 ± 82	392 ± 71	82 ± 226	509 ± 116	696 ± 68	557 ± 58	87.69%
USNO	-6.9 ± 0.3	3.1 ± 0.6	2.7 ± 0.5	428 ± 109	38 ± 103	-324 ± 137	-372 ± 94	217 ± 116	556 ± 148		
I	-2.3 ± 16.8	-1.1 ± 7.5	0	-309 ± 169	-188 ± 133	325 ± 122	178 ± 156	318 ± 140	534 ± 114	448 ± 60	68.26%
II	-3.5 ± 20.2	-0.6 ± 9.0	0	-291 ± 174	-182 ± 135	305 ± 123	195 ± 156	290 ± 140	510 ± 117	436 ± 60	58.34%
III	-0.5 ± 9.7	-1.9 ± 4.6	0	-355 ± 158	-191 ± 133	372 ± 124	134 ± 164	373 ± 145	587 ± 117	484 ± 72	94.39%
PPMXL	-6.9 ± 0.3	3.1 ± 0.6	2.7 ± 0.5	452 ± 140	2 ± 82	-294 ± 95	-408 ± 136	193 ± 89	552 ± 147		
I	-0.3 ± 11.0	-2.1 ± 5.0	0	-337 ± 155	-194 ± 118	341 ± 96	176 ± 153	346 ± 12	554 ± 88	453 ± 60	68.72%
II	-0.8 ± 12.9	-2.0 ± 5.8	0	-314 ± 154	-196 ± 120	326 ± 96	197 ± 142	320 ± 117	532 ± 87	441 ± 56	58.80%
III	0.1 ± 7.4	-2.2 ± 3.4	0	-403 ± 158	-169 ± 119	370 ± 100	135 ± 184	399 ± 137	605 ± 102	491 ± 77	94.88%
APOP	-6.9 ± 0.3	3.1 ± 0.6	2.7 ± 0.5	568 ± 287	0 ± 123	-360 ± 82	-514 ± 299	241 ± 91	700 ± 256		
I	4.2 ± 6.8	-4.7 ± 5.1	0	-185 ± 176	-260 ± 78	352 ± 93	124 ± 121	307 ± 119	505 ± 124	420 ± 81	42.48%
II	4.7 ± 8.4	-5.2 ± 6.5	0	-147 ± 163	-261 ± 77	329 ± 93	148 ± 107	277 ± 112	474 ± 121	399 ± 77	35.72%
III	3.0 ± 3.9	-3.7 ± 2.9	0	-309 ± 210	-228 ± 88	401 ± 88	50 ± 159	389 ± 142	590 ± 140	481 ± 103	70.12%
HSOY	-6.8 ± 0.3	3.1 ± 0.6	2.7 ± 0.5	489 ± 110	-64 ± 48	-241 ± 46	-470 ± 104	150 ± 61	552 ± 113		
I	-0.6 ± 2.1	-1.7 ± 0.8	0	-484 ± 97	-122 ± 87	328 ± 75	231 ± 183	409 ± 111	614 ± 49	497 ± 45	71.91%
II	-0.7 ± 2.2	-1.6 ± 0.7	0	-463 ± 94	-135 ± 89	325 ± 76	245 ± 171	385 ± 109	599 ± 46	488 ± 41	59.17%
III	-0.8 ± 2.2	-1.8 ± 0.8	0	-538 ± 109	-82 ± 84	333 ± 76	237 ± 217	444 ± 121	654 ± 65	530 ± 63	98.28%

Table A.18: Same as Table A.1 but for SDSS J165956.02+392414.9 (#18).

PM/ Model	x (kpc)	y (kpc)	z (kpc)	v_x (km/s)	v_y (km/s)	v_z (km/s)	v_r (km/s)	v_ϕ (km/s)	v_{GRF} (km/s)	v_{ej} (km/s)	bound
this work	-8.420 ± 0.004	-3.5 ± 0.6	2.9 ± 0.5	-126 ± 49	57 ± 31	-23 ± 36	95 ± 47	103 ± 27	151 ± 41		
I	1.4 ± 2.6	-2.1 ± 1.6	0	-251 ± 57	-175 ± 68	203 ± 58	15 ± 139	277 ± 73	380 ± 46	266 ± 46	100%
II	1.4 ± 2.6	-2.0 ± 1.6	0	-249 ± 59	-182 ± 72	203 ± 60	14 ± 141	279 ± 76	382 ± 48	268 ± 47	100%
III	1.4 ± 2.7	-2.1 ± 1.6	0	-249 ± 56	-166 ± 64	209 ± 60	21 ± 138	269 ± 72	376 ± 47	268 ± 46	100%
SDSS (P14)	-8.420 ± 0.004	-3.5 ± 0.6	2.9 ± 0.5	-622 ± 190	58 ± 99	-25 ± 118	550 ± 171	297 ± 125	645 ± 188		
I	33.4 ± 76.2	1.2 ± 16.8	0	-557 ± 172	-44 ± 84	132 ± 57	-458 ± 224	235 ± 183	585 ± 164	532 ± 167	43.39%
II	32.4 ± 73.7	1.1 ± 16.1	0	-562 ± 171	-47 ± 85	133 ± 56	-463 ± 225	235 ± 183	590 ± 161	536 ± 167	34.61%
III	37.0 ± 80.3	2.2 ± 17.9	0	-531 ± 194	-38 ± 81	129 ± 59	-434 ± 231	228 ± 185	562 ± 179	513 ± 168	79.96%
USNO	-8.420 ± 0.004	-3.5 ± 0.6	2.9 ± 0.5	-680 ± 194	90 ± 161	12 ± 189	591 ± 126	349 ± 217	727 ± 205		
I	29.8 ± 69.9	1.7 ± 20.6	0	-644 ± 247	25 ± 141	164 ± 97	-470 ± 241	352 ± 307	683 ± 257	614 ± 200	28.71%
II	28.8 ± 69.3	1.3 ± 20.4	0	-655 ± 234	22 ± 143	166 ± 96	-479 ± 234	355 ± 306	692 ± 249	621 ± 196	20.58%
III	31.7 ± 65.0	2.7 ± 18.6	0	-588 ± 315	33 ± 137	159 ± 97	-420 ± 286	332 ± 309	649 ± 279	590 ± 211	68.45%
PPMXL	-8.420 ± 0.004	-3.5 ± 0.6	2.9 ± 0.5	-706 ± 249	-81 ± 144	-188 ± 170	683 ± 236	203 ± 162	768 ± 254		
I	66.7 ± 116.8	10.5 ± 28.3	0	-508 ± 249	-62 ± 70	103 ± 63	-467 ± 257	133 ± 161	540 ± 228	535 ± 205	26.90%
II	64.7 ± 115.7	9.9 ± 28.3	0	-526 ± 237	-68 ± 70	105 ± 63	-486 ± 248	136 ± 161	555 ± 222	548 ± 204	21.20%
III	73.4 ± 116.2	13.1 ± 26.8	0	-403 ± 326	-38 ± 83	97 ± 63	-364 ± 326	116 ± 158	482 ± 243	491 ± 207	57.52%
APOP	-8.4 ± 0.01	-3.5 ± 0.6	2.9 ± 0.5	-107 ± 154	117 ± 77	49 ± 91	54 ± 156	150 ± 70	235 ± 100		
I	-1.3 ± 12.4	-4.1 ± 4.7	0	-206 ± 131	-13 ± 136	170 ± 55	-19 ± 150	209 ± 107	319 ± 91	247 ± 78	99.64%
II	-1.3 ± 13.0	-4.1 ± 4.8	0	-204 ± 131	-14.7 ± 138	170 ± 56	-19 ± 151	208 ± 108	319 ± 92	248 ± 79	99.31%
III	-1.3 ± 11.1	-4.1 ± 4.1	0	-203 ± 130	-10 ± 131	171 ± 57	-15 ± 148	205 ± 106	316 ± 91	247 ± 77	99.99%

Table A.19: Same as Table A.1 but for SDSS J110815.19-155210.3 (#19).

86

PM/ Model	x (kpc)	y (kpc)	z (kpc)	v_x (km/s)	v_y (km/s)	v_z (km/s)	v_r (km/s)	v_ϕ (km/s)	v_{GRF} (km/s)	v_{ej} (km/s)	bound
this work	-4.7 ± 0.7	-0.3 ± 0.1	4.6 ± 0.8	73 ± 59	220 ± 80	68 ± 50	-88 ± 59	214 ± 81	257 ± 69		
I	-4.7 ± 1.7	-6.1 ± 2.8	0	-98 ± 41	112 ± 73	201 ± 48	-30 ± 91	133 ± 48	262 ± 58	251 ± 48	100%
II	-4.7 ± 1.8	-6.0 ± 2.8	0	-99 ± 42	111 ± 73	201 ± 48	-29 ± 92	133 ± 48	262 ± 58	252 ± 49	99.99%
III	-4.8 ± 1.7	-6.1 ± 2.8	0	-92 ± 39	114 ± 72	198 ± 49	-34 ± 89	129 ± 48	257 ± 58	251 ± 48	100%
SDSS (P14)	-4.7 ± 0.7	-0.3 ± 0.1	4.6 ± 0.8	405 ± 141	413 ± 167	-189 ± 114	-432 ± 147	383 ± 164	632 ± 178		
I	-29.3 ± 34.1	-55.4 ± 82.5	0	-87 ± 145	17 ± 220	62 ± 43	38 ± 269	46 ± 36	250 ± 143	309 ± 114	52.01%
II	-33.0 ± 39.7	-60.9 ± 91.3	0	-51 ± 127	70 ± 204	59 ± 41	-28 ± 247	44 ± 36	228 ± 135	293 ± 106	43.19%
III	-20.3 ± 21.3	-39.5 ± 57.3	0	-184 ± 174	-121 ± 239	84 ± 55	210 ± 293	62 ± 44	335 ± 184	378 ± 154	85.39%
USNO	-4.7 ± 0.7	-0.3 ± 0.1	4.6 ± 0.8	713 ± 241	672 ± 278	-421 ± 192	-758 ± 254	619 ± 269	1098 ± 323		
I	-28.6 ± 38.0	-69.0 ± 112.8	0	-99 ± 186	70 ± 343	73 ± 59	-3 ± 400	60 ± 59	363 ± 210	404 ± 181	5.89%
II	-32.8 ± 42.6	-78.5 ± 123.5	0	-50 ± 165	158 ± 333	64 ± 52	-108 ± 386	51 ± 50	350 ± 224	396 ± 195	4.24%
III	-17.9 ± 26.6	-45.4 ± 84.9	0	-242 ± 207	-172 ± 327	113 ± 84	278 ± 374	103 ± 100	464 ± 205	480 ± 170	19.79%
PPMXL	-4.7 ± 0.7	-0.3 ± 0.1	4.6 ± 0.8	571 ± 190	584 ± 223	-312 ± 153	-611 ± 200	541 ± 218	902 ± 247		
I	-32.4 ± 40.6	-77.1 ± 115.4	0	-79 ± 170	61 ± 317	61 ± 49	-10 ± 366	54 ± 48	331 ± 189	376 ± 159	12.71%
II	-36.9 ± 45.1	-86.0 ± 122.9	0	-32 ± 150	146 ± 299	55 ± 44	-110 ± 344	47 ± 42	317 ± 197	367 ± 167	9.19%
III	-20.7 ± 28.2	-51.0 ± 85.4	0	-217 ± 195	-176 ± 305	96 ± 72	266 ± 353	87 ± 76	429 ± 199	453 ± 163	39.40%
APOP	-4.7 ± 0.7	-0.3 ± 0.1	4.6 ± 0.8	632 ± 114	307 ± 66	-380 ± 92	-651 ± 120	260 ± 66	803 ± 141		
I	-3.7 ± 1.9	-8.9 ± 4.0	0	-338 ± 78	-354 ± 56	142 ± 44	460 ± 67	171 ± 52	513 ± 82	491 ± 67	10.42%
II	-4.7 ± 2.6	-11.8 ± 5.6	0	-280 ± 74	-324 ± 63	108 ± 39	409 ± 76	135 ± 43	445 ± 86	439 ± 69	5.74%
III	-3.4 ± 1.5	-5.8 ± 2.1	0	-476 ± 84	-376 ± 57	220 ± 50	569 ± 67	214 ± 60	651 ± 76	615 ± 75	56.28%
HSOY	-4.7 ± 0.7	-0.3 ± 0.1	4.6 ± 0.8	307 ± 84	373 ± 95	-112 ± 68	-332 ± 90	350 ± 93	505 ± 105		
I	-33.7 ± 33.3	-58.9 ± 68.2	0	-26 ± 90	60 ± 155	49 ± 29	-37 ± 181	41 ± 28	174 ± 98	249 ± 70	86.98%
II	-37.7 ± 41.4	-64.8 ± 80.5	0	-3 ± 75	96 ± 135	48 ± 30	-80 ± 155	40 ± 30	167 ± 92	244 ± 63	78.88%
III	-23.1 ± 16.3	-40.4 ± 36.3	0	-87 ± 115	-26.9 ± 181	60 ± 27	71 ± 215	47 ± 25	205 ± 128	272 ± 103	99.46%

Table A.20: Same as Table A.1 but for SDSS J145132.12+003258.0 (#20).

List of Figures

List of Tables

List of acronyms

2MASS Two Micron All Sky Survey

AGB Asymptotic Giant Branch

APOP Absolute Proper Motions outside the Plane

BHB Blue Horizontal Branch

CNO carbon-nitrogen-oxygen

DSS Digitised Sky Survey

EHB Extreme or Extended Horizontal Branch

GC Galactic centre

HB Horizontal Branch

Hipparcos HIgh Precision PARallax COllecting Satellite

HRD Hertzsprung-Russel-Diagramm

HSOY Hot Stuff for One Year

HST Hubble Space Telescope

HVS Hypervelocity stars

LMC Large Magellanic Cloud

LSR local standard of rest

MUCHFUSS Massive Unseen Companions to Hot Faint Underluminous Stars from SDSS

PanSTARRS Panoramic Survey Telescope and Rapid Response System

POSS I First Palomar Observatory Sky Survey

POSS II Second Palomar Observatory Sky Survey

pp proton-proton

QVN Quick-V Northern survey

PPMXL Position and Proper Motions Extended Large

RAVE Radial Velocity Experiment

RGB Red Giant Branch

SDSS Sloan Digital Sky Survey

SED spectral energy distribution

SEGUE Sloan Extension for Galactic Understanding and Exploration

SMBH supermassive black hole

SN supernova

SN Ia supernova of type Ia

SSPP SEGUE Stellar Parameter Pipeline

UCAC4 Fourth US Naval Observatory CCD Astrograph Catalogue

UCAC5 Fifth US Naval Observatory CCD Astrograph Catalogue

USNO-B1.0 United States Naval Observatory

WD white dwarf

Bibliography

Abadi M.G., Navarro J.F., Steinmetz M., 2009, ApJL 691, L63

Ahn C.P., Alexandroff R., Allende Prieto C., et al., 2012, ApJS 203, 21

Allen C., Moreno E., Pichardo B., 2008, ApJ 674, 237

Allen C., Santillan A., 1991, Rev. Mex. Astron. Astrophys. 22, 255

Allende Prieto C., Sivarani T., Beers T.C., et al., 2008, AJ 136, 2070

Altmann M., Edelmann H., de Boer K.S., 2004, A&A 414, 181

Altmann M., Roeser S., Demleitner M., et al., 2017, A&A 600, L4

Behr B.B., 2003, ApJS 149, 101

Bender R., Kormendy J., Bower G., et al., 2005, ApJ 631, 280

Blaauw A., 1961, Bull. Astron. Inst. Netherlands 15, 265

Boubert D., Evans N.W., 2016, ApJL 825, L6

Bromley B.C., Kenyon S.J., Brown W.R., Geller M.J., 2009, ApJ 706, 925

Brown W.R., 2015, ARA&A 53, 15

Brown W.R., 2016, Physics Today 69, 52

Brown W.R., Anderson J., Gnedin O.Y., et al., 2015, ApJ 804, 49

Brown W.R., Anderson J., Gnedin O.Y., et al., 2010, ApJL 719, L23

Brown W.R., Geller M.J., Kenyon S.J., 2009, ApJ 690, 1639

Brown W.R., Geller M.J., Kenyon S.J., 2012, ApJ 751, 55

Brown W.R., Geller M.J., Kenyon S.J., 2014, ApJ 787, 89

Brown W.R., Geller M.J., Kenyon S.J., Kurtz M.J., 2005, ApJL 622, L33

Brown W.R., Geller M.J., Kenyon S.J., Kurtz M.J., 2006, ApJ 647, 303

Brown W.R., Geller M.J., Kenyon S.J., et al., 2007, ApJ 671, 1708

Castelli F., 1999, A&A 346, 564

Charpinet S., Fontaine G., Brassard P., et al., 2011, Nat 480, 496

Copperwheat C.M., Morales-Rueda L., Marsh T.R., et al., 2011, MNRAS 415, 1381

Cutri R.M., et al. 2013, VizieR Online Data Catalog 2328

de Bruijne J.H.J., 2012, Ap&SS 341, 31

Edelmann H., Heber U., Hagen H.J., et al., 2003, A&A 400, 939

Edelmann H., Napiwotzki R., Heber U., et al., 2005, ApJL 634, L181

Ferraro F.R., Beccari G., Dalessandro E., et al., 2009, Nat 462, 1028

Fink M., 2013, *Bachelor's thesis*, Friedrich-Alexander University Erlangen-Nürnberg

Fink M., Röpke F.K., Hillebrandt W., et al., 2010, A&A 514, A53

Fregeau J.M., Cheung P., Portegies Zwart S.F., Rasio F.A., 2004, MNRAS 352, 1

Fuentes C.I., Stanek K.Z., Gaudi B.S., et al., 2006, ApJL 636, L37

Fuhrmann K., 2011, MNRAS 414, 2893

Geier S., Fürst F., Ziegerer E., et al., 2015a, Sci 347, 1126

Geier S., Heber U., Podsiadlowski P., et al., 2010, A&A 519, A25

Geier S., Hirsch H., Tillich A., et al., 2011, A&A 530, A28

Geier S., Kupfer T., Heber U., et al., 2015b, A&A 577, A26

Geier S., Marsh T.R., Wang B., et al., 2013, A&A 554, A54

Geier S., Nesslinger S., Heber U., et al., 2007, A&A 464, 299

Geier S., Østensen R.H., Nemeth P., et al., 2017, A&A 600, A50

Genzel R., Eisenhauer F., Gillessen S., 2010, Reviews of Modern Physics 82, 3121

Ghez A.M., Salim S., Hornstein S.D., et al., 2005, ApJ 620, 744

Ghez A.M., Salim S., Weinberg N.N., et al., 2008, ApJ 689, 1044

Gillessen S., Eisenhauer F., Trippe S., et al., 2009, ApJ 692, 1075

Ginsburg I., Perets H.B., 2011, ArXiv e-prints

Gnedin O.Y., Gould A., Miralda-Escudé J., Zentner A.R., 2005, ApJ 634, 344

Greenstein J.L., 1956, In: Neyman J. (ed.) Third Berkeley Symposium on Mathematical Statistics and Probability., p.11

Gualandris A., Merritt D., 2009, ApJ 705, 361

Gualandris A., Portegies Zwart S., 2007, MNRAS 376, L29

Gvaramadze V.V., Gualandris A., 2011, MNRAS 410, 304

Gvaramadze V.V., Gualandris A., Portegies Zwart S., 2009, MNRAS 396, 570

Hawkins K., Kordopatis G., Gilmore G., et al., 2015, MNRAS 447, 2046

Heber U., 2009, ARA&A 47, 211

Heber U., 2016, PASP 128, 082001

Heber U., Edelmann H., Napiwotzki R., et al., 2008, A&A 483, L21

Hernquist L., 1990, ApJ 356, 359

Hills J.G., 1988, Nat 331, 687

Hirsch H.A., Heber U., O'Toole S.J., Bresolin F., 2005, A&A 444, L61

Humason M.L., Zwicky F., 1947, ApJ 105, 85

Iben, Jr. I., Tutukov A.V., 1984, ApJ 284, 719

Irrgang A., 2014, Ph.D. thesis, Friedrich-Alexander University Erlangen-Nürnberg

Irrgang A., Przybilla N., Heber U., et al., 2010, ApJ 711, 138

Irrgang A., Wilcox B., Tucker E., Schiefelbein L., 2013, A&A 549, A137

Johnson D.R.H., Soderblom D.R., 1987, AJ 93, 864

Justham S., Wolf C., Podsiadlowski P., Han Z., 2009, A&A 493, 1081

Kenyon S.J., Bromley B.C., Brown W.R., Geller M.J., 2014, ApJ 793, 122

Kenyon S.J., Bromley B.C., Geller M.J., Brown W.R., 2008, ApJ 680, 312

Kilic M., Munn J.A., Harris H.C., et al., 2006, AJ 131, 582

Kromer M., Sim S.A., Fink M., et al., 2010, ApJ 719, 1067

Lane R.R., Küpper A.H.W., Heggie D.C., 2012, MNRAS 423, 2845

Lanz T., Brown T.M., Sweigart A.V., et al., 2004, ApJ 602, 342

Latour M., Randall S.K., Fontaine G., et al., 2014, ApJ 795, 106

Lawrence A., Warren S.J., Almaini O., et al., 2007, MNRAS 379, 1599

Lee Y.S., Beers T.C., Allende Prieto C., et al., 2011, AJ 141, 90

Levin Y., 2006, ApJ 653, 1203

Madigan A.M., Pfuhl O., Levin Y., et al., 2014, ApJ 784, 23

Martin P., Jeffery C.S., Naslim N., Woolf V.M., 2017, MNRAS 467, 68

Massey R., 2010, MNRAS 409, L109

Maxted P.F.L., Heber U., Marsh T.R., North R.C., 2001, MNRAS 326, 1391

Maxted P.F.L., Marsh T.R., North R.C., 2000, MNRAS 317, L41

Mereghetti S., La Palombara N., Tiengo A., et al., 2011, ApJ 737, 51

Miller Bertolami M.M., Althaus L.G., Unglaub K., Weiss A., 2008, A&A 491, 253

Miyamoto M., Nagai R., 1975, PASJ 27, 533

Monet D.G., Levine S.E., Canzian B., et al., 2003, AJ 125, 984

Morales-Rueda L., Maxted P.F.L., Marsh T.R., et al., 2003, MNRAS 338, 752

Munari U., Sordo R., Castelli F., Zwitter T., 2005, A&A 442, 1127

Münch G., 1958, ApJ 127, 642

Napiwotzki R., 2008, In: Werner A., Rauch T. (eds.) Hydrogen-Deficient Stars, Vol. 391. Astronomical Society of the Pacific Conference Series, p. 257

Navarro J.F., Frenk C.S., White S.D.M., 1997, ApJ 490, 493

Nelemans G., Tauris T.M., 1998, A&A 335, L85

Németh P., Kawka A., Vennes S., 2012, MN-RAS 427, 2180

Németh P., Ziegerer E., Irrgang A., et al., 2016, ApJL 821, L13

Odenkirchen M., Brosche P., Borngen F., et al., 1997, A&AS 124

Oort J.H., Spitzer, Jr. L., 1955, ApJ 121, 6

Ott T., Eckart A., Genzel R., 1999, ApJ 523, 248

Palladino L.E., Schlesinger K.J., Holley-Bockelmann K., et al., 2014, ApJ 780, 7

Pauli E.M., Napiwotzki R., Altmann M., et al., 2003, A&A 400, 877

Pauli E.M., Napiwotzki R., Heber U., et al., 2006, A&A 447, 173

Perets H.B., 2009, ApJ 698, 1330

Pfuhl O., Alexander T., Gillessen S., et al., 2014, ApJ 782, 101

Poveda A., Ruiz J., Allen C., 1967, Boletin de los Observatorios Tonantzintla y Tacubaya 4, 86

Przybilla N., Fernanda Nieva M., Heber U., Butler K., 2008a, ApJL 684, L103

Przybilla N., Nieva M.F., Heber U., et al., 2008b, A&A 480, L37

Przybilla N., Tillich A., Heber U., Scholz R.D., 2010, ApJ 718, 37

Qi Z., Yu Y., Bucciarelli B., et al., 2015, AJ 150, 137

Raghavan D., McAlister H.A., Henry T.J., et al., 2010, ApJS 190, 1

Randall S.K., Bagnulo S., Ziegerer E., et al., 2015, A&A 576, A65

Reid M.J., Brunthaler A., 2004, ApJ 616, 872

Roeser S., Demleitner M., Schilbach E., 2010, AJ 139, 2440

Rossi E.M., Marchetti T., Cacciato M., et al., 2017, MNRAS 467, 1844

Ruiz-Lapuente P., Comeron F., Méndez J., et al., 2004, Nat 431, 1069

Schödel R., Ott T., Genzel R., et al., 2003, ApJ 596, 1015

Schönrich R., Binney J., Dehnen W., 2010, MNRAS 403, 1829

Sesana A., Haardt F., Madau P., 2008, ApJ 686, 432

Silva M.D.V., Napiwotzki R., 2011, MNRAS 411, 2596

Smith M.C., Ruchti G.R., Helmi A., et al., 2007, MNRAS 379, 755

Soker N., 1998, AJ 116, 1308

Stroeer A., Heber U., Lisker T., et al., 2007, A&A 462, 269

Svensson K.M., Church R.P., Davies M.B., 2008, MNRAS 383, L15

Tauris T.M., 2015, MNRAS 448, L6

Tillich A., Heber U., Geier S., et al., 2011, A&A 527, A137

Tillich A., Przybilla N., Scholz R.D., Heber U., 2009, A&A 507, L37

Volkert M., 2014, *Bachelor's thesis*, Friedrich-Alexander University Erlangen-Nürnberg

Wang B., Han Z., 2009, A&A 508, L27

Webbink R.F., 1984, ApJ 277, 355

Wilkinson M.I., Evans N.W., 1999, MNRAS 310, 645

Yu Q., Madau P., 2007, MNRAS 379, 1293

Yu Q., Tremaine S., 2003, ApJ 599, 1129

Zacharias N., Finch C., Frouard J., 2017, AJ 153, 166

Zacharias N., Finch C.T., Girard T.M., et al., 2013, AJ 145, 44

Zhang F., Lu Y., Yu Q., 2013, ApJ 768, 153

Zhong J., Chen L., Liu C., et al., 2014, ApJL 789, L2

Ziegerer E., Heber U., Geier S., et al., 2017, A&A 601, A58

Ziegerer E., Volkert M., Heber U., et al., 2015, A&A 576, L14